TAMPEREEN TEKNILLINEN YLIOPISTO
TAMPERE UNIVERSITY OF TECHNOLOGY

Henrik Tolvanen

Advanced Solid Fuel Characterization for Reactivity and Physical Property Comparison

Julkaisu 1359 • Publication 1359

Tampere 2016

Tampereen teknillinen yliopisto. Julkaisu 1359
Tampere University of Technology. Publication 1359

Henrik Tolvanen

Advanced Solid Fuel Characterization for Reactivity and Physical Property Comparison

Thesis for the degree of Doctor of Science in Technology to be presented with due permission for public examination and criticism in Konetalo Building, Auditorium K1702, at Tampere University of Technology, on the 19th of January 2016, at 12 noon.

Tampereen teknillinen yliopisto - Tampere University of Technology
Tampere 2016

Doctoral candidate: Henrik Tolvanen
Department of Chemistry and Bioengineering
Tampere University of Technology, Tampere, Finland

Supervisor: Professor Risto Raiko
Department of Chemistry and Bioengineering
Tampere University of Technology, Tampere, Finland

Pre-examiners: Professor Reginald Mitchell
Department of Mechanical Engineering
Stanford University, Stanford, California, USA

Assistant Professor Hao Wu
Department of Chemical and Biochemical Engineering
Technical University of Denmark, Lyngby, Denmark

Opponent: Professor Terese Løvås
Department of Energy and Process Engineering
Norwegian University of Science and Technology,
Trondheim, Norway

ISBN 978-952-15-3666-3 (printed)
ISBN 978-952-15-3674-8 (PDF)
ISSN 1459-2045

ABSTRACT

The main objective of this thesis was to formulate a method with which solid fuel combustion characteristics and physical properties could be accurately compared between different samples. The main study instrument used and further developed in the fuel reactivity tests during this work was a laminar drop-tube reactor (DTR). Five different solid fuel sample types were tested with the DTR. The samples were selected to represent a wide range of possible solid fuel types relevant to energy production in Finland. Fossil coal was selected as a reference fuel. Peat was chosen as it is a commonly co-fired with biomass in Finland. The three other samples, raw, torrefied, and steam-exploded woody biomasses, were chosen to find out how thermochemical pretreatment of biomass feedstock affects the fuel combustion characteristics.

In addition to the DTR tests, the fine grinding energy requirement of the biomass samples was also examined. Moreover, collaboration work with other researchers was conducted to examine the effect of torrefaction on the fine grinding energy requirement, chlorine content, and heating value. Various domestic and foreign wood species were used in these studies. The torrefaction process was noted to reduce the energy required to fine grind the tested sample. It was also noted that during torrefaction the chlorine content of the solid matter was reduced and the specific heating value was slightly increased. Fine grinding the steam-exploded biomass produced more spherical particles compared to the raw and torrefied pellet samples.

The combustion behavior of the five main samples was tested in the DTR. The samples were preground and the particles sieved with vibration sieves with an opening of 100-125 µm. The pyrolysis process was examined separately at a temperature range of 973-1173 K in pure N_2. The combined pyrolysis and combustion tests were conducted at a reactor temperature of 1123 K. The O_2 concentrations used in the combustion measurements were 3–21 vol-% in either N_2 or CO_2 atmospheres. The surface temperature of the combusting sample particles was measured with a two-color pyrometer. The initial size distribution of the sample particles as well as their size and geometry evolution as a function of conversion was studied by using optical techniques. The density, specific surface area, and mean pore diameter were measured from the samples with a mercury porosimeter. The reactivity parameters, which describe the pyrolysis and char oxidation rates of the samples, were determined by using the data from the measurements. Using discretized size distribution in the model calculations explained better the measured particle surface temperatures than using a mono sized single particle model. Moreover, combining the optical techniques with the DTR setup provided valuable data on the geometry evolution of the particles.

Based on the reactivity parameters, the sample combustion characteristics could be compared with one another. The reactivity comparison method presented in this thesis relies on consistent DTR measurements, determining accurately the size distribution and porosity of the sample particles, and using multiobjective optimization in fitting the model parameters.

PREFACE

This work was carried out in Tampere University of Technology in the Department of Energy and Process Engineering (2011-2012) and the Department of Chemistry and Bioengineering (2013-2015). The financial support received from Valmet Technologies (former Metso Power), Fortum, UPM, Pohjolan Voima, Helen, Gasum, Neste, Carbon Capture and Storage Program (CCSP) research program coordinated by CLIC Innovation Oy with funding from the Finnish Funding Agency for Technology and Innovation (Tekes), and Tampere University of Technology is gratefully acknowledged.

I would like to express my gratitude to my supervisor, Prof. Risto Raiko. He gave me the possibility to independently build and direct this project, yet always provided the necessary guidance whenever I needed it. Moreover, he ensured that I would have the necessary tools and know-how to continue my academic endeavours after this thesis. From my colleagues the greatest thanks go to Dr. Lauri Kokko. He saw the ups and downs related to this project from near and far, as a colleague and friend, and provided invaluable help and support. I am also grateful to Dr. Milena Rodriguez for helping me get started in my scientific career. I wish to thank Dr. Eugene Podkletnov for providing me with valuable guidance and ideas related to the experimental work of this thesis. Taru Siitonen, Markus Fager-Pintilä, Tiina Keipi, Jaana Rajamäki, and Kai Hämäläinen were also a great help to me in conducting the measurements. I thank Dr. Markus Honkanen and M.Sc. Matti Paananen for their help with the camera and pyrometer systems. Laboratory engineers Matti Savela and Jarmo Ruusila were of great help in constructing the experimental devices. Without them I could have not succeeded in making a single measurement for this thesis.

Dr. Matti Lindstedt and Dr. Oskar Karlström gave me valuable help and tips related to programming and combustion modeling. I thank them both. I am grateful to all the coworkers in the former Department of Energy and Process Engineering and the current Department of Chemistry and Bioengineering, with whom I had the pleasure to work, for making this an inspiring place to work. Satu Palonen, Anna Pääkkönen, and Aino Leppänen especially gave me a lot of support and encouragement. I would like to express my gratitude to my training partners along these years and most of all to the Acrowork team for reminding me that there is more in life than just the academic world.

I owe a special debt to my parents and sisters for helping me in this project. I would also like to say thank you to my dear friend Saila for keeping me on track. Finally, thank you Jenni and Vilma for giving me your unconditional love and supporting me in this long process called life.

Tampere, December 14, 2015

Henrik Tolvanen

LIST OF PUBLICATIONS

This thesis is based on the following five publications, referred to as Publications I–V. Additionally, some unpublished material is presented and discussed.

I Lauri Kokko, Henrik Tolvanen, Kai Hämäläinen, Risto Raiko. Comparing the energy required for fine grinding torrefied and fast heat treated pine. Biomass and Bioenergy, Volume 42, July 2012, Pages 219-223.

II Henrik Tolvanen, Lauri Kokko, Risto Raiko. Fast pyrolysis of coal, peat, and torrefied wood: Mass loss study with a drop-tube reactor, particle geometry analysis, and kinetics modeling. Fuel, Volume 111, September 2013, Pages 148-156.

III Henrik Tolvanen and Risto Raiko. An experimental study and numerical modeling of combusting two coal chars in a drop-tube reactor: A comparison between N_2/O_2, CO_2/O_2, and $N_2/CO_2/O_2$ atmospheres. Fuel, Volume 124, 15 May 2014, Pages 190-201.

IV Tiina Keipi, Henrik Tolvanen, Lauri Kokko, and Risto Raiko. The effect of torrefaction on the chlorine content and heating value of eight woody biomass samples. Biomass and Bioenergy, Volume 66, July 2014, Pages 232-239.

V Henrik Tolvanen, Tiina Keipi, Risto Raiko. A study on raw, torrefied, and steam-exploded wood: fine grinding, drop-tube reactor combustion tests in N_2/O_2 and CO_2/O_2 atmospheres, particle geometry analysis, and numerical kinetics modeling. Fuel, Submitted August 2015.

AUTHOR'S CONTRIBUTION

I The author was involved in constructing the experimental setup, conducting the measurements, and had a minor role in writing the manuscript.

II The author was involved in designing and constructing the experimental setup and carried out most of the measurements. The author wrote the program, conducted the simulations, and wrote the manuscript.

III The author carried out most of the measurements and developed further the existing imaging techniques. The article presented new measurement data and simulations on oxidation and gasification reaction competition. The author wrote the program, conducted the simulations, and wrote the manuscript.

IV The author was involved in constructing the experimental setup, conducting the measurements, and had a minor role in writing the manuscript.

V The author carried out most of the measurements. The author wrote the program, conducted the simulations, and wrote the manuscript.

LIST OF SYMBOLS AND ABBREVIATIONS

Latin symbols

A	area	m^2
A	pre-exponential factor	s^{-1}, s m^{-1}
A_g	internal surface area	m^2 kg^{-1}
B	coefficient related to Stefan flow	-
c	specific heat capacity	J kg^{-1} K^{-1}
C	concentration	mol m^{-3}
d	diameter	m
D	diffusion coefficient	m^2 s^{-1}
D_0	diffusion rate coefficient	s m^{-1}
E_a	exponential factor	J mol^{-1}
F	averaged variable	various
h	reaction enthalpy	J kg^{-1}
k	heat conductivity	W m^{-1} K^{-1}
$k_{c,i}$	intrinsic reactivity	s m^{-1}
k_d	mass transfer coefficient	m s^{-1}
m	mass	kg
M	molar mass	kg mol^{-1}
p	pressure	Pa
$\dot{r}$	reaction rate	kg s^{-1}
r	radius	m
R	reaction rate	s^{-1}, s m^{-1}
R_u	universal gas constant	J mol^{-1} K^{-1}
S_b	mass stoichiometric coefficient	-
Sh	Sherwood number	-
t	time	s
T	temperature	K
v	volume fraction	-
V	volume	m^3
X	conversion	-

Greek symbols

α	yield parameter	-
β	diameter evolution coefficient	-
ε	emissivity	-
η	effectiveness factor	-
θ	coefficient related to Stefan flow	-
θ	porosity	-
ν	stoichiometric coefficient	-
ρ	density	kg m^{-3}
σ	characteristic length	Å
τ	tortuosity	-
ϕ	Thiele modulus	-
φ	swelling magnitude	-
Ψ	structural parameter	-
Ω	collision integral	-

Subscripts

0	initial
A	substance A
AB	between A and B
B	substance B
c	carbon
dry	dry, ash included
D	diffusion
DAF	dry, ash free
e	effective
inf	final, infinity
kn	Knudsen
n	n:th variable
p	particle

Abbreviations

CCS	carbon capture and storage
CFD	computational fluid dynamics
DAF	dry ash-free
DTR	drop-tube reactor
TGA	thermogravimetric analysis

Contents

ABSTRACT **i**

PREFACE **iii**

LIST OF PUBLICATIONS **v**

LIST OF SYMBOLS AND ABBREVIATIONS **vii**

1 Introduction **1**

2 Background **3**
2.1 Significance of solid fuel combustion 3
2.2 Alternatives to fossil coal 4
2.3 Thermal pretreatment methods of biomass 5
2.4 Solid fuel characterization 6

3 Solid fuel combustion modeling **9**
3.1 Particle energy balance 9
3.2 Pyrolysis 11
3.3 Particle motion 12
3.4 Char oxidation 13
3.5 Gas diffusion 17
3.6 Particle size evolution 18
3.7 Combustion modeling calculation procedure 19

4 Experimental **23**
4.1 Tested fuels 23
4.2 Sample grinding and sieving 25
4.3 Mercury porosimeter 27
4.4 Drop-tube reactor 29
4.5 Two-color pyrometer 31
4.6 High-speed camera 31
4.7 Particle size and geometry analysis 32
4.8 Torrefaction reactors 33
4.9 Fine grinding energy measurement 34

5 Results and discussion **35**
5.1 Physical property characterization 35
5.1.1 Effect of torrefaction on fine grinding energy 35
5.1.2 Biomass pellet fine grinding energy and resulting particle geometry 36
5.2 Drop-tube reactor test results and reactivity characterization 38
5.2.1 Mass loss 38
5.2.2 Particle geometry evolution 43
5.2.3 Particle surface temperature 49
5.2.4 Fitted parameters 53
5.2.5 Sample reactivity comparison 54

6 Summary and conclusions **57**

7 Future work **59**

Bibliography **61**

Appendix: Original publications **67**

Chapter 1

Introduction

Solid fuel combustion nowadays accounts for well over 40% of the world's electricity generation. Today, the world, and especially the developing countries such as China and India, is facing an increasing growth in the demand for electrical power. In order to keep up with the demand, new power plants are being built at a remarkable rate. The majority of recently constructed and planned power plants, on a world-wide basis, are coal-fired. Coal is considered to be cheap and an abundant resource, while at the same time being a very reliable fuel for power production. However, the ever increasing concern about the environmentally harmful effects of fossil fuels has led to a search for cleaner alternatives. Various biomass feedstocks have already been used as replacement fuels for fossil coal. These biomass based fuels tend to have significantly different combustion characteristics compared to coal and also one another. Their reactivity, ash chemistry [1], and volatile composition may cause difficulties in predicting the furnace performance the feedstock is used in. Moreover, the thermal and chemical pretreatment methods used to upgrade biomass quality further alter the combustion characteristics of the feedstock.

Various biomass feedstocks can be considered as fuel sources capable of replacing fossil coal, to some extent even in existing power plants. However, compared to coal these fuels have different pyrolysis and combustion properties. The cofiring of coal and biomass blends has been found to produce flammable gaseous mixtures even at low pyrolysis temperatures (e.g. 150°C) [2]. Therefore, their usage in power plants requires more in-depth information about their behavior in the aforementioned processes. Biomass feedstocks also have inferior storage and transportation properties compared to fossil coal. Therefore, thermochemical technologies have been developed to upgrade biomass quality.

Torrefied wood is thermally pretreated wood that has some of the good properties of fossil coal, such as hydrophobicity. The benefit of torrefied wood as a fuel is its ability to withstand outdoor storing without rapidly losing its heating value. Compared to untreated wood it is also easier to grind [3, 4]. Moreover, torrefied wood can be considered to be carbon dioxide neutral fuel. An alternative technology of upgrading biomass feedstock is steam-explosion. Steam-explosion is a process where the water inside the pores of biomass tissue undergoes adiabatic

expansion. This results in both mechanical deformation and chemical degradation of the feedstock [5]. Many energy production companies have expressed interest in these technologies and already the first commercial products have become available. Nevertheless, the effects of torrefaction and steam-explosion on biomass pyrolysis and combustion have yet to be studied in depth. In recent years, along with this thesis, there has been an increasing interest in this issue and multiple new studies have been published [6–13].

Laboratory-scale testing provides useful and necessary information on solid fuel behavior during pyrolysis and combustion. This information can be used later on when designing larger power plants and burning facilities. A DTR can be used to simulate the temperature level, atmosphere, and especially the high heating rates of fluidized bed combustion and pulverized fuel firing. Therefore, a DTR was chosen as the main study instrument in this thesis. Along with the DTR, this thesis presents a combination of optical and physical measurement techniques to complement mass loss experiments in reactivity studies. The combustion tests were conducted both in O_2/N_2 or O_2/CO_2 atmospheres. This enabled examining the role of CO_2 gasification on the results. This thesis also shows how important it is to use kinetic modeling when comparing the reactivities of solid fuels. Using a combination of the study methods presented here could be called advanced fuel characterization. It covers the study chain starting from the sample fuel grinding tests and optical geometry analysis, followed by DTR reactivity tests and numerical kinetics modeling.

Chapter 2

Background

2.1 Significance of solid fuel combustion

In 2014 well over a quarter of the world's total primary energy supply came from fossil coal [14]. The most significant application of coal is electricity generation, accounting for more than 40% of global electricity production. Other uses include, for example, steel production and cement manufacturing. Coal is geographically the most widely available and distributed fossil fuel energy resource. The largest coal reserves are in the by USA, Russia, China, and India [15]. The most common way to burn coal in large steam-generating units is to grind and inject the powder into a furnace flame with a stream of air. Fluidized bed combustion is an alternative to the more traditional pulverized fuel firing.

Coal has a significant role in energy production throughout the world. However, it also has harmful environmental effects, such as the widely acknowledged impact on climate change through its CO_2 emissions. Therefore, new clean and environmentally friendly combustion technologies need to be developed if the use of coal continues. One possibility for limiting CO_2 emissions is carbon capture and storage (CCS) technology. Several technologies are being developed for CO_2 capture and sequestration from coal-fired plants. Among them, oxy-fuel combustion is considered as one of the most economical alternatives [16]. It is also the most probable technology to be employed when retrofitting existing coal-fired power plants [17]. However, there are still several obstacles to overcome before oxy-fuel combustion can fully be commercialized. One critical issue is to study how the elevated CO_2 concentration affects the reaction rate of the fuel particles. High CO_2 concentrations can change the fuel particle overall reaction rate through gasification or possibly through interfering the oxidation reaction. Especially when co-firing biomass feedstocks with fossil coal, it is of great importance to know how the flue gas recirculation affects the burnout times of the particles. Other issues related to biomass combustion are the complex chemical reactions of the ash-forming matter. These issues have been extensively studied by, e.g. Mikko Hupa's research group from Åbo Akademi University [18].

It would appear that as never before, the future of energy production seems unclear. The operating life of an industrial scale boiler is measured in tens of years. The ever changing economic, environmental, and political situations mean that in the future power production boilers will have to be rather versatile in terms of fuel type. This development poses a huge challenge for boiler manufacturers and designers. For this, an accurate and comprehensive method of characterizing solid fuels is needed.

2.2 Alternatives to fossil coal

Solid fuels in general can be divided into fossil and renewable fuels. Coal originates from the remains of prehistoric vegetation that originally accumulated in swamps and peat bogs. Coal is fossil fuel by any standards, but there has been some controversy on the classification of peat. Nevertheless, the United Nations and the Intergovernmental Panel for Climate Change have classified peat as a fossil fuel due to its slow regrowth rate [19, 20]. Carbonaceous fuels in general are collections of organic polymers. These polymers consist mainly of aromatic chains combined by hydrocarbons and atoms such as oxygen, sulfur, nitrogen, potassium, and sodium [21]. Biomass is a term used for organic material of living, or recently living, organisms. Usually it means plant-based materials which are more specifically called lignocellulosic biomass. From these three, fossil coal, peat, and biomass, coal is by far the easiest to use in energy production. It is easy to store, it has hydrophobic properties, and it is easy to grind. Moreover, the supply chain for fossil coal is more centralized compared to biomass or peat. Biomass also tends to chemically degrade during storage, it contains a lot of harmful chemicals which can lead to boiler corrosion, and it is partially a seasonal fuel.

The direct co-combustion of coal and secondary fuels, such as heat treated biomass, in a pulverized fuel firing boiler is considered a very convenient method to replace part of the fossil coal consumption [22]. One likely application of thermally pretreated biomass is to co-fire it with fossil coal in pulverized fuel furnaces. Peat has been studied to be a beneficial co-firing fuel even with coal, while it has been noted to reduce ash deposition rates [23]. It can also reduce the corrosive effects of various types of biomass in power production furnaces [24]. The combustion behavior of biomass feedstocks in general are not as well defined as with coal. Furthermore, if novel combustion technologies, such as flue gas recirculation or gasification of the feedstock are applied, information on the fuel reactivity in reducing atmosphere is required. Especially in the case of torrefied and steam-exploded biomasses, this type of information is not yet available.

When comparing coal and biomass, there are several differences. The most distinctive differences are the chemical composition and fiber structure of biomass. These factors result in very different combustion and pyrolysis behavior. For instance, compared to coal, biomass produces much less char and more volatiles during the pyrolysis process. From a chemical perspective, the high amount of volatiles in biomass is due to the high O/C and H/C ratios. The Van Krevelen diagram [25] in Figure 2.1 shows these ratios for different solid fuels.

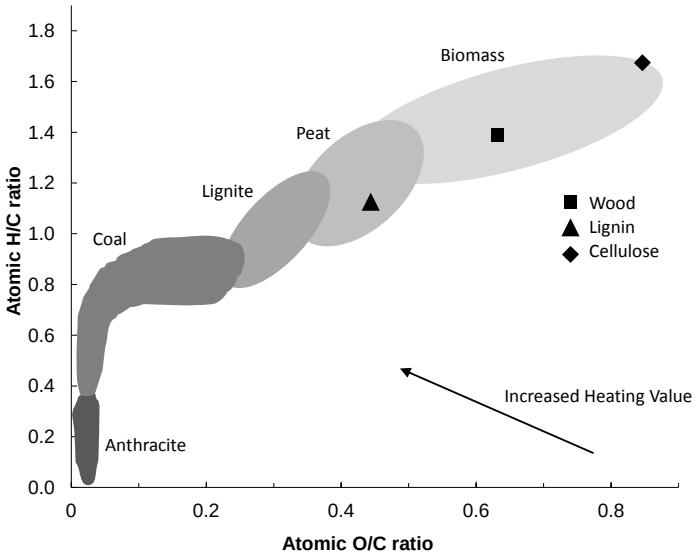

Fig. 2.1: Van Krevelen diagram for various solid fuels. [25]

Figure 2.1 shows how the decomposition of biomass changes the chemical structure of solid fuels. A more detailed description on the placement of various solid fuels in the diagram can be found in [26]. On top of the differences in the elemental composition between coal and biomass, the latter tends to always be at least somewhat anisotropic. This poses many challenges to modeling intraparticle mass and heat transfer, especially in larger particles.

Biomass particles are typically larger than pulverized coal particles [27]. It is not usually economically feasible to process the biomass feedstock to the same particle size as brittle coal. However, studies show that with thermochemical pretreatment methods it is possible to reduce the grinding energy of biomass. This thesis also shows that grinding steam-exploded biomass produces rather round particles. To bring biomass feedstocks to the same level as fossil coal in terms of storage, grinding, and overall furnace performance, it is necessary to be able to quantify the effects of these thermochemical methods on biomass quality and reactivity.

2.3 Thermal pretreatment methods of biomass

There are various methods to improve biomass feedstock properties regarding efficiency of utilization. The methods can be mechanical, thermal, chemical, or a combination of these. Dewatering and size reduction or pulverization are examples of mechanical treatments. These processes can be further continued by pelletizing or bricketizing the material for easier transport. Drying can be considered as purely thermal treatment, whereas torrefaction and steam-explosion, on the other hand, also involve chemical changes in the feedstock.

Torrefaction is a process in which the biomass feedstock is heated in an inert atmosphere in the temperature range of 225-300°C [28, 29]. Torrefied wood has some of the good properties of fossil coal, such as hydrophobicity. The acclaimed benefits of torrefied wood as a fuel include its ability to withstand outdoor storage without losing its heating value. Compared to untreated wood it is also easier to grind, as stated in [4,30]. Moreover, torrefied wood can be considered as a carbon dioxide neutral fuel, since its raw material is woody biomass. Therefore, in the world of emissions trading, many energy production companies have expressed increasing interest in it. Nevertheless, the effects of torrefaction on the biomass feedstock quality and also on the pyrolysis and combustion processes are not fully known. Since torrefied wood has been planned as a replacement fuel for fossil coal, it is important that kinetics studies would be conducted with fossil coal references.

Steam explosion is a process where the water inside the pores of biomass tissue undergoes adiabatic expansion. It results in both mechanical deformation and chemical degradation of the feedstock [5]. Lignocellulosic biomass is first heated to elevated temperatures with high pressure steam, and afterwards subjected to explosive decompression. The treatment temperature ranges mentioned in the literature start typically from 180 ending up to 250°C. The corresponding pressure range is approximately 10-50 bar. This process physically and chemically modifies the biomass [31]. Steam explosion can be considered an attractive method of upgrading biomass because a high degree of defibration can be achieved without the addition of chemicals. Therefore, chemical, material, and environmental costs are reduced [32]. Lam reported in his thesis [33] that untreated pellets and steam exploded pellets required respectively 4.83 MJ kg^{-1} and 7-8 MJ kg^{-1} energy to produce. Although more energy was needed to produce the steam-exploded pellets, the quality of the product was improved in terms of mechanical strength, grindability, energy density and hydrophobicity.

2.4 Solid fuel characterization

In order to efficiently utilize the biomass resources in existing and future power plant furnaces, it is essential to examine the combustion properties of different biomass feedstocks. Due to their different chemical and physical structure the devolatilization and char oxidation rates of biomasses are in some cases very different than those of fossil coal. Computational fluid dynamics (CFD) calculation enables the designing of better combustion systems in terms of emission reduction, minimizing the amount of unburnt matter, and reducing slagging and fouling. The CFD program sub-models describe the combustion behavior of a single fuel particle. Therefore, exact information is needed on the fuel properties and reactivity. The research chain should begin with determining the fuel physical properties, moving on to reactivity tests, and finally applying kinetics modeling to extract the needed variables from the measurement data.

Standardized ultimate and proximate analysis along with fuel heating value tests offer the basic information needed for fuel characterization. With these analyzes some effects of thermal treatment methods on the fuel properties can

be evaluated. Publication IV, for example, addresses the issue of changes in the fuel heating value and decreased chlorine content in woody biomasses due to torrefaction. In addition to standardized analysis methods, more case sensitive analyzes, such as mercury porosimeter based density, fuel particle fine grinding energy requirement and resulting particle size distribution can also be used. Such results are presented in Publication I and V. Some of these analysis results can be used as supplementary information in the kinetics modeling. However, the fuel reactivity data has to be measured separately.

Laboratory-scale reactivity testing can provide useful and necessary information on solid fuel behavior during pyrolysis, combustion and gasification. The gathered data has to be usually refined with kinetic modeling to the needs of the CFD sub-models. Plenty of laboratory-scale reactivity research equipment has been developed for pyrolysis and combustion research. This equipment can, depending on the design, examine single particles, a batch of the sample, or a continuous feed of the feedstock, e.g. to flame. One of the most common commercially available devices is one that uses a methodology called thermogravimetric analysis (TGA). These thermogravimeters are well suited for low heating rate experiments. However, industrial size furnaces always have heating rates several magnitudes higher than in TGA devices. Many other setups with higher heating rates are presented in the combustion literature. Karlström et. al. used a single particle reactor to examine the NO formation from large char particles [34]. In their reactor, a sample particle could be suspended into the reactor in a thin net. This also enabled visual observation of the sample. Weber et. al. have presented a small scale vertical combustion chamber for comparison of solid fuel flame properties [35]. The test reactor was especially designed for pulverized fuel firing studies. Mitchell has used an entrained laminar flow reactor in many of his studies, e.g. [36] and [37]. The reactor design consists of a rectangular array of diffusion flamelets on the bottom which provide heat for the system and a sampling probe which is used to collect the particles traveling upwards.

A DTR, on the other hand, can be used to simulate the temperature level, atmosphere, and especially the heating rate of industrial processes. Among others, [38] have noticed that pyrolysis kinetics change substantially when the heating rate varies. DTR systems are well suited for fossil coals, and recently they have also been used in many biomass reactivity studies, e.g. [39]. The measurement setup used in this work enabled the investigation of the sample particles' actual size and shape before and after the pyrolysis and combustion processes, the mass loss resulting from the reactor treatment, the particle surface temperature during combustion, and the particle falling velocity inside the reactor. This advanced solid fuel characterization study chain was further complemented with numerical kinetics modeling.

The value of kinetic modeling is not just that it produces information for CFD calculation. It is also crucially important when conducting fuel sample reactivity comparison. Exempli gratia the DTR measurement results produced in this work cannot be directly compared to one another, even though the residence times of the particles are known based on the velocity measurements. The external temperature profile a falling particle experiences inside the reactor is not

a step change; instead there is always some thermal inertia in the reactor gas and wall temperature profiles. Therefore, particles falling at different velocities have different external temperature histories. Even though two different samples might share a common residence time in the reactor, their temperature histories might be significantly different. With kinetic modeling, the reactivity data can be first determined based on the measurements and the sample particles can be exposed to the same simulated environment.

Chapter 3

Solid fuel combustion modeling

This chapter presents the phenomena related to the combustion process of a solid fuel particle. Moreover, the equations used in the models of this work are presented. The combustion process of a solid fuel particle can be divided into stages. The first stage is drying, where moisture starts to evaporate from the particle. Drying is followed by pyrolysis, during which the organic matter in the particle thermochemically decomposes. In other words, pyrolysis is a set of cracking reactions of big molecules into smaller ones. The release of the volatile matter from the solid part is referred to as devolatilization. The remaining solid part consists of carbon, referred to as char, and inorganic material, referred to as ash. Char oxidation or gasification is the final part in the combustion process. During this step the remaining char in the particle reacts chemically with an oxidizing or a gasifying agent, usually O_2 or CO_2, forming CO or CO_2. In pyrolysis the driving force is heat transfer from the exterior into the particle, whereas in char oxidation it is the reaction heat generated from the reaction itself. All of these phenomena can at least to some extent overlap, depending on the reaction conditions and the fuel type.

3.1 Particle energy balance

An essential part of modeling solid fuel combustion under high heating rates is knowing the particle temperature history. The environment temperature related to thermal radiation and convection can usually be measured. However, depending on the fuel particle size and properties, the particle internal temperature has to be calculated based on heat transfer correlations. The general energy balance equation for a combusting fuel particle can be written as (e.g. [40]):

$$\frac{\partial \left(\rho_p T_p\right)}{\partial t} = \frac{1}{c_p}\frac{1}{r^2}\left(\frac{\partial}{\partial r} r^2 k_p \frac{\partial T_p}{\partial r}\right) + \frac{1}{c_p}\dot{r}\left(-\Delta h\right) \tag{3.1}$$

where ρ_p is the density of the particle (kg m^{-3}), c_p is the heat capacity of the particle (J kg^{-1} K^{-1}), t is the time (s), r is the radius of the particle (m), k_p is the heat conductivity (W m^{-1} K^{-1}), and T_p is the temperature of the particle (K). The sink or source term $\dot{r}$ can, depending on the case, depict pyrolysis, char oxidation, or char gasification rates (kg s^{-1}). The termΔh is the reaction enthalpy (J kg^{-1}) related to the considered reaction. The left hand side term of the equation describes the energy storage in the particle. The first term on the right hand side describes the heat conduction and the second term the internal heat generation or consumption from the chemical reactions. At the particle center point the heat flux can be assumed to be zero. Depending on the particle size, the particle can be assumed to be thermally thin, which makes the calculation simpler. However, the energy balance equation can rather easily be solved numerically with the implicit method. This approach was used in the calculations of this compilation work.

The heat transfer boundary condition on the particle surface can be written as:

$$-k_p \frac{\partial T_p}{\partial r} = \theta h_c \left(T_{gas} - T_p\right) + \varepsilon\sigma \left(T_{wall}^4 - T_p^4\right) \tag{3.2}$$

where θ is a coefficient related to the Stefan flow (-), h_c is the convective heat transfer coefficient (W m^{-2} K^{-1}), T_{wall} is the reactor wall temperature (K), T_{gas} is the gas temperature (K), ε is the emissivity of the particle (-), and σ is the Stefan–Boltzmann constant (W m^{-2} K^{-4}). The left hand side term describes the heat conduction. The first right hand side term describes the heat convection between the particle and the surrounding gas. The second right hand term describes the radiative heat transfer between the wall and the particle. The heat conductivity inside the particle consists of the actual heat conduction in the solid matter, but also of the heat conduction through the gases in the particle voids and the radiation between the void surfaces. In the compilation part calculation however, a constant value of 0.1 W m^{-1} K^{-1} was used. The heat transfer coefficient was calculated with the Ranz Marshall [41] correlations. This is by far the most common way used in the combustion literature. The emissivity of the particle in the radiation term was assumed to be 0.9 in all cases throughout the conversion process.

There are various correlations and measurement results presented in the literature for biomass and coal specific heat capacities [42–46]. However, due to the uncertainties related to the measurement of the specific heat capacity at high temperatures in this work, a constant value of 1500 J kg^{-1} K^{-1} was used based on the heat capacity correlations presented in [47]. This value was used with all fuels in both the pyrolysis and the combined pyrolysis and char oxidation case calculations. The value represents the combined heat capacity of the unreacted part of the particle, the formed char, and the voids filled by the gases. When comparing the results of this thesis with other literature work, it is crucial to take this simplification into consideration.

The term θ in the convection part of the energy balance equation, describing the effect of Stefan flow, was used as presented in [48]. The following correlation applies to the Reynolds numbers up to 400 [49]:

$$\theta = e^{(-0.6B)} \tag{3.3}$$

where the term B is related to the devolatilization rate and the gas properties (-):

$$B = \frac{c_{gas}}{2\pi d_p k_g} \left(\frac{dm_p}{dt} \right) \tag{3.4}$$

The heat capacity c_{gas} (J kg^{-1} K^{-1}) and the conductivity k_g (W m^{-1}K^{-1}) of the product gas were assumed to be the same as for the environment since there was no actual knowledge of the volatiles' composition. The term m_p is the mass of the particle (kg) and d_p is the particle diameter (m).

3.2 Pyrolysis

Solid fuel particle pyrolysis is a complex series of chemical reactions where the main driving force is heat transfer from the exterior to the particle. When constructing a pyrolysis model, usually it should consider the fuel properties, the reactions taking place, and the generated products. Regardless of the fuel type, usually pyrolysis products can be divided into three different types: the solid char, the liquid tar, and gaseous products referred to as gas. The amount of char is dependent on the fuel type, pyrolysis temperature, heating rate, and particle size. For coal, at temperatures of 1073-1173 K, the amount of pyrolysing mass is usually 20-50% of the initial particle. For peat, the proportion is higher, 60-70%, and for wood over 80%. Small biomass particles under high heating rates can be transformed almost entirely to gas and tars.

The exact chemical reactions taking place during pyrolysis are not known, and thus the exact modeling of them is not possible, nor practical. However, there are various models describing pyrolysis chemical kinetics. These models do not necessarily describe accurately the physical and chemical processes taking place during pyrolysis, but rather they correlate the empiric information.

The pyrolysis model used in the compilation part of this thesis was proposed by Kobayashi [50]. The model was selected in a way that the kinetic parameter results can easily be utilized in commercial computational fluid dynamics programs, such as Ansys Fluent. The volatile yield $m_v\,(t)$ (kg) at a given time t (s) can be written as:

$$m_v\,(t) = m_{0,DAF} \int_0^t (\alpha_1 R_1 + \alpha_2 R_2) \exp\left(- \int_0^t (R_1 + R_2)\, dt \right) dt \tag{3.5}$$

where α_1 and α_2 are the so called yield parameters (-), $m_{0,DAF}$ is the dry ash free initial mass of the particle (kg), and R_1 and R_2 are the competing reaction rates (s^{-1}). Here, the two global reactions include hundreds, if not thousands of elementary chemical reactions in themselves. The model does not consider any intermediate products, only virgin solid matter, the formed char, and the released volatile gases. The competing reaction rates can be expressed in the

form of the Arrhenius equation, which is the most common form used in reaction rate modeling:

$$R_n = A_n \exp\left(-\frac{E_{a,n}}{R_u T}\right) \tag{3.6}$$

where A_n is the pre-exponential factor of the reaction rate coefficient (s^{-1}), $E_{a,n}$ is the exponential factor of the reaction rate coefficient (J mol^{-1}), R_u is the universal gas constant (J $mol^{-1}K^{-1}$), and T is the reaction temperature (K). If the reaction rate were to be written to a single elementary reaction, the terms A_n and $E_{a,n}$ could be called the frequency factor and the activation energy, and they would have an actual physical meaning.

The reaction enthalpy of a high heating rate pyrolysis process is hard, if not impossible to determine. Simultaneous Thermal Analysis, which combines differential scanning calorimetry and thermogravimetry, can be used to determine reaction enthalpies at low heating rates. Often in a DTR environment, however, a constant slightly endothermic value is used. The same procedure was applied also in this work. A value of 120 kJ kg^{-1} was used, as suggested by Lehto for peat [51]. Moreover, with small particles the heat convective transfer coefficient and thus the heat flux into the particle from the exterior is so strong that the pyrolysis reaction enthalpy plays only a minor role in the fuel particle temperature history.

3.3 Particle motion

The particle motion inside the DTR has been in many cases solved based on the motion equation. This approach is valid when the properties and shape of the particle are well known during the pyrolysis or combustion process. Coal particles, for example, tend to maintain their shape, and the density of the falling particles can be evaluated based on the mass loss and particle size. However, biomass particles tend to be much more irregular shaped and the drag coefficient related to the motion inside the DTR is hard to determine. Rather than trying to estimate the particle velocity based on motion equation, in this thesis the velocity of the particles was measured. The measurement procedure is further discussed in Publication II and [52]. The greatest shortcoming of this method is that even though it is possible to determine the particle falling velocity rather accurately, the slip velocity, i.e. the velocity between the gas and the particle, has to be estimated. The slip velocity affects especially the convective heat transfer coefficient and thus the heating rate of the particle. Based on the falling velocities of the smallest and almost completely burned particles, the terminal velocities of which were close to zero, the average gas velocity was determined to be 0.35 m s^{-1}. The slip velocity between the particles and the gas could be estimated based on this average gas velocity and the particle velocity profiles. The sensitivity of the slip velocity on the model calculations was tested by multiplying it to tenfold. The difference in the results was minor. Therefore, it could be stated that the possible error in the slip velocity estimation had hardly any effect on the final results. However, in the long term it would be appropriate to use CFD analysis

to more accurately determine the velocity difference between the particles and the gas.

3.4 Char oxidation

Char oxidation is a series of intermediate reactions where the reactants are solid carbon, i.e. char, and O_2 and the final products are CO and CO_2. The ratio between the CO and CO_2 depends on the O_2 concentration and the reaction temperature. The general understanding is that at higher temperatures the CO production is dominant [53]. The main mechanisms controlling the char oxidation apparent reaction rate are the boundary layer diffusion, diffusion in the particle pores, and the chemical kinetics. In the combustion literature generally three different cases are defined in which the reaction rate controlling factors differ from one another. These cases are called Regime I, Regime II, and Regime III. A graphical illustration of the reaction rate controlling factors and O_2 concentrations under the three different regime conditions is given in Figure 3.1.

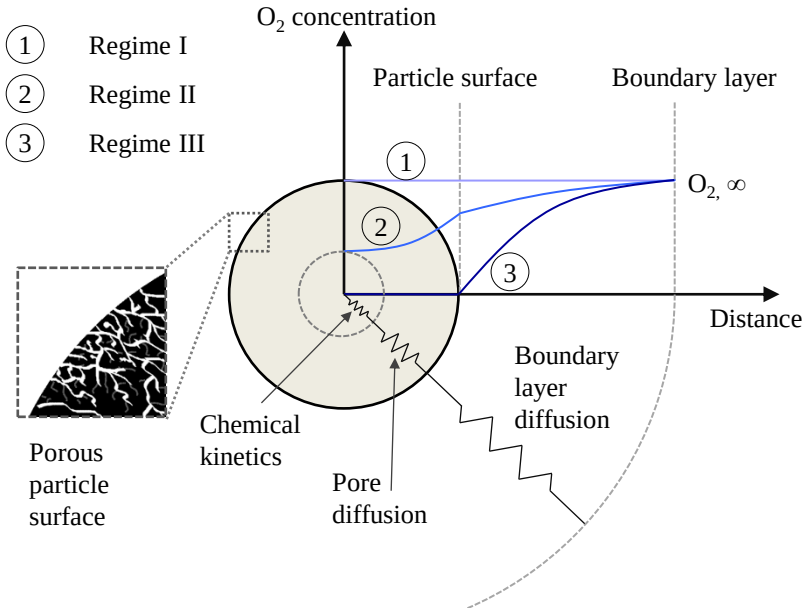

Fig. 3.1: Depiction of the phenomena related to porous char particle oxidation.

Under Regime I conditions the particle is small and the oxidation reaction is slow due to low temperature. Therefore, the O_2 concentration inside the particle is uniform. The oxidation reaction rate is controlled by the chemical kinetics and the oxidation reactions occur evenly throughout the particle. Under Regime III conditions the particle is large and the temperature is high. The O_2 concentration inside the particle approaches zero. All the char oxidation occurs in the particle

surface. The process is controlled by the O_2 boundary layer diffusion. Regime II is an intermediate state between Regime I and III. The oxidation process is controlled by the external boundary layer diffusion, internal pore diffusion, and the chemical kinetics. A concentration gradient of O_2 forms inside the particle and outside as well. How steep the gradient is depends on whether the conditions are closer to Regime I or III.

The oxidation affects the particle size in a different way under different regimes. Under Regime I conditions the particle is saturated by the O_2 and the oxidation reaction occurs throughout the particle at a uniform rate. The apparent size of the particle remains constant and its density decreases. Under Regime III conditions the oxidation reaction only occurs on the particle surface. Therefore, the particle density remains constant and its size decreases. Regime II conditions are again a combination of the two latter cases. Both the particle size and density decrease simultaneously. In real combustion systems the combusting particles have a size distribution and both the temperature and the O_2 concentration are dependent on time and place. Therefore, combustion may occur under all of the regimes. Even in the DTR tests of this thesis, in which the combustion process is well controlled, different combustion modes are present. Figure 3.2 shows the sometimes chaotic nature of the combustion process of coal char particles under 21 vol-% of O_2.

Fig. 3.2: Coal combustion under high O_2 concentration.

The larger particles fragment forming many smaller ones. The small particles may be close to Regime I conditions, whereas the larger ones are closer to Regime III. The temperature is over 2000 K and the oxidation reactions are fast. The medium sized particles experience the combined reaction rate controlling effects of chemical kinetics and O_2 diffusion, Regime II.

A commonly used approach in the combustion literature, e.g. [54], to calculate the char oxidation reaction rate is to use the intrinsic model [55]. The intrinsic model takes into account the extra- and intraparticle diffusion of the oxidizing agent, as well as the chemical kinetics. Therefore, it is applicable to all of the

combustion regimes. The following equations related to the intrinsic combustion model are presented in many sources. However, many of the sources do not include units or clear explanations of the relation between the presented equations. Therefore, the equations are presented and discussed here. The equations and their source material are presented also in, e.g. [56]. To avoid confusion, the terms were named similarly as in the mentioned source.

The mass loss rate related to the reaction between char and oxygen can be expressed in terms of the kinetic rate and the diffusion rate coefficient as:

$$\frac{dm_p}{dt} = -A_p p_{O_2\infty} \frac{D_0 R}{D_0 + R} \tag{3.7}$$

where A_p is the spherical equivalent diameter based area of the particle (m^2), $p_{O_2\infty}$ is the partial pressure of oxygen outside the boundary layer (Pa), R is the kinetic rate of the reaction (s m^{-1}), and D_0 is the diffusion rate coefficient related to the diffusion of oxygen through the boundary layer (s m^{-1}). The reaction order is assumed to be equal to unity.

The effect of pore diffusion is taken account in the kinetic rate of the reaction:

$$R = \eta \frac{d_p}{6} \rho_p A_g k_{c,i} \tag{3.8}$$

whereη is the effectiveness factor (-), d_p is the equispherical diameter of the particle (m), ρ_p is the density of the particle (kg m^{-3}), A_g is the internal surface area of the particle (m^2 kg^{-1}), and $k_{c,i}$ is the intrinsic reactivity (s m^{-1}). The internal surface area can be measured, e.g. based on gas adsorption or, as in this work, with a mercury porosimeter. Another issue, which could not be addressed in this thesis, is to cover the surface area evolution during the combustion process. The DTR system used in this work is suitable for producing the partially combusted particles for such surface area tests. The most suitable measurement system for such experiments would be gas sorption based analyzer.

The char oxidation reaction rate coefficient is of the Arrhenius form:

$$k_{c,i} = A_c e^{\left(-\frac{E_{a,c}}{R_u T}\right)} \tag{3.9}$$

where A_c is the pre-exponential factor (s m^{-1}), E_a is the exponential factor (J mol^{-1}), R_u is the universal gas constant (J $mol^{-1}K^{-1}$), and T is the reaction temperature (K). The reaction temperature can be solved from the energy balance equation for a thermally thin particle when the reaction temperature is uniform throughout the particle, or for separate intraparticle elements.

The mass transfer inside the particle could be solved, like heat transfer in this work, numerically. However, the numerical solution for the intraparticle O_2 concentration was very troublesome in terms of calculation time and stability. Thus, instead of the numerical solution, Thiele modulus was used. The effectiveness factor η in the kinetic rate equation describes the ratio of the actual reaction rate to the rate with no pore diffusion limitation:

$$\eta = \frac{3}{\phi^2} \left(\phi \coth\left(\phi\right) - 1\right) \tag{3.10}$$

where ϕ is the so called Thiele modulus:

$$\phi = \frac{d_p}{2}\left[\frac{S_b \rho_p A_g k_{c,i} p_{O_2}}{D_e \rho_{O_2}}\right]^{\frac{1}{2}} \tag{3.11}$$

where S_b is the mass stoichiometric coefficient related to the char oxidation reaction to CO (-), ρ_{O_2} is the density of the oxidant (kg m^{-3}), p_{O_2} is the oxygen partial pressure (Pa), and D_e is the effective diffusion coefficient inside the particle (m^2 s^{-1}). The oxygen partial pressure p_{O_2} and the density of the oxidant ρ_{O_2} can be assumed to be the same as outside the boundary layer in cases where the boundary layer diffusion is fast compared to the chemical reaction rate. Otherwise, the terms should be calculated on the particle surface or in the boundary layer. The effective diffusion coefficient takes into account the molecular and Knudsen diffusion effects:

$$D_e = \frac{\theta}{\tau^2}\left[\frac{1}{D_{kn}} + \frac{1}{D_{AB}}\right]^{-1} \tag{3.12}$$

where θ is the porosity of the particle (-), τ is the tortuosity of the pores (-), and D_{kn} in turn is the Knudsen diffusion coefficient (m^2 s^{-1}):

$$D_{kn} = 97\bar{r_p}\sqrt{\frac{T_p}{M_{O_2}}} \tag{3.13}$$

where $\bar{r_p}$ is the mean pore radius of the particle (m), and M_{O_2} is the molecular weight of O_2 (kg mol^{-1}), in this case, oxygen. Determining the molecular binary diffusion coefficient D_{AB} (m^2 s^{-1}) is discussed further in the following chapter.

The specific surface area describes the area available for the chemical reactions to occur. The area first grows when the pores are opened as the oxidation reactions consume the pore walls. At some point the area starts to decrease as the pores begin to merge. The specific surface area change during conversion can be calculated according to the Bhatia-Perlmutter random pore model widely used in the combustion literature [57]:

$$A_g = A_{g,0}\sqrt{1 - \Psi \ln\left(1 - X_{dry}\right)} \tag{3.14}$$

where $A_{g,0}$ is the initial specific surface area (m^2 kg^{-1}), X_{dry} is the dry form of conversion, and Ψ is the structural parameter (-). There are correlations to calculate the structural parameter or it can be a fitted coefficient based on experimental data [58] and [59]. In this work, due to the lack of experimental data, the parameter, was set as 10 for all the tested fuels. The use of the Bhatia-Perlmutter approach in the model calculations is somewhat questionable since the model was developed for coal char oxidation under Regime I conditions. In this work it was applied to the combined pyrolysis and char oxidation of coal and biomasses under Regime II. During the combined pyrolysis and char oxidation process the pore structure evolution is likely to be different than the equation predicts. However, it is likely that as the pyrolysis gases erupt from the particle, the pore size and the specific surface area grow. Moreover, later as the pores inside

the residual char particle start to merge, the area decreases. Since there was no accurate information on the actual pore structure and surface area evolution of the sample particles, a commonly used model was applied to give at least a rough estimation of the phenomenon.

3.5 Gas diffusion

The mass transfer processes of a combusting spherical particle can be described with the following differential equation, which is Fick's second law for one-dimensional diffusion in radial direction for spherical coordinates:

$$\frac{\partial C}{\partial t} = \frac{1}{r^2}\left(\frac{\partial}{\partial r} r^2 D \frac{\partial C}{\partial r}\right) + \dot{C} \tag{3.15}$$

where C is the gas concentration (mol m^{-3}), D is the diffusion coefficient (m^2 s^{-1}), r is the radius (m), and the last sink or source term $\dot{C}$ describes the consumption or generation of the diffusing gas species due to chemical reactions (mol m^{-3}s^{-1}). Usually the boundary condition on the particle surface is calculated based on gas film diffusion theory. One of the most common approaches to model gas film diffusion is to use a simple integrated form of Fick's Law [60]:

$$\dot{N}''_{gas} = k_d \left(C_{gas,\infty} - C_{gas,s}\right) \tag{3.16}$$

where $\dot{N}''_{gas}$ is the molar flow of gas through a surface (mol s^{-1} m^{-2}), $C_{gas,\infty}$ is the concentration of the gas outside the boundary layer, and $C_{gas,s}$ is the gas concentration on the particle surface. The concentration of the boundary layer is usually calculated at the mean temperature of the bulk gas and the particle surface. The same approach is used in determining the gas properties. The mass transfer coefficient k_d (m s^{-1}) can be calculated from the Ranz Marshall correlation expressing the Sherwood number as a function of the Reynolds and Schmidt numbers:

$$k_d = \frac{Sh D_{AB}}{d_p} \tag{3.17}$$

where Sh is the Sherwood number (-). The binary diffusion coefficient can be calculated, e.g. according to [61]:

$$D_{AB} = \frac{266 T^{\frac{3}{2}}}{p (M_{AB})^{\frac{1}{2}} \sigma_{AB}^2 \Omega_D} \tag{3.18}$$

where D_{AB} is the diffusion coefficient (in this equation cm^2 s^{-1}, usually m^2 s^{-1}), T is the temperature (K), p is the pressure (Pa), and σ_{AB} is the characteristic length (Å). The term Ω_D is the diffusion collision integral (-) and its calculation along with the needed tables is presented also in [61]. The term M_{AB} can be calculated as:

$$M_{AB} = 2\left[\frac{1}{M_A} + \frac{1}{M_B}\right]^{-1} \tag{3.19}$$

where M_A and M_B are the molecular weights (g mol^{-1}) of gases A and B. The diffusion rate coefficient D_0 can be calculated from Equations 3.7 and 3.16:

$$D_0 = \frac{k_d M_c}{\nu R_u T} \tag{3.20}$$

where ν is the stoichiometric coefficient (-). If, as in this work, the sole product of the char oxidation reaction is assumed to be CO, the stoichiometric coefficient equals 0.5.

3.6 Particle size evolution

The diameter evolution of the sample particles was modeled with the following equation [55]:

$$d = d_0 \left(1 - X\right)^{\beta} \tag{3.21}$$

where d is the diameter of the particle (m) at a given time and d_0 is the particle initial diameter (m). The value 0 for the term β stands for the so-called shrinking core model. In this case the density of the particle decreases, whereas the particle external diameter remains constant. This kind of behavior is characteristic of combustion Regime I. The other extreme, Regime III, corresponds to value 1/3 for β. It describes a situation where the density of the particle remains constant and the diameter decreases, i.e. the shrinking particle model. Between the extremes of the scale, in Regime II, both the particle density and the diameter decrease. The equation was used for both cases, pyrolysis and the overall combustion process with the peat and woody biomass samples. During pyrolysis the coal particles have a tendency to swell as the erupting pyrolysis product gases expand the particle. In Publication II, with the coal sample an additional term was introduced to Equation 3.21 to describe the swelling effect. It was noted that at higher mass loss rates the swelling effect was stronger. Therefore, the swelling term was set to be dependent on the mass loss rate, as follows:

$$d = d_0 \left(\left(1 - X\right)^{\beta} + \frac{dX}{dt}\varphi \right) \tag{3.22}$$

where the coefficient φ described the magnitude of the swelling (-). However, this equation was only used in the calculations related to Publication II. The terms φ and β were fitted without restrictions in the coal pyrolysis model calculations related to Publication II. This resulted in negative values for the term β. Together with the swelling magnitude coefficient φ they described a situation where the density of the particle decreased at the same time when the diameter increased. The values are presented in Table 5 of Publication II. A better way to conduct the parameter fitting would have been to force to term β to be positive or zero.

The kinetic modeling calculations were all performed with particles consisting of 20 internal cores, all of which had the same initial volume. All the cores had different temperature histories and thus different reaction rates. Therefore,

instead of using equation 3.21, the diameter of the particle was calculated based on the combined volume change of each individual core. The volume change equation could be written similarly as Equation 3.21:

$$V_e = V_{e,0} \left(1 - X\right)^{3\beta} \tag{3.23}$$

where V_e is the volume of the element, $V_{e,0}$ is the initial volume of the element, and X is the element mass loss in dry form.

3.7 Combustion modeling calculation procedure

Before the model calculations, the initial diameter distribution of each DTR-tested fuel sample was determined. The distribution was discretized into ten size classes, each of which had the same initial volume and their own mass mean diameters. The following procedure was conducted for each particle size class. The particle was first divided into 20 co-centric cores with equal initial volumes. The variables related to the calculation were first initialized. This meant assigning the measurement based initial mass, density, velocity, temperature, etc. for the particle. The reactor was then divided into place steps. During each place step the particle temperature was first solved numerically from the energy balance Equation 3.1. The partial differential equations related to the intraparticle heat transfer were discretized by using the central differencing method. The radiation term was discretized according to [62]. The calculation procedure was a mixture of implicit and explicit methods. The internal temperature profile of the particle was solved with the help of matrix inversion. The method was not purely implicit since some of the gas and solid properties as well as the reaction rates were calculated based on the previous place step temperatures. This caused sensitivity issues and a rather small place step had to be used in some cases. The temperature profile of the particles could be solved in this way. However, in the combustion calculations solving the intraparticle O_2 concentration numerically was not sensible since the near zero concentration values made the calculation ever more time consuming. Therefore, the Thiele modulus approach was used.

For the Thiele modulus the intrinsic reactivity (Equation 3.9) was calculated using the particle average temperature. The average effectiveness factor η could then be calculated for the whole particle. The reaction rate of each core could then be calculated using their own temperature and the average effectiveness factor according to Equation 3.8. This procedure enabled taking into account the temperature gradient inside the particles, and using the Thiele modulus removed the need to solve the internal concentration gradient of O_2 numerically, which in turn simplified the solution. Nevertheless, the larger the particle, the greater becomes the error from assuming average effectiveness factor.

The reaction scheme related to the combined pyrolysis and char oxidation was selected such that in the beginning the dry, ash free part of the particle was assumed to consist entirely of material available for the oxidation reaction. Thus, the pyrolysis and char oxidation reactions competed from the unreacted solid matter. This approach meant that both processes occurred simultaneously and some of the unvolatalized compounds were oxidized as well. However, the

pyrolysis reactions were much faster in comparison to the char oxidation. Therefore, the simultaneous oxidation of char and unvolatilized compounds was very minor and the oxidation kinetic parameters actually describe almost entirely the char oxidation. With larger particles the reaction scheme will most likely cause error in the model prediction.

The aforementioned calculation process for a single particle was repeated for all the size classes generated in the particle size distribution discretization. The distribution was discretized into ten equal-sized size fractions, each of which had the same initial volume, and the model results were volume-averaged. The averaging was done according to the following equation:

$$F_{avg} = \sum_{n=1}^{10} F_n v_n \tag{3.24}$$

where F_{avg} describes the averaged variable (X, c_p, T_p, or d_p), F_n is a variable (X_n, $c_{p,n}$, $T_{p,n}$,or $d_{p,n}$) related to the n:th volume fraction, and $v_n = 0.1$ is the volume fraction.

The particle sizes used in the tests were so small that their terminal velocity was small compared to the gas velocity. Therefore, when the residence time of the particles was calculated, an assumption was made that all the size classes had the same velocity. This meant that there was no difference in the residence times between different volume fractions.

The distributed diameter model had the greatest impact on the accuracy of the particle temperature prediction. It also explained the question posed by Rodriguez in her thesis [52]. Rodriguez used a similar measurement setup for char particles and the measured particle surface temperatures seemed to remain high for much longer than the models predicted. Compared to the mono-sized single particle model the diameter distribution approach explained the measured results much better. This can be seen from Figure 3.3, where the steam-exploded wood temperature profile during combustion in 12 vol-% O_2 in N_2 is shown.

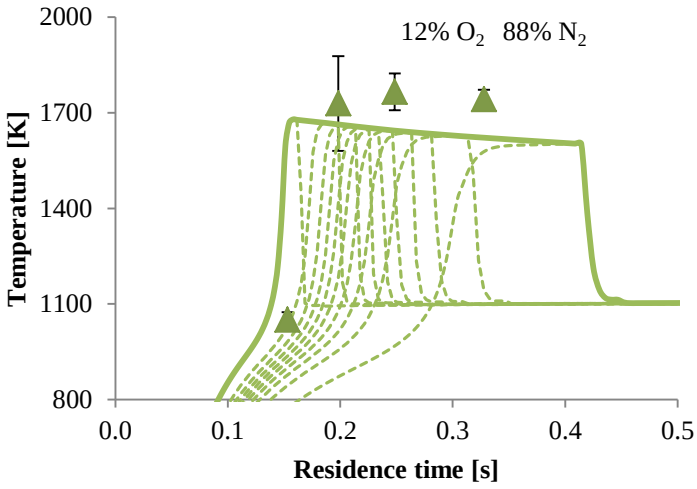

Fig. 3.3: Using discretized particle size distribution resulted in an overall apparent temperature profile where the calculated temperature remained high for longer than with a mono sized single particle model. This procedure explained better the results obtained from the two-color pyrometer measurements. The dashed lines represent single particles with different sizes and the continuous line the resulting overall temperature profile.

The importance of replacing a mono-sized particle model with the diameter distribution approach was emphasized already e.g. by [63] and [64]. In the early stages of combustion the smallest particles had reached the ignition temperature and started to heat up above the gas temperature. They would then show in the pyrometers field of view rather frequently due to their vast numbers. As the combustion process advanced the smaller particles had already been consumed by the pyrolysis and char oxidation and only the largest particles had any char to burn. Towards the end of the combustion process the frequency of the particles detected by the pyrometer decreased. This can be seen from Figure 3.3 as decreasing standard deviation.

The distributed diameter model also generated a problem related to the kinetic parameter fitting. The fitting program used a multiobjective optimization algorithm to find kinetic parameters which would give mass loss, temperature, and diameter predictions as close as possible to the measured values. The mass loss and diameter results were rather straightforward to process for the fitting algorithm. The measured mass loss was the average mass loss of all the size classes. This was also the case with the diameter. However, the pyrometer measurement results did not represent an average of all the size classes. Especially in the middle of the combustion process, some of the larger particles were not yet heated above the gas temperature and some of the smaller particles had already burned out. Therefore, the pyrometer only detected the particles which were at proper combustion stage. Because of this, the temperature profile that was used

in the kinetic parameter search was not the average profile. Instead the profile was generated based on the ten different particle profile peaks. The thick line in Figure 3.3 represents the highest attainable temperature at a given time according to the model. In the kinetic parameter search routine the mass loss results were emphasized the most, since they were directly linked to the conversion rate. The diameter and temperature results were used in the optimization also but were used more just to check how well the prediction worked.

Chapter 4

Experimental

4.1 Tested fuels

The fuels tested in this thesis were selected not only based on the interest of the industry co-operation partners of our research group, but also as they represent the most common solid fuel types used in Finland. The results were produced to serve a purpose in design and operation optimization. The selected fuels presented in the compilation part were peat, coal, raw wood, torrefied wood, and steam exploded wood. Together, these solid fuels represent the majority of alternatives that can be utilized in pulverized fuel firing. The ultimate and proximate analyzes as well as the ash fusibility of the sample fuels are presented in Table 4.1.

Table 4.1: Results of the ultimate, proximate, and ash fusibility analyzes of the fuel samples.

Analysis	Peat	Coal	Raw wood	Torrefied wood	Steam-exploded w.	Unit
Ash content (550°C)	-	-	0.3	0.3	0.5	dry wt%
Ash content (815°C)	7.1	13.7	0.3	0.2	-	dry wt%
Volatile matter	65.4	34.5	84.9	81.9	76.2	dry wt%
Sulfur	0.14	0.33	<0.02	<0.02	<0.02	dry wt%
Carbon	52.6	67.8	50.2	53.2	54.0	dry wt%
Hydrogen	5.5	4.6	6.1	6.0	5.9	dry wt%
Nitrogen	1.24	2.04	<0.2	<0.2	<0.2	dry wt%
Oxygen (calculated)	33.42	11.53	42.7	40.38	39.4	dry wt%
Chlorine	0.026	-	0.003	0.002	0.008	dry wt%
Fluorine	0.004	-	<0.001	0.001	<0.001	dry wt%
Bromine	-	-	<0.001	<0.001	<0.001	dry wt%
HHV	20.96	28.05	20.30	21.07	21.79	MJ/kg
LHV	19.76	27.06	18.97	19.77	20.51	MJ/kg

Fusibility of ash	Peat	Coal	Raw wood	Torrefied wood	Steam-exploded w.	Unit
Deformation	1210	1210	1440	1310	1250	°C
Sphere	1220	1240	>1450	-	1260	°C
Hemisphere	1250	1300	>1450	1330	1290	°C
Flow	1290	1370	>1450	1360	1300	°C

In addition to the fuel samples presented here, the effect of torrefaction on eight woody biomasses and the char oxidation process of another coal sample were also studied. The characterization of these samples is shown in Publication III and Publication IV.

The coal sample discussed in this compilation was received crushed straight from a Finnish power plant. The peat was Finnish milled peat. The rest of the sample materials were commercially available pellet products and thus the wood species were different. The raw wood was Finnish spruce and it was similar to the torrefied sample raw material, which was mostly Swedish spruce. The steam exploded sample was Southern Yellow Pine. Both the torrefied and steam-exploded wood samples were received as pellets. The raw wood was originally pelletized also, but for the DTR experiments it was received preground.

The torrefied sample was manufactured in a continuously operated reactor at 250°C. The stem wood raw material was first chipped and then torrefied. The residence time of the raw material chips in the reactor had been approximately 30 min. The mass yield of the torrefaction process had been 89.6% of the original weight. The pelletizing process had been done with a ring matrix pelletizer. The steam-exploded sample was also made from chips. The steam explosion reactor

pressure level had been 15-25 bar. The residence time had been under 20 minutes at 210°C.

4.2 Sample grinding and sieving

Before sieving, the samples were ground with a Retsch ZM200 ultra-centrifugal mill. Before the DTR tests the samples were sieved to obtain particles of similar size. The coal sample DTR measurements were conducted in two batches. The first was sieved with ring sieves sized 100-125 µm and the second later on with 112-125 µm sieves. The two peat sample was sieved with 112-125 µm sieves but there were also two different batches. The raw, torrefied and steam exploded wood sample batches were all sieved with 112-125 µm sieves. Before sieving the samples were kept in a drying oven at 105°C for 24 hours. The vibration sieving was conducted several times to narrow down the size fraction. Between the sample preparation and the measurements, the samples were kept in an exicator with silica gel to prevent moisture condensation to the samples.

The coal sample was the first one to be tested. The particles were rather spherical and homogeneous in terms of density. Moreover, an air sieve was also constructed and used to improve the vibrational sieving result. A schematic picture of the air sieve is shown in Figure 4.1.

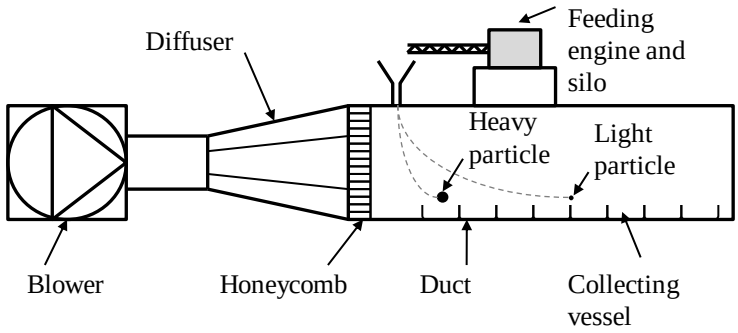

Fig. 4.1: Air sieve schematics.

The idea was that the vibrational sieved sample was fed into a laminar air stream. The stream then carried the smaller and lighter particles further down the duct and heavier larger particles were dropped closer to the feeding point. Multiple collecting vessels were placed on the bottom of the duct and a few middle ones were selected as the final sample. The sieve worked somehow with coal particles. An example of how the air sieve enhanced the size distribution with coal is given in Figure 4.2. The size distribution shows that even when 100 and 125 µm sieves were used, the volume mean diameter was greater than 125 µm. This is mostly due to the irregular and elongated shapes of the particles.

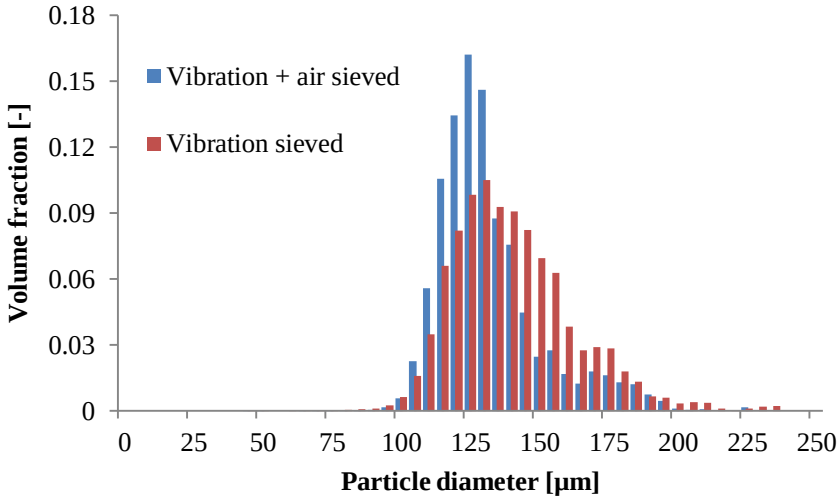

Fig. 4.2: The size distribution of the original and air sieved coal sample. The particle diameter represents a spherical equivalent diameter.

It can also be partially caused by particles being stuck to one another at the moment of imaging.

At first the air sieve was applied also to the biomass samples. However, since the biomass particles were highly elongated and somewhat irregular shaped, the benefit gained from the procedure was non-existent. The initial size distribution of the sample particles was measured with the method described later on in Section 4.7. The size distributions of the samples are shown in Figure 4.3.

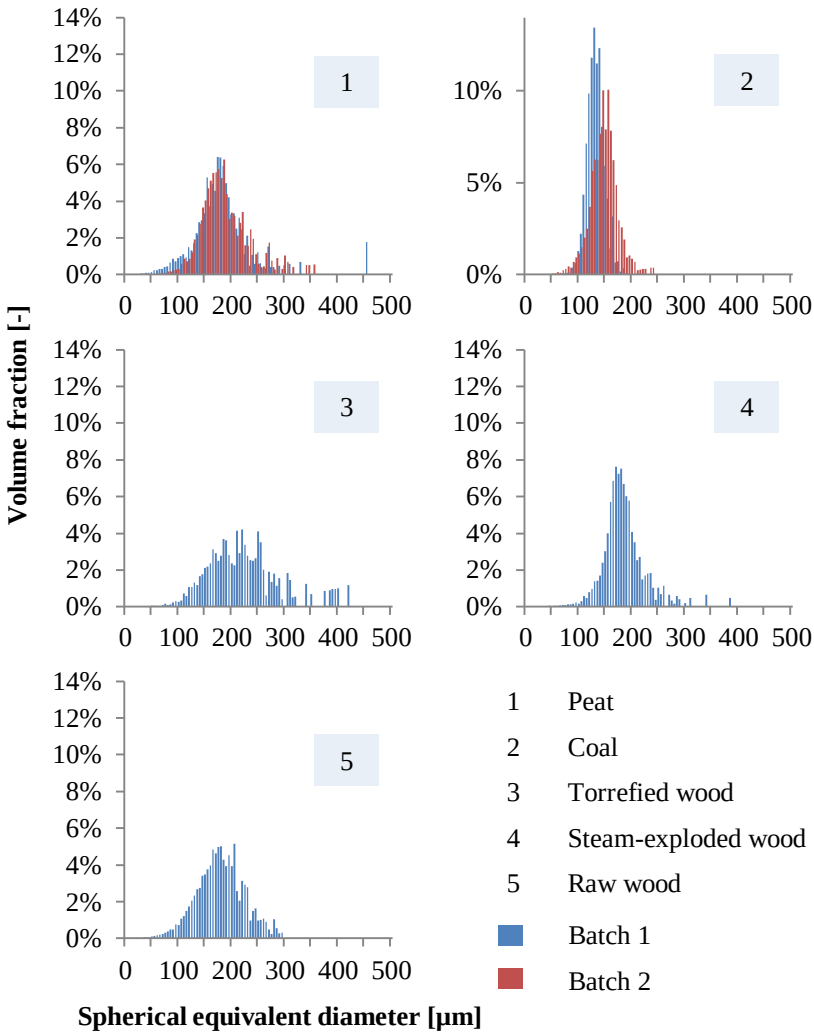

Fig. 4.3: Spherical equivalent particle diameter distribution of the samples before DTR treatment.

The distributions show that despite a really narrow size range being used in the sieving, the distribution, especially with the biomasses, was rather wide. This mostly results from the elongated particles. Batch differences with peat are non-existent and with coal the batch with the smaller volume mean diameter corresponds to the 100-125 µm sieves and the other to the 112-125 µm sieves.

4.3 Mercury porosimeter

The densities of the samples used in the DTR experiments of this thesis were measured with a Micromeritics Poresizer 9320 mercury porosimeter in the De-

partment of Civil Engineering at Tampere University of Technology. The density measurements were conducted with preground samples. The porosimeter measured the mercury intrusion into the sample up to 6 nm. The sample intrinsic density was determined based on the porosimeter data. The mercury intrusion into the five presented samples as a function of the pore diameter is shown in Figure 4.4.

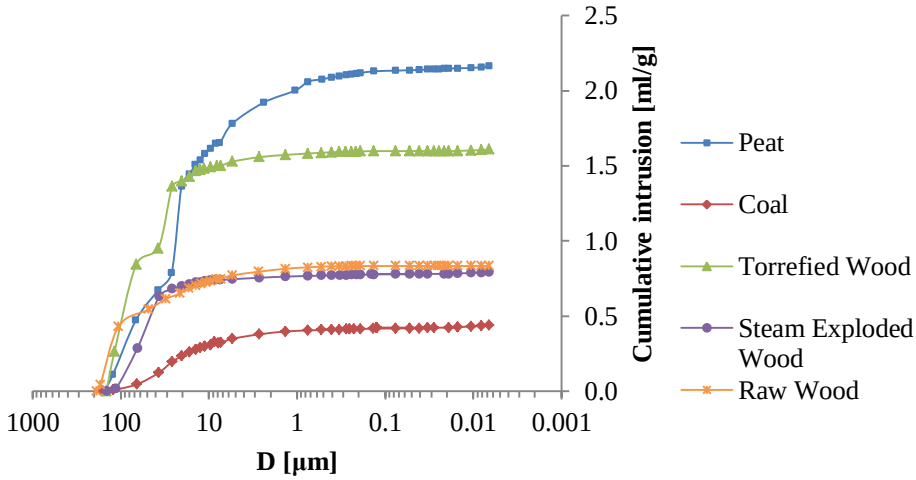

Fig. 4.4: Mercury intrusion curve of the tested samples as a function of the pore diameter.

The initial part of the intrusion curve, starting from approximately 150 µm is when the mercury fills the gaps between the ground particles. A threshold value of 26 µm was chosen to represent the point at which the mercury had filled the gaps between the particles and started to intrude inside them. The threshold value was chosen based on the slopes in Figure 4.4. The mercury porosimeter data also included the average pore diameter and the total pore surface area. These values, along with the intrinsic and apparent density values of the samples, are presented in Table 4.2.

Table 4.2: Measured intrinsic densities of the samples and evaluated apparent densities of the sample particles.

Sample	Peat	Coal 1	Raw wood	Torrefied wood	Steam exploded w.	Unit
Intrinsic density	1245	1412	1500	1208	1341	kg m^{-3}
Apparent density	625.0	1049	1055	931.0	1166	kg m^{-3}
Average pore diameter	0.4873	0.1061	3.078	0.1845	0.07129	µm
Total pore area	11.26	8.778	0.285	5.317	5.729	m^2 g^{-1}

According to general understanding in the literature, mercury porosimeter based surface area is not as accurate as, for example, gas adsorption based result. The fitted kinetic parameters will be affected by the technique used. Discussion on the surface area measurement techniques can be found, e.g. from [65]. The particle apparent density determination is further discussed in Publication II.

4.4 Drop-tube reactor

The DTR system used in the experiments of this thesis was designed and also partially constructed by the author. The design was based on the previous DTR versions used at the TUT laboratory. The previous versions are partially presented in [52], [51], and [66]. The author was also involved in using and partially designing some of the previous reactor versions. A systematic error source evaluation was conducted on the previous setups. The main improvements to previous designs were a movable feeding probe, measurement window placement, and especially the collecting system, which was developed in co-operation with Dr. Eugene Podkletnov. The impactor style liquid nitrogen quenched collecting system enabled fast and accurate mass loss measurements and, together with the optical techniques, improved the residence time determination a great deal. The collecting system made it possible to collect all the particles fed into the reactor. The DTR and the auxiliary equipment are show in Figure 4.5.

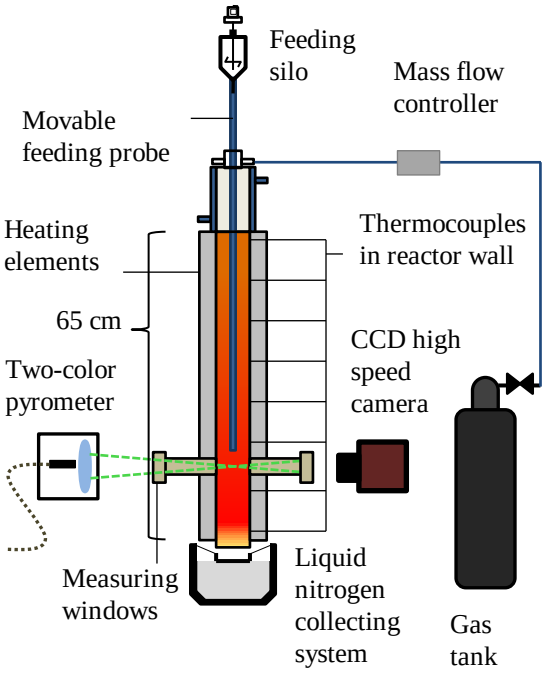

Fig. 4.5: DTR system used in the experiments of this thesis, presented in more detail in Publications II and III and V.

In previous reactor versions, the particle collecting was carried out with a suction probe. The quenching was done by inserting gaseous nitrogen into the tip of the probe. Another alternative used in previous reactor setups during pyrolysis tests was to collect the particles with a filter system without any quenching. However, with both of these systems it was noted that, especially with biomass particles, the collected particles were smouldering after collection. This made the thermal treatment exposure time imprecise in some cases.

The reactor temperature profile was measured from the wall of the reactor tube and also from within the reactor before any test runs were conducted with the current setup. Due to the reactor structure, the gas temperature had to be measured without any radiation cover. Therefore, the gas temperature was corrected in a similar way as presented in [67]. From this data, the reactor wall and gas temperature profiles were generated and used in the heat transfer models. The total volume flow of gas inside the reactor at 273.15 K was 1.585 l min^{-1}, which corresponded with the average gas velocities of 0.17 m s^{-1}, 0.20 m s^{-1}, and 0.21 m s^{-1} at furnace temperatures of 973, 1123, and 1173 K respectively. The particle feeding rate to the reactor was approximately 0.005 g per minute.

One shortcoming of the reactor system was the feeding system, which made it very hard to feed any biomass char particles into the reactor. The biomass particles had such a high amount of volatiles that the leftover char was very

brittle and crumbled when it was run through any screw feeder. It was also hard to produce biomass char particles of the size wanted. Therefore, biomass char oxidation could not be studied separately from pyrolysis. With coal, this was not a problem.

4.5 Two-color pyrometer

The two-color pyrometer used in the measurements of this thesis was assembled by M.Sc. Matti Paananen from the Physics Department of Tampere University of Technology. The falling particles' radiation was measured through the measuring windows with two narrow wavelength bands. Based on the measured wavelength ratio, the particle surface temperature could be determined. Great caution was put into the selection of these wavelengths, since the absorption of the thermal radiation from the particle to the reactor gases could have distorted the results. In addition to this, there also had to be enough thermal radiation at the selected wavelength bands for clear data. The selected wavelength bands were 1.0 and 1.6 µm for the main signals, and 1.25 µm for the reference signal.

When the temperature of the particles were calculated, the emissivity of the particles had to be evaluated. In his thesis, Joutsenoja [68] suggested a value of 0.9 for burning char particles. In this work the same value, 0.9, was used in the temperature analysis program related to the pyrometer with all the tested samples. The pyrometer setup is further discussed in detail in [69]. The use of the temperature measurement data in the kinetic parameter search routines is discussed in Publications III and V.

4.6 High-speed camera

An AVT Marlin 145-B2 camera with a 1380×1090 resolution and with black and white CCD-cell was used as the imaging tool for the particle velocity and diameter measurements. The main advantage of using imaging based particle velocity determination was that it allowed accurate residence time determination without the use of a motion equation. The samples processed with the reactor were very different in terms of particle geometries. With coal particles the Stokes law based velocity calculation might have succeeded rather well. However, in the case of the biomass samples the particle shapes were too irregular. The image analysis program calculated the average velocity from all the particle size fractions. This meant that there was no difference in the residence times between the smallest and the largest particles. The terminal velocity differences between different size classes seemed to be in some cases rather significant according to the image analysis. However, the problem was that as the particle shower inside the reactor started to spread a part of the particles were slightly out of focus in the images. For the velocity determination this was not a problem but it made it difficult to pair the velocity and diameter information. Since the particles were blurry in the images it was hard to determine the exact particle size. This undermines the accuracy of the results to some degree and the matter should be

taken into consideration in the future especially when conducting experiments with larger particles. CFD analysis of the DTR gas and particle velocities could be useful in overcoming this problem.

The camera, coupled with the DTR particle collection system, also enabled examining the particle diameter and geometry evolution as a function of the conversion process. The particles could be collected, quenched, and analyzed separately. The camera system is further discussed in Publications II, III, and V.

4.7 Particle size and geometry analysis

When performing kinetic modeling and parameter fitting based on DTR data it is essential to know the sample particles' initial mass. For this, knowing the particle size distribution and geometry are important. The approach used in this thesis was to scatter the particles on top of a light diffuser, luminate the plane from below, and image the particle projections from above. The DTR collecting system enabled particle size analysis before and after the reactor treatment. Therefore, the particle size evolution could be measured. A schematic picture of the particle geometry analysis setup is shown in Figure 4.6.

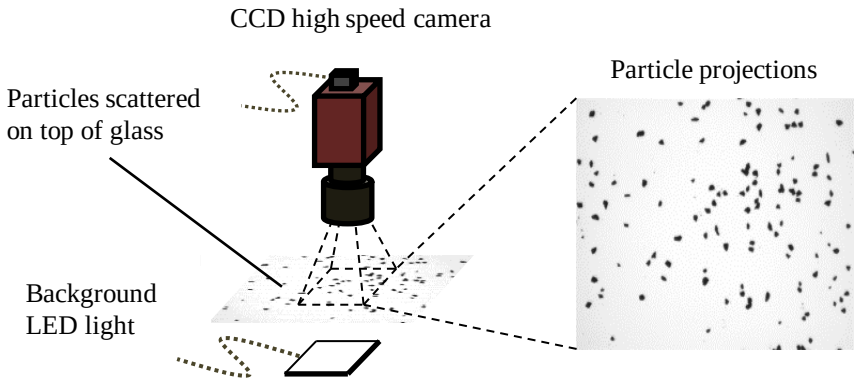

Fig. 4.6: Particle geometry analysis setup.

As mentioned in Section 4.6, another possibility to determine the particle geometry was straight from the velocity images. The velocity images were taken from within the reactor. With long residence times the particle feeding probe was far above the measuring windows and the particle stream spread slightly. Thus, some of the particles imaged with CCD camera were not in focus. Analyzing the geometry from these kinds of images might have resulted in inaccurate results. When the particles were all scattered on a single plane they were all in focus. Also, all of the particles were on one's side, showing their longest length in the images. Determining the aspect ratio of the particles was thus more straightforward. The

aspect ratio of the particles was determined based on an ellipse fit the program made for each particle. The ellipse major axis was divided by the minor one, and the result was the aspect ratio. The amount of detected particles from the images per one measurement case was between one and two thousand.

4.8 Torrefaction reactors

Two types of torrefaction reactors were used in the experiments of this thesis. The first was an electrically heated bubbling fluidized bed reactor. The other was a slow heating rate oven with an inner gas tight container. The fluidized bed reactor was used in the experiments related to Publication I. A schematic picture of the reactor is shown in Figure 4.7.

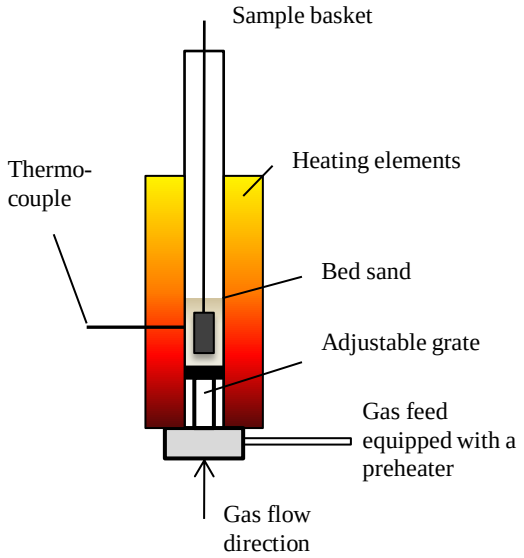

Fig. 4.7: Electrically heated bubbling fluidized bed reactor used in fast torrefaction.

The bed material used was quartz sand with a particle size of 500-600 μm. The operation of this reactor is further discussed in [70].

The second reactor is shown in Figure 4.8.

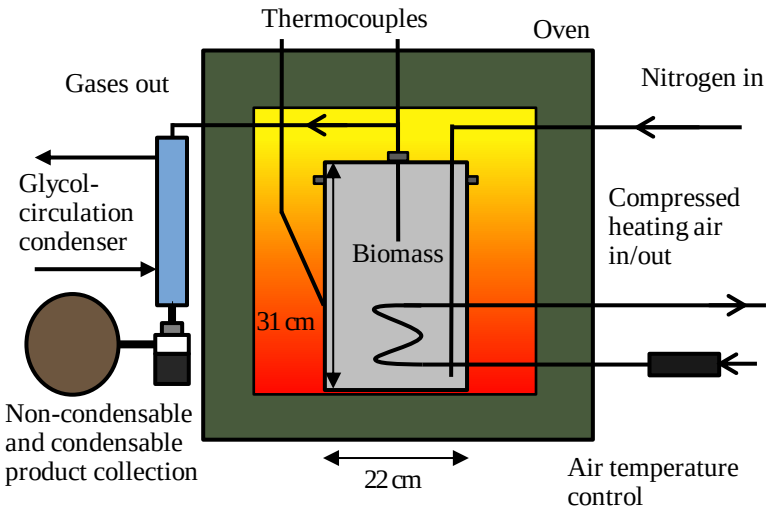

Fig. 4.8: Slow heating rate oven with an inner gas tight container.

The slow heating rate reactor was used in the experiments related to Publication IV. The torrefied wood sample that was used in the DTR tests was not produced with either of these reactors. The tested pellet products were commercial products and they were received for testing already heat treated.

4.9 Fine grinding energy measurement

The main instrument used in the fine grinding energy requirement experiments for the sample pellets was the same Retsch ZM200 ultra-centrifugal mill that was also used for the DTR sample crushing. The mill was coupled with a Christ Elektronik CLM1000PP energy consumption meter for monitoring the power draw. The measurement setup was used in two separate cases. The first case was to determine how torrefaction affected the fine grinding energy requirement of pine cubes. The second case was to examine the grinding energy requirement and end product quality of commercial woody biomass pellets. The experiments are further discussed in [70] and Publications I and V.

Chapter 5

Results and discussion

5.1 Physical property characterization

5.1.1 Effect of torrefaction on fine grinding energy

The study related to the collaboration work with Dr. Lauri Kokko considered the effect of torrefaction on the fine grinding energy requirement of woody biomass. The study is presented in more detail in Publication I. Figure 5.1 shows how, regardless of the torrefaction treatment temperature, the fine grinding energy requirement decreases as a function of the dry mass loss. This observation is also presented by Repellin [4]. The sample used in the fine grinding tests was produced with the reactor presented in Section 4.8. The temperatures used in the production procedure are presented in Figure 5.1.

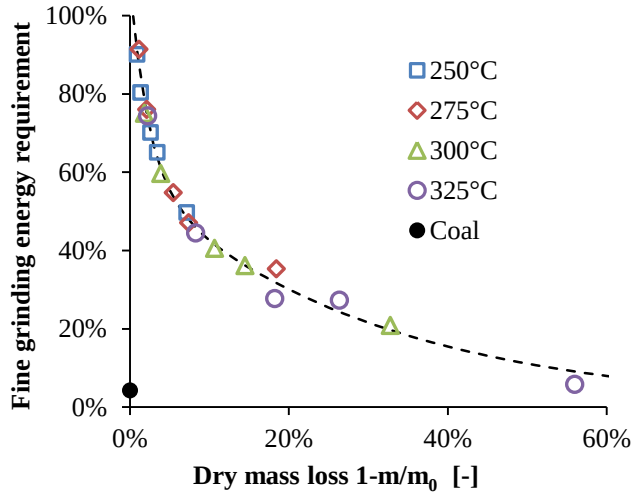

or

Fig. 5.1: Fine grinding energy requirement for wood cubes torrefied at different temperatures as a function of dry mass loss.

Figure 5.1 also shows the relative energy requirement for fine grinding coal particles compared to raw wood cubes. Along with the result presented in Publication IV that torrefaction decreases feedstock chlorine content, it would appear that mild thermal pretreatment can improve the feedstock quality in terms of reducing the fine grinding energy requirement.

5.1.2 Biomass pellet fine grinding energy and resulting particle geometry

An ever more important aspect of fuel characterization is determining the particle geometry that results from a grinding process. The fine grinding energy of the three biomass pellets, raw, torrefied, and steam-exploded, was compared by using the setup described in Section 4.9. The resulting particle size distribution was also analyzed with the setup shown in Section 4.7. The results are shown in Figure 5.2. The step changes in the cumulative volume curve towards the end are caused by single large particles detected by the analysis program.

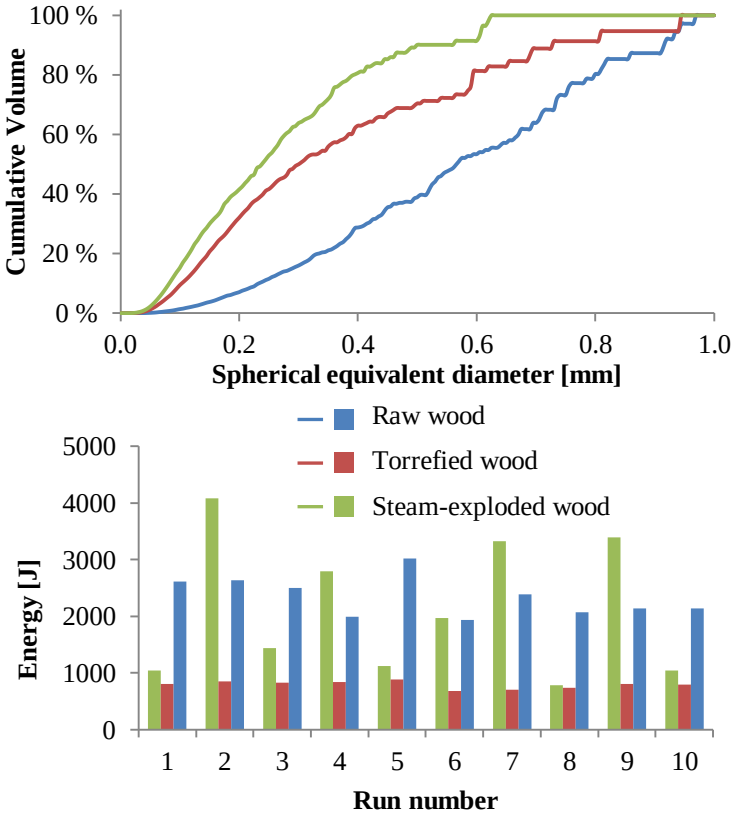

Fig. 5.2: Spherical equivalent diameter number fractions of particles resulting from the grinding process, and required pellet fine grinding energies for raw, torrefied, and steam-exploded pellets.

It would appear that the torrefied pellet had by far the smallest fine grinding energy requirement. There also seemed to be a lot of fluctuation in the steam-exploded sample results. However, because the pelletizing process and the possible additives can distort the results, the grinding energy tests presented here might be a poor indicator of how the thermal treatment technology affects the structural strength of the biomass itself. A more interesting fact is how the particle size and geometry of the heat treated samples appeared compared to the raw sample. The spherical equivalent diameter comparison of the ground samples showed that grinding the torrefied and steam-exploded pellets resulted in smaller particles. From the two types of heat treated samples the steam-exploded sample particles were by far the most spherical. The average aspect ratios of the samples were 2.23, 2.20, and 1.69 respectfully for raw, torrefied, and steam-exploded samples. This information can be an important factor when determining the trajectories of the particles in industrial furnaces.

5.2 Drop-tube reactor test results and reactivity characterization

The fuel reactivity characterization was conducted to the five samples presented in Section 4.1. Mass loss, particle surface temperature during combustion, and particle geometry evolution were determined from the DTR experiments. Based on this information the fuel reactivity parameters could be determined with the multiobjective optimization routine described in Section 3.7. In addition, the sample reactivity could be compared. The DTR setup is shown in Section 4.4.

5.2.1 Mass loss

The mass loss results from the DTR tests used in the reactivity parameter fitting procedure are presented in Figures 5.3, 5.4, and 5.5. The model fits are also presented to show how well the calculation results could be optimized. The mass loss of the samples is shown in dry ash-free (DAF) form. As all the fed particles could be collected, the mass loss could be calculated based on the fed and collected sample amounts. The residence time of samples in the DTR was determined based on the high-speed camera images. Discussion about the particle motion and velocity calculation can be found in Section 3.3 and Publication II. In the figures showing the sample mass loss as a function of residence time it is noteworthy that the time scale with the coal sample is different compared to the others. This was because the coal sample had a rather slow conversion rate in the tested environment and the final tests were conducted with longer reactor heating length than that needed with the other samples.

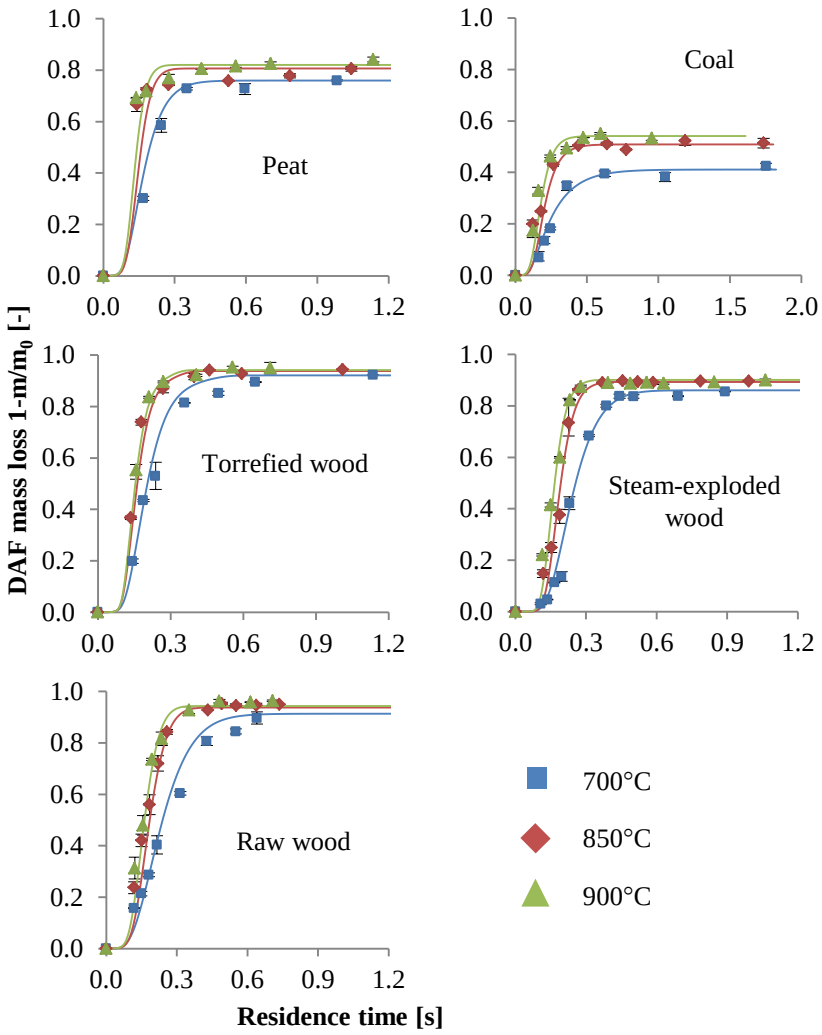

Fig. 5.3: DAF mass loss during pyrolysis as function of residence time in the DTR. The dots represent the measured values and the lines the model fits.

The pyrolysis mass loss tests indicate well how the volatile matter amount was different between different types of samples. The coal sample DAF volatile matter amount was a little over 50 %, whereas in the case of the biomasses the amount was even above 90 %. A direct comparison in terms of mass loss versus time between the samples is not entirely straightforward nor sensible. Due to the different apparent densities the samples had different falling velocities inside the reactor. Moreover, since the reactor temperature was dependent on the place in the reactor, especially right after the probe tip when the temperature started to rise, the samples also developed different external temperature histories. There-

fore, in order to actually compare the reactivities of different samples, kinetic modeling had to be applied.

The char oxidation tests were conducted both in O_2/N_2 and O_2/CO_2 atmospheres. The high amount of volatiles in the biomass samples made it harder to distinguish between the different O_2 concentration cases than with the coal and peat samples. The reactivity parameters were determined based on the O_2/N_2 results. The model results in Figure 5.5 were calculated with the same parameters. The gas property differences were taken into account in the calculations. In other words, the differences between the measured and the calculated results in Figure 5.5 should result only from possible changes in the oxidation reaction kinetics or from the CO_2 gasification reaction. The pyrolysis stage in both atmosphere cases was calculated according to the parameters determined based on the pure N_2 experiments. If CO_2 in the atmosphere had some effect on the pyrolysis reaction kinetics, it was not taken into consideration.

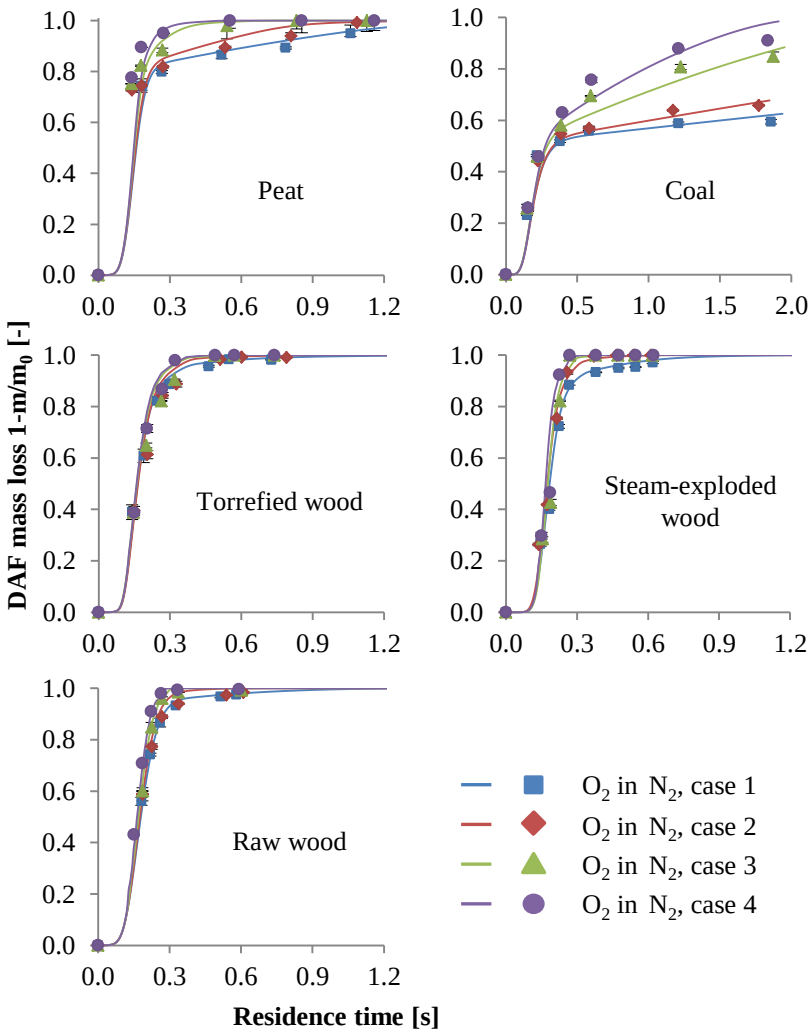

Fig. 5.4: DAF mass loss in the DTR during combustion in O_2/N_2 atmosphere as a function of residence time. For the peat and coal sample the O_2 concentrations in cases 1-4 were respectively 2, 3, 6, and 8 vol-%. For the raw, torrefied and steam-exploded wood samples the corresponding concentrations were respectively 3, 6, 12, and 21 vol-%.

Conducting the char combustion tests separately from the pyrolyis stage would have been the best alternative. However, as explained previously this was not possible with the setup used due to the brittle nature of biomass char particles. The model fits in Figure 5.4 seem to be rather accurate. Nevertheless, the high amount of volatiles in the biomass samples definitely reduced the char oxidation parameter accuracy.

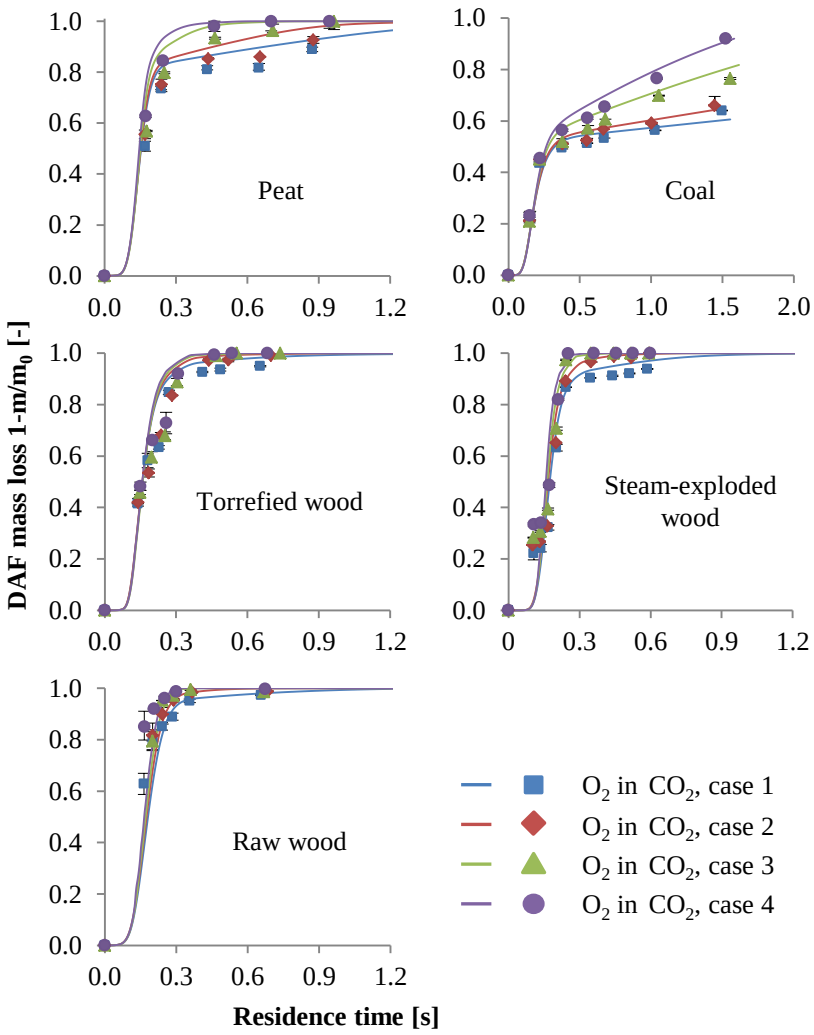

Fig. 5.5: DAF mass loss in the DTR during combustion in O_2/CO_2 atmosphere as a function of residence time. For the peat and coal sample the O_2 concentrations in cases 1-4 were respectively 2, 3, 6, and 8 vol-%. For the raw, torrefied and steam-exploded wood samples the corresponding concentrations were respectively 3, 6, 12, and 21 vol-%.

Since some differences between the modeled and measured results can be seen in Figure 5.5, especially with the peat and torrefied wood samples, it could be speculated that the high CO_2 concentration in the boundary layer might have interfered with the reaction between O_2 and solid carbon. This behavior was speculated on also in Publication III, where the mentioned phenomenon was studied with two coal chars. However, in both cases the evidence is far too inconclusive to make any definitive claims this competition between oxidation and

gasification exists. Tests are needed especially with larger particles to confirm this phenomenon and to determine how meaningful it could be, e.g. in CFD calculations. Larger particles would show more separation in the results and any differences would be more visible. Another, more likely, possibility for the difference between the measured and modeled results in the O_2/CO_2 environment would be the CO_2 gasification. The gasification reaction, if significant, would also affect the particle surface temperature. With the coal, peat, and torrefied wood samples this behavior is somewhat visible when comparing Figures 5.4 and 5.12 with Figures 5.5 and 5.13. The question this comparison between the O_2/N_2 and O_2/CO_2 cases tries to answer is whether the reactivity parameters determined in N_2/O_2 atmosphere can be used also in CO_2/O_2 environment without taking into account any possible interference between the gasification and oxidation and without taking into account the gasification reaction. Based on the mass loss measurement and model results this issue seems to be slightly fuel sensitive. Especially with the steam-exploded wood, and with the raw wood also, the difference between the atmosphere cases is rather small.

5.2.2 Particle geometry evolution

The particle geometry evolution was determined with the setup shown in Section 4.7. During pyrolysis, the mass mean diameter of the sample particles was noted to decrease with the peat and biomass samples. With coal the particles swelled and the final diameter after the pyrolysis process was somewhat the same or even a little greater than the initial diameter. The standard diameter evolution Equation 3.21 was able to follow the measured trend rather well with peat and biomass. With coal the result was not as good. This can be seen from Figure 5.6. The dots represent the measured and volume mean averaged values and the lines the model fits averaged from all the ten size classes. In general, the diameter model fits were a little less accurate compared to the mass loss. This was most likely because more emphasis was given to the mass loss in the optimization procedure. Also, a major shortcoming of the particle imaging system was that a part of the smallest particle might have burned out totally and only the larger particles showed on the images. Because of this the fits were allowed to undershoot the measured values a little.

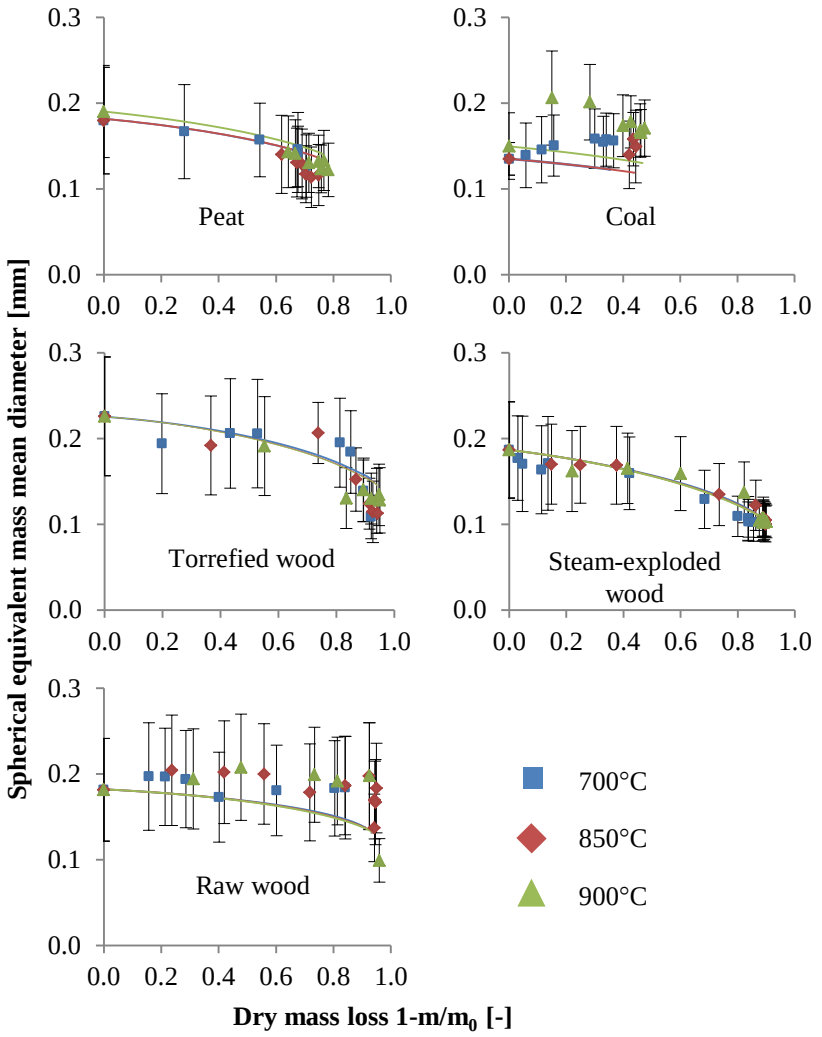

Fig. 5.6: Spherical equivalent mass mean diameter evolution during pyrolysis in the DTR as a function of dry mass loss. The dots represent the measured values and the lines the model fits.

An alternative solution for modeling the diameter evolution for coal pyrolysis is presented in Publication II. It takes into account the swelling during pyrolysis. However, since no notable swelling was observed during combined pyrolysis and char oxidation even with the coal sample, the method was not used in the model calculations presented here.

The O_2/CO_2 atmosphere case presented in Figure 5.8 showed no notable difference compared to the O_2/N_2 case.

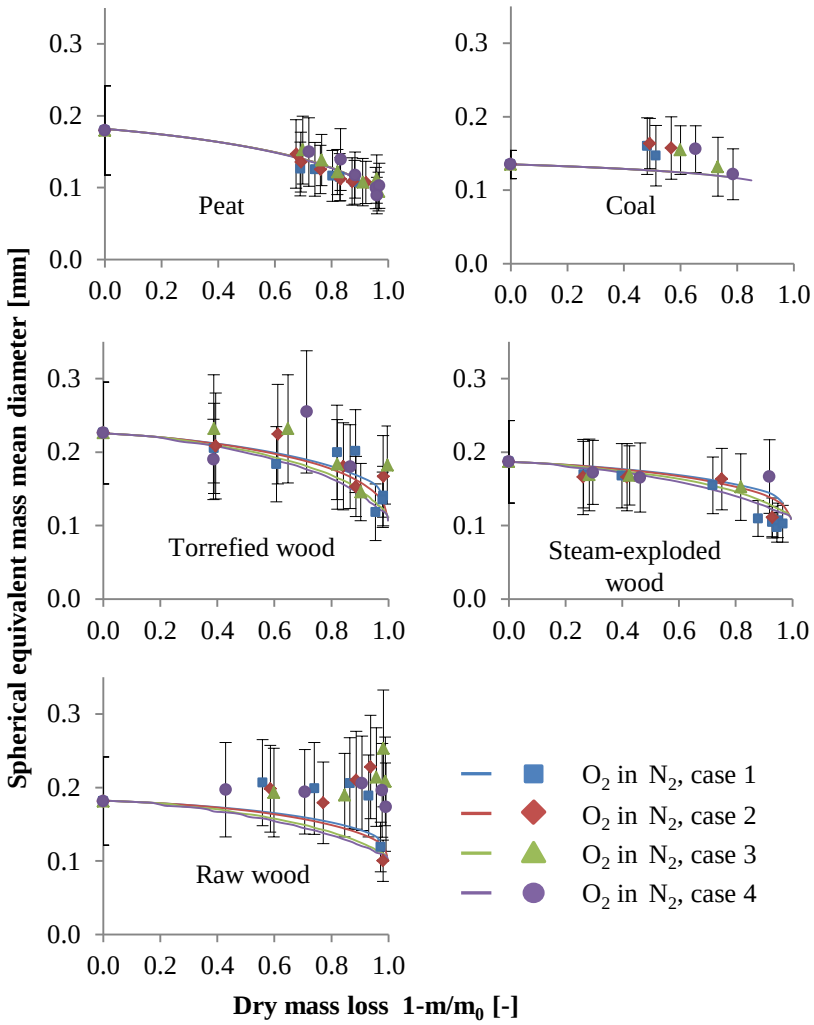

Fig. 5.7: Spherical equivalent mass mean diameter evolution in the DTR during combustion in O_2/N_2 atmosphere as a function of dry mass loss. For the peat and coal sample the O_2 concentrations in cases 1-4 were respectively 2, 3, 6, and 8 vol-%. For the raw, torrefied and steam-exploded wood samples the corresponding concentrations were respectively 3, 6, 12, and 21 vol-%.

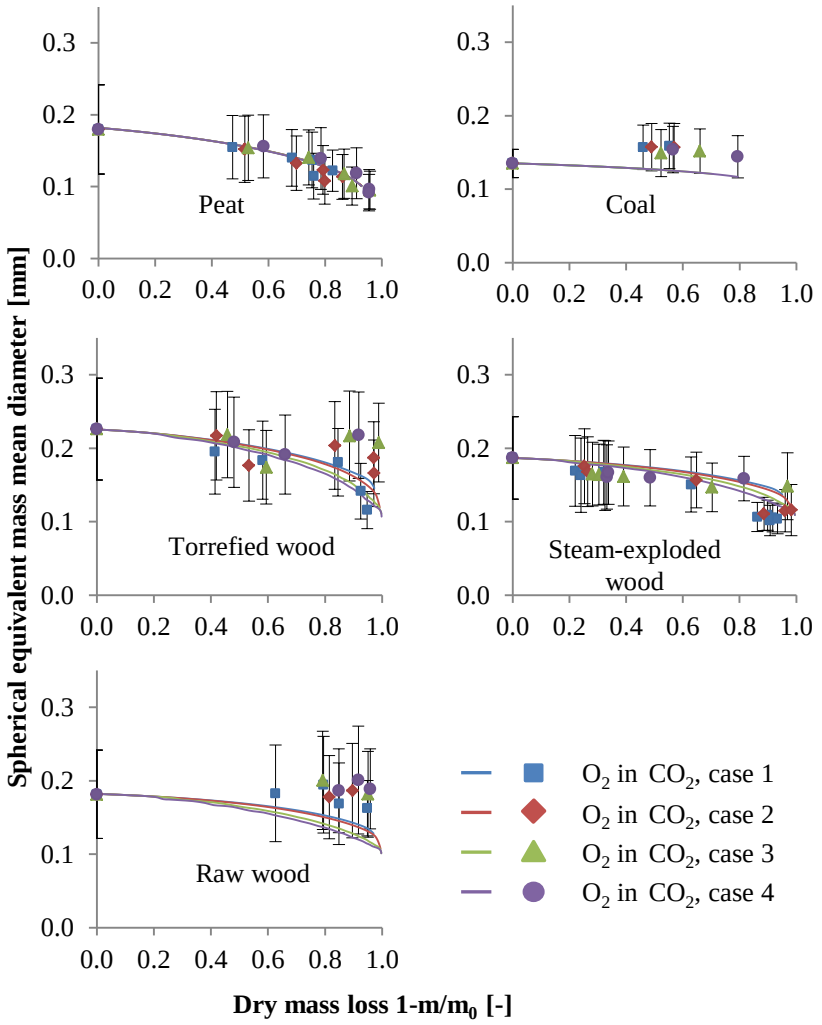

Fig. 5.8: Spherical equivalent mass mean diameter evolution in the DTR during combustion in O_2/CO_2 atmosphere as a function of dry mass loss. For the peat and coal sample the O_2 concentrations in cases 1-4 were respectively 2, 3, 6, and 8 vol-%. For the raw, torrefied and steam-exploded wood samples the corresponding concentrations were respectively 3, 6, 12, and 21 vol-%.

The average aspect ratios of the imaged particles are shown in Figures 5.9 and 5.10 as a function of the dry mass loss. Determining the particle aspect ratios was a rather robust procedure and the results are at best only approximate. The values are shown separately for pyrolysis and for combined pyrolysis and char oxidation.

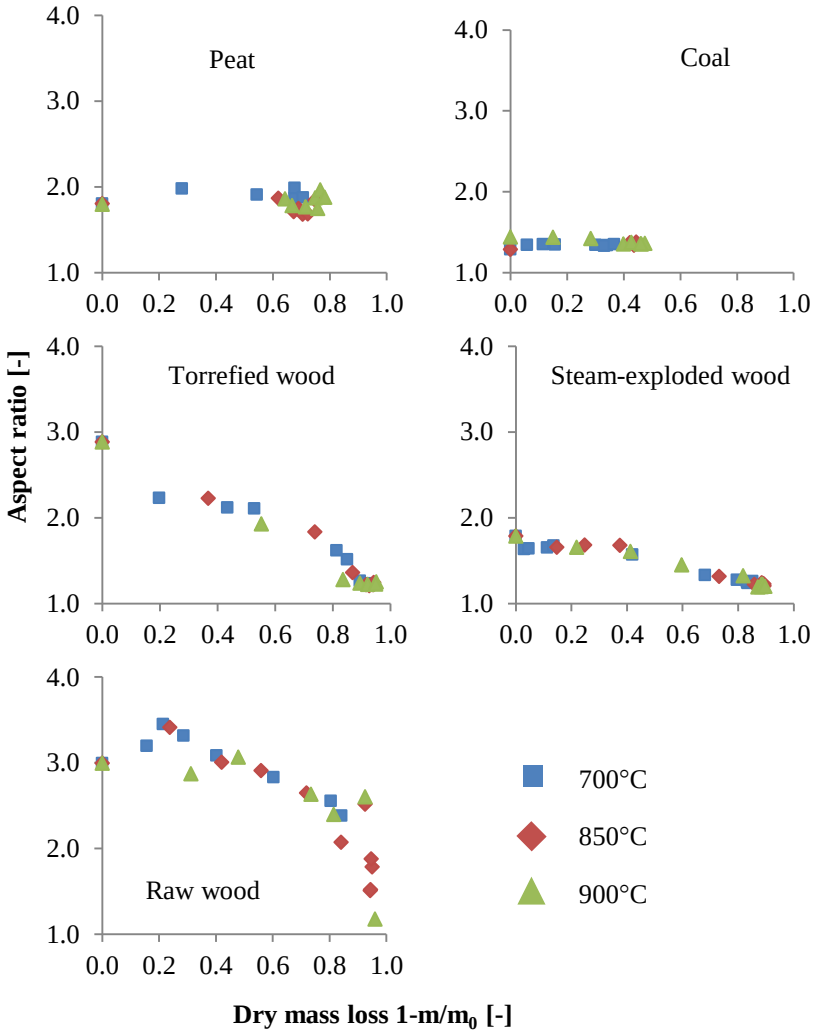

Fig. 5.9: Particle aspect ratio evolution as a function of dry mass loss during pyrolysis in the DTR.

The initial sample particle average aspect ratios were 1.80, 1.29, 2.88, 1.78, and 2.99 respectively for the peat, coal, torrefied wood, steam-exploded wood, and raw wood samples.

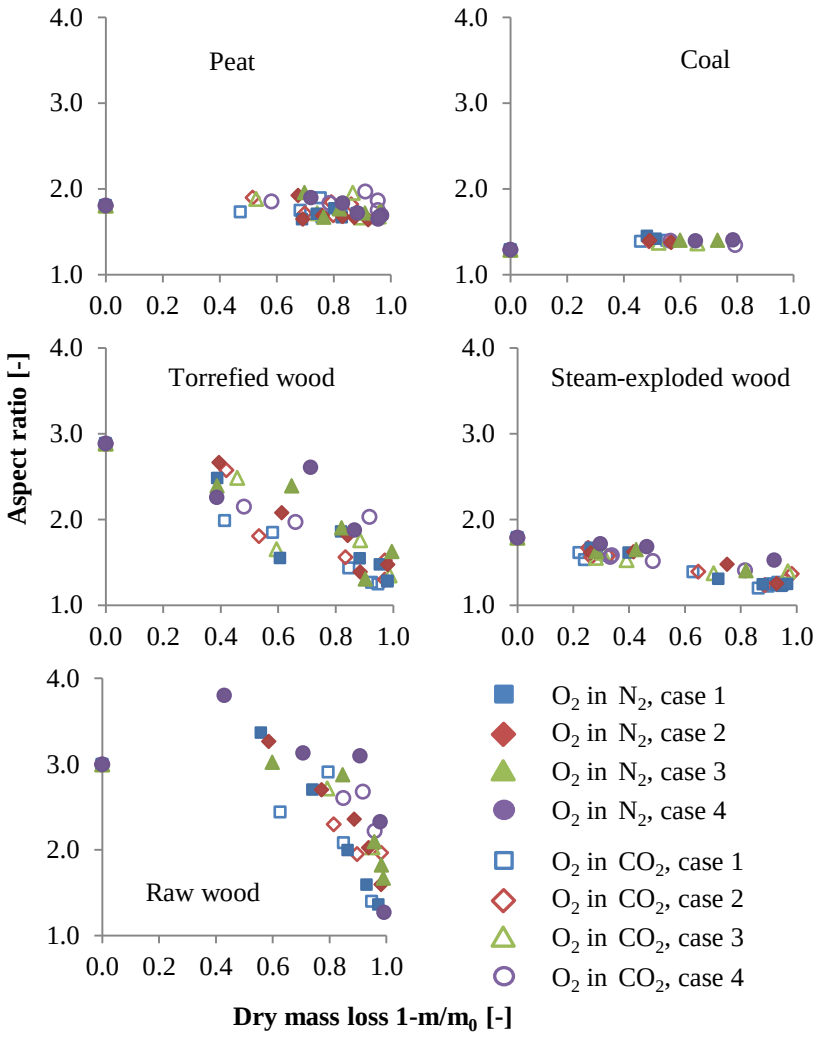

Fig. 5.10: Particle aspect ratio evolution as a function of dry mass loss in the DTR during combustion in O_2/CO_2 and O_2/N_2 atmospheres. For the peat and coal sample the O_2 concentrations in cases 1-4 were respectively 2, 3, 6, and 8 vol-%. For the raw, torrefied and steam-exploded wood samples the corresponding concentrations were respectively 3, 6, 12, and 21 vol-%. The dots represent the measured values and the lines the model fits.

Figures 5.9 and 5.10 indicate that there was only a small difference in the aspect ratio evolution between pyrolysis and the overall combustion process. The peat and coal aspect ratios remained rather similar throughout the processes, whereas the biomass values clearly decreased. The reason for this is most likely the chemical structure of the solid fuel samples. The issue is further discussed in Publication II. It seemed that from the three biomass samples the steam-exploded

particles were closest to coal in terms of geometry evolution. This information could have significance when calculating particle heat transfer and trajectories in furnaces. Lu et. al. [71] concluded that using spherical mathematical approximations for aspherical shapes poorly represent the actual combustion behavior when particle size exceeds 200–300 µm. Momeni et. al. [72] studied the effect of particle aspect ratios on the conversion time. They concluded in their article that among biomass particles with equal volume, spherical particles have the longest conversion times. However, the tests were conducted with particles approximately ten times larger than in this study.

5.2.3 Particle surface temperature

The particle surface temperature was measured with the two-color pyrometer shown in Section 4.5. Since no separate char oxidation tests could be conducted with the biomass samples on a large scale, the effect of volatiles combustion on the particle surface temperatures was studied with the steam-exploded wood particles. Some of the original sample was prepyrolyzed in the DTR in pure N_2 at 1123 K. These char particles were again fed to the DTR and the pyrometer was used to measure the surface temperature of the char particles at 12 vol-% of O_2 in N_2. The results were then compared to the untreated sample tests. The difference in the measured particle surface temperatures is presented in Figure 5.11.

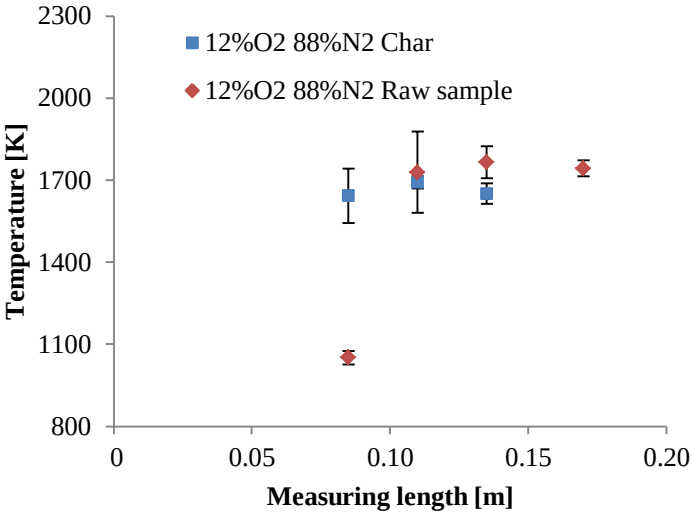

Fig. 5.11: Effect of volatiles combustion on the steam-exploded sample particle surface temperatures in the DTR.

Figure 5.11 shows that the temperature difference between the prepyrolyzed char and the raw sample was rather small. The char oxidation process was delayed due to pyrolysis, but the volatiles combustion did not drastically change the

measured particle maximum temperature. Therefore, it was concluded that the radiative heat transfer from the combusting volatile gas film towards the particle was minor. It also meant that the particle surface temperature measurement results from the combined pyrolysis and char oxidation tests could be used in the char oxidation kinetic parameter search without significant error. Riaza et. al. [73] were able to separately measure the volatile matter and char temperatures. With various coals the difference between the combustion temperatures of the particle char and the surrounding volatile matter flame was approximately 100-200 K. It might be so that in this work the two-color pyrometer actually measured partially volatile matter flame. This would cause some error in the results and would be a matter to look into in future studies.

The temperature profiles shown in Figures 5.12 and 5.13 were calculated based on the procedure shown in Figure 3.3. The model temperature fit came rather close to the measured one. The distributed diameter model seemed to explain well why the temperature profile remained high for such a long time.

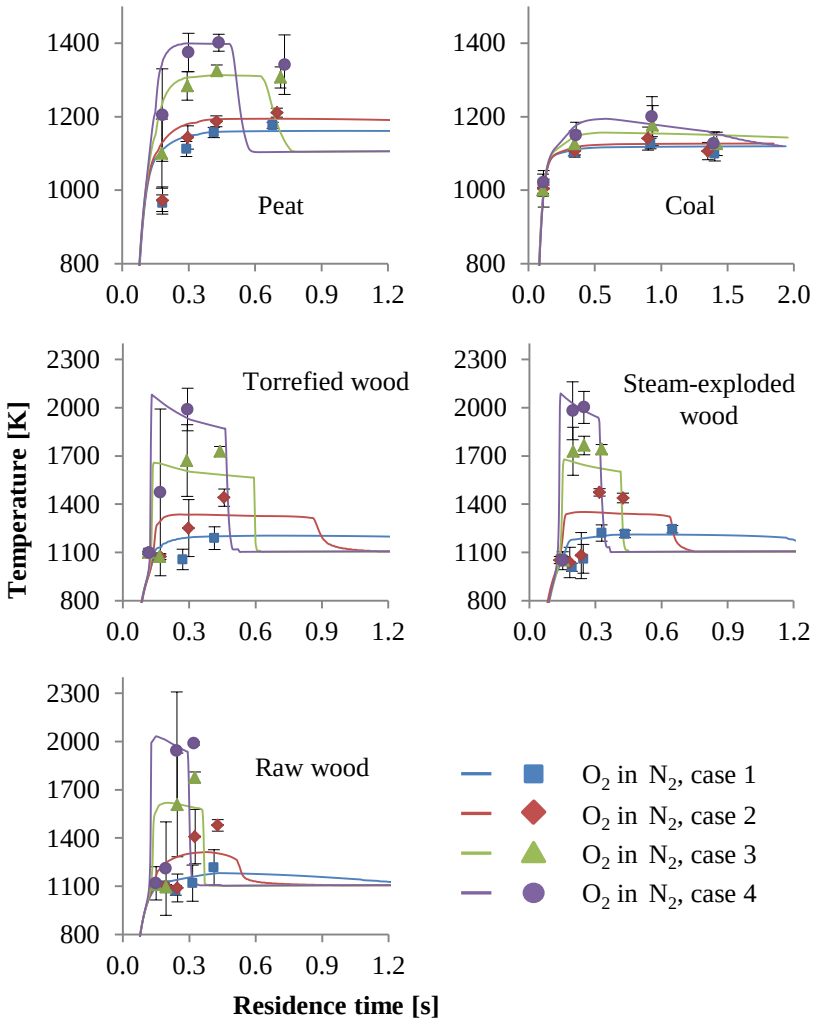

Fig. 5.12: Particle surface temperature as a function of residence time in the DTR during combustion in O_2/N_2 atmosphere. For the peat and coal sample the O_2 concentrations in cases 1-4 were respectively 2, 3, 6, and 8 vol-%. For the raw, torrefied and steam-exploded wood samples the corresponding concentrations were respectively 3, 6, 12, and 21 vol-%.

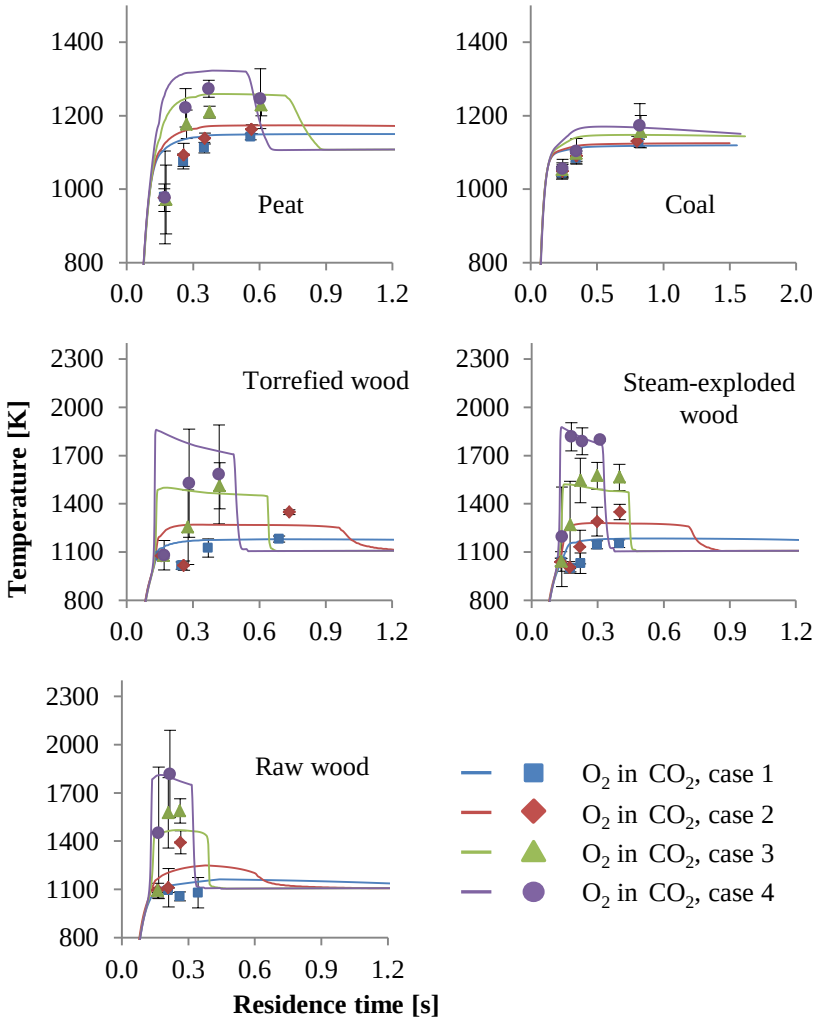

Fig. 5.13: Particle surface temperature as a function of residence time in the DTR during combustion in O_2/CO_2 atmosphere. For the peat and coal sample the O_2 concentrations in cases 1-4 were respectively 2, 3, 6, and 8 vol-%. For the raw, torrefied and steam-exploded wood samples the corresponding concentrations were respectively 3, 6, 12, and 21 vol-%.

Figure 5.13 indicates that replacing N_2 with CO_2 from the atmosphere reduces the measured particle surface temperatures. In Publication III, as the matter was examined closer with two coal chars, an interaction between the char oxidation and the CO_2 gasification reactions was speculated. The hypothesis was that the differences in the measured particle surface temperatures resulted not only from the gas property differences between N_2 and CO_2 or the gasification reaction, but also partly from the mentioned interaction. However, based on Fig-

ures 5.12 and 5.13, there seems to be no conclusive evidence that adding CO_2 to the combustion atmosphere would drastically change the reaction kinetics related to the char oxidation. This means that if the reactivity parameters are determined based on O_2/N_2 measurements, they can also be used to some extent in cases modeling O_2/CO_2 atmospheres. On the other hand, no clear sign of the CO_2 gasification reaction can be seen with all fuels. Especially the raw and steam-exploded wood sample measured and modeled results seemed to match rather well both in terms of mass loss and particle surface temperature. If the gasification reaction were significant, the measured particle surface temperature would have been lower due to the endothermic nature of the reaction. This, in turn, would have meant a greater difference between the measured values and the model prediction. With peat, coal, and torrefied wood a slight difference can be seen between the measured and modeled results. This difference most likely originates from the gasification reaction.

TGA based tests suggest that in some cases the CO_2 gasification reaction would account for well over 20% of the solid fuel conversion at high temperatures [74]. A comparison of the oxidation and CO_2 gasification reaction rates based on low heating rate measurements can be found in [75]. This article also suggests that the gasification reaction is notable compared to oxidation. However, there is not much data reported on the ratio of the gasification and oxidation reactions under high heating rates. In the experiments of this work, the gasification reaction did not seem to have as strong an effect as the low heating rate studies would suggest. More investigation is needed to confirm this.

5.2.4 Fitted parameters

The kinetic parameters related to the pyrolysis and oxidation models determined in this work are presented in Table 5.1.

Table 5.1: Fitted Kobayashi pyrolysis model and char oxidation model kinetic parameters.

Pyrolysis						
Parameter	Peat	Coal	Raw wood	Torrefied wood	Steam exploded w.	Unit
A_1	202.2	92.54	64.60	92.96	72.65	s^{-1}
$E_{a,1}$	23,790	22,940	20,440	23,600	27,320	J mol^{-1}
A_2	583,900	608,400	666,700	615,700	651,700	s^{-1}
$E_{a,2}$	88,620	104,600	89,410	74,190	83,300	J mol^{-1}
α_1	0.6588	0.3334	0.8406	0.6804	0.4280	-
α_2	0.9926	0.8738	0.9997	0.9996	0.9787	-
β	0.2118	0.2212	0.1173	0.1580	0.2561	-

Char oxidation						
Parameter	Peat	Coal	Raw wood	Torrefied wood	Steam exploded w.	Unit
A	4.413×10^{-4}	3.817×10^{-4}	19.10	4.284	12.28	s m^{-1}
E_a	95,740	110,700	160,900	166,500	169,400	J mol^{-1}
β	0.2238	0.09273	0.1012	0.1202	0.1019	-

In this thesis, models that are commonly admitted by CFD codes were selected. The kinetic parameters can only be used in conjunction with both the combustion and pyrolysis models employed to derive them and the reaction scheme to link the reactions. Moreover, while the reaction scheme enabled overlapping pyrolysis and char oxidation, the oxidation parameters may not be accurate if used separately from the pyrolysis model.

5.2.5 Sample reactivity comparison

As mentioned previously, a direct comparison of the DTR results between samples is not sensible. The samples have different external temperature histories due to different falling velocities. To be able to compare the sample reactivities, the determined kinetic parameters were used to model the pyrolysis and char oxidation processes of the samples in the same environment. The results in Figure 5.14 were calculated with particles which had 200 µm spherical equivalent diameters at 1123 K reactor wall and gas temperature. The results were calculated both in O_2/N_2 and O_2/CO_2 atmospheres. The differences in the results derive solely from the gas property differences between N_2 and CO_2.

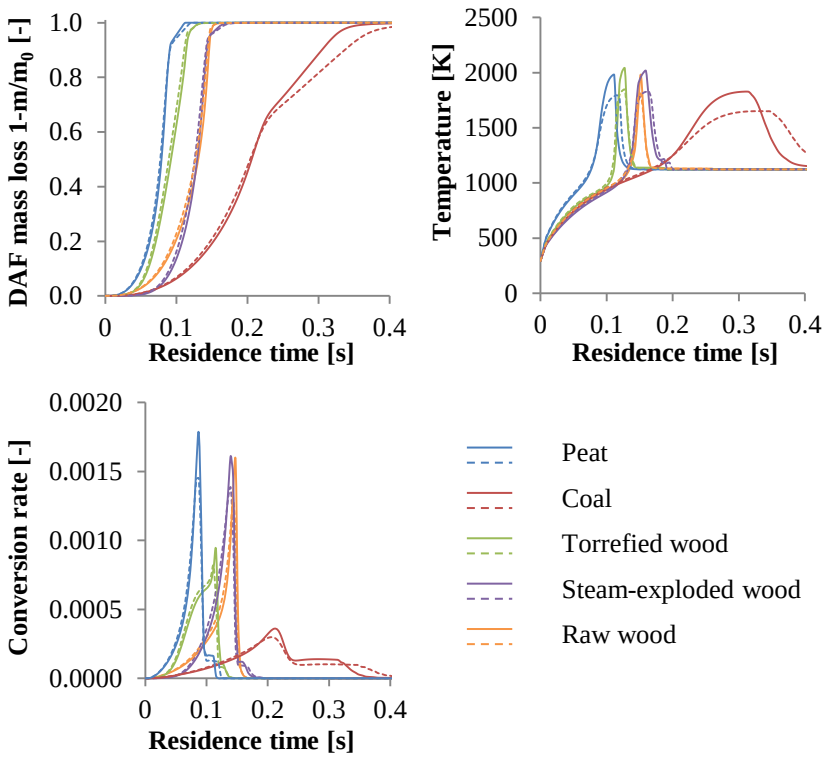

Fig. 5.14: Mass loss, particle surface temperature, and conversion rate of 200 µm -sized samples. The diameter represents the spherical equivalent diameter, and thus the particles have equal initial volumes. The results were calculated with identical external temperature histories. Both the gas and the radiating surface temperatures were set to 1123 K. The O_2 concentration was set to 21% in both N_2 and CO_2. The continuous and dashed lines represent the N_2 and CO_2 cases, respectively.

The fastest overall conversion was noted with peat and the slowest with the coal sample. The difference between the biomass samples was rather small compared to the one between coal and any of the other samples.

One of the most important result of this thesis can be seen in Figure 5.15. It presents how much time a certain sized fuel particle requires to reach 99.8% DAF conversion. The calculation procedure was conducted with spherical particles as all the other model calculations. However, the peat and the biomass sample particles were in reality all rather elongated. The initial aspect ratio of the particles was also known. Therefore, the peat and biomass particle geometry was modified to that of a cylinder with an equal volume to that of the spherical particle. The cylinder dimensions were determined based on the initial aspect ratios. The x-axis in Figure 5.15 corresponds to the cylindrical particle minimum dimension. In other words, it represents the sieving size the particle would still fit through.

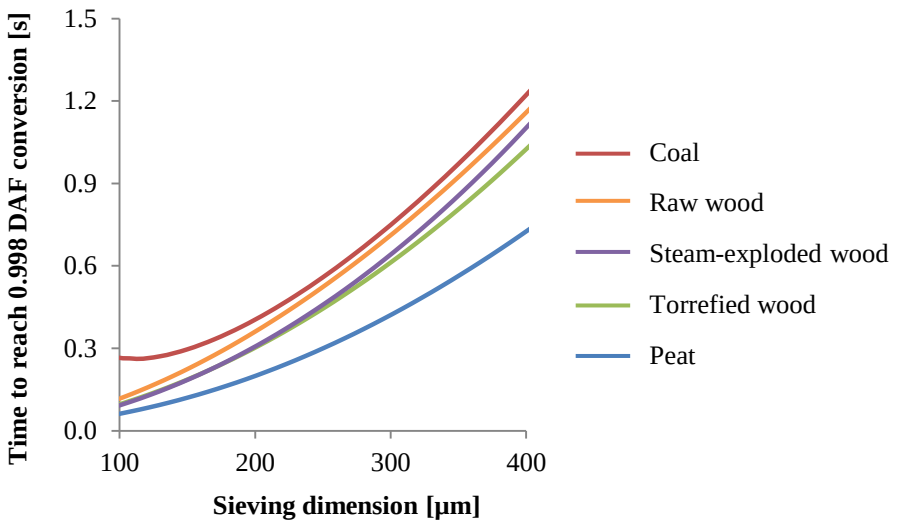

Fig. 5.15: The time a certain sized particle takes to reach 0.998 DAF conversion at 1123 K environment temperature and 21% of O_2 in N_2. The sieving dimension describes the smallest dimension a spherical or a cylindrical particle would fit through.

The coal sample had the lowest amount of volatiles from all the tested samples. This resulted in slower conversion times compared to the peat and biomass samples, as the char combustion process lasted longer. Peat, on the other hand, seemed to have the fastest devolatilization rate. This could be due to its low apparent density. The raw, torrefied, and steam-exploded biomass samples seemed to behave in a similar manner to one another. It would appear that the greatest difference between these three samples was not in the reactivity, but rather in the particle geometry evolution. The torrefied sample had a slightly faster conversion time, which could have been due to higher reactivity or just better heat transfer between the particles and the reactor environment resulting from the elongated shape of the particles. This, however, is mere speculation and based on the measured data there is no way to prove this.

Chapter 6

Summary and conclusions

The main objective of this thesis was to formulate a method with which solid fuel combustion characteristics could be accurately compared with one another. This meant developing the existing reactivity research equipment, mainly the DTR. An impactor style, liquid nitrogen quenched and cooled particle collecting system was incorporated into the reactor setup. It enabled collecting all the fed particles, thus making the mass loss tests faster and more accurate. Optical methods were combined with the DTR and utilized to determine the geometry and size distribution of the sample particles as a function of the conversion processes. This was an important addition, especially when examining biomass particles. Moreover, a two-color pyrometer was used to measure the combusting particles' surface temperature. These methods provided measurement data based on which the reactivity parameters of the sample fuels could be accurately determined. Using the discretized size distribution in the model calculations significantly improved the accuracy of the results. This advanced solid fuel characterization package was complemented with mercury porosimeter measurements, which provided information on the density and porosity of the samples.

The measurement setup was rather successful and it was suitable for all the tested samples. The greatest limitation of the system was that experiments with larger particles would have been harder to conduct in the DTR due to the short length of the reactor tube. The two-color pyrometer was also best suited to the particle sizes used in this work. The particle size and geometry measurement setup was able to provide information on the particle aspect ratio evolution as the conversion process advanced.

The determined reactivity parameters were used to compare the combustion behavior of five different samples tested in the DTR: coal, peat, raw wood, torrefied wood, and steam-exploded wood. It was noted that peat had the fastest conversion time with the same particle size and external environment. Coal, with the highest amount of residual char after pyrolysis, on the other hand represented the other end. The three biomass samples behaved in a similar manner in terms of reaction rates. The torrefied wood sample had a slightly faster conversion time compared to the other two. The greatest difference noted between the biomass samples was in the geometry of the particles after fine grinding them.

The steam-exploded sample particles were much more spherical after grinding, whereas the raw and torrefied wood particles were elongated. The particle shape change with torrefied and raw wood was also more severe than with the steam-exploded sample. The comparison between the O_2/N_2 and O_2/CO_2 atmosphere results revealed that the gasification reaction did not seem as significant with relation to the oxidation as the low heating rate studies would suggest.

In addition to the DTR tests, the fine grinding energy requirement was examined in relation to the biomass samples. Collaboration work was also conducted to examine the effect of torrefaction on the feedstock fine grinding energy requirement, chlorine content, and heating value. Various domestic and foreign wood species were used in these studies.The torrefaction process was noted to reduce the energy required to fine grind the tested sample. It was also noted that during torrefaction the chlorine content of the solid matter was reduced and the specific heating value was slightly increased. Fine grinding the steam exploded biomass produced more spherical particles compared to the raw and torrefied samples.

To summarize, the main contributions of this thesis are:

- Improving the existing DTR measurement techniques and equipment, especially the particle collection system that enables accurate particle residence time determination.
- Demonstrating how the measured particle surface temperature profiles in the DTR can be better explained using a distributed diameter model.
- Demonstrating that at high heating rates and with small biomass particles the gasification reaction is less significant with relation to oxidation than low heating rate experiments would imply.
- Demonstrating how steam-explosion treated woody biomass grinding produces more spherical particles compared to untreated feedstock.
- Demonstrating how torrefaction can be used to upgrade biomass feedstock in terms of reduced fine grinding energy requirement, increased specific heating value, and possibly reduced chlorine content.
- Suggesting a kinetic model based approach for solid fuel reactivity measurement data comparison.

Chapter 7

Future work

The main challenge related to future solid fuel reactivity research seems to be in generating a proper feedback loop with the end users of the results. Moreover, concerning combustion and pyrolysis model development, the question seems to be what purpose it serves. This thesis showed there is value in reactivity measurements and kinetics modeling as a comparison tool. Many studies have shown that the reactivity parameters derived from experimental work can be utilized in CFD calculations. However, a rigorous sensitivity study is needed for the entire research chain from the basic fuel analyzes to the calculation results from a CFD program. One of the key issues is to see how sensitive the calculation results are to errors in, e.g., the initial particle size distribution of a batch tested in a DTR. Implementing new improvements to the existing models can make them a little more accurate but can also make the calculation much heavier. The sensitivity analysis of the entire research chain would possibly enable pinpointing the easiest points of development in terms of making the results more accurate without complexifying the CFD calculation process too much.

In terms of developing the DTR measurement environment, larger particles need to be tested to understand better the internal heat and mass transfer limitations in practice. Larger particles would also enable studying the overlap of the pyrolysis and char oxidation processes. In this thesis the reactivity parameter results were generated with a rather narrow particle size fraction. However, it was noted that a wider fraction could be utilized if the size distribution was determined with the camera measurement setup. Also, a great deal of time and effort was consumed in trying to make the reactor temperature profiles as smooth as possible. In retrospect, this was mostly unnecessary. The DTR tests could be performed in a more random manner. The size distribution could be wider, the atmosphere conditions could vary more, and the reactor temperature profiles could be more irregular. These are all things that can be measured and given to the reactivity parameter optimization program as input values. Therefore, future DTR measurements would not have to be so strict as in this thesis. The determined reactivity parameters would in this way apply in a wider range and possibly some new phenomena could be drawn out.

The effect of thermochemical pretreatment methods on biomass feedstock grindability and other properties, such as hydrophobicity, has already been studied rather extensively. This thesis provided some insight into how torrefaction and steam explosion affect the fuel reactivity and especially the particle geometry that results from the grinding process. However, the effect of these methods on biomass based fuel behavior, such as slagging and fouling, in large furnaces is still somewhat unclear. It is well known that chlorine, alkali and alkaline earth metals are responsible for many undesirable reactions in furnaces. The reduction of these unwanted elements from the biomass fuels can be conducted with, e.g., water leaching or soaking. A question arises as to whether this reduction could be achieved cost effectively through or in conjunction with thermal pretreatment methods.

Bibliography

[1] G. Zhang, M. Reinmöller, M. Klinger, B. Meyer, Ash melting behavior and slag infiltration into alumina refractory simulating co-gasification of coal and biomass, Fuel 139 (2015) 457 – 465.

[2] B. Moghtaderi, The safety implication of low heating rate pyrolysis of coal/biomass blends in pulverised fuel boilers, Journal of Loss Prevention in the Process Industries 14 (2001) 161 – 165.

[3] L. Kokko, H. Tolvanen, K. Hämäläinen, R. Raiko, Comparing the energy required for fine grinding torrefied and fast heat treated pine, Biomass and Bioenergy 42 (2012) 219 – 223.

[4] V. Repellin, A. Govin, M. Rolland, R. Guyonnet, Energy requirement for fine grinding of torrefied wood, Biomass and Bioenergy 34 (2010) 923 – 930.

[5] R. L. Pereira, The chemistry involved in the steam treatment of lignocellulosic materials, Quím. Nova 26 (2003) 863 – 871.

[6] M. Gil, R. García, C. Pevida, F. Rubiera, Grindability and combustion behavior of coal and torrefied biomass blends, Bioresource Technology 191 (2015) 205 – 212.

[7] J. L. Goldfarb, C. Liu, Impact of blend ratio on the co-firing of a commercial torrefied biomass and coal via analysis of oxidation kinetics, Bioresource Technology 149 (2013) 208 – 215.

[8] X. Gu, C. Liu, X. Jiang, X. Ma, L. Li, K. Cheng, Z. Li, Thermal behavior and kinetics of the pyrolysis of the raw/steam exploded poplar wood sawdust, Journal of Analytical and Applied Pyrolysis 106 (2014) 177 – 186.

[9] D. S. Gunarathne, A. Mueller, S. Fleck, T. Kolb, J. K. Chmielewski, W. Yang, W. Blasiak, Gasification characteristics of steam exploded biomass in an updraft pilot scale gasifier, Energy 71 (2014) 496 – 506.

[10] J. Jones, T. Bridgeman, L. Darvell, B. Gudka, A. Saddawi, A. Williams, Combustion properties of torrefied willow compared with bituminous coals, Fuel Processing Technology 101 (2012) 1 – 9.

[11] Z. Sebestyén, E. Jakab, Z. May, B. Sipos, K. Réczey, Thermal behavior of native, washed and steam exploded lignocellulosic biomass samples, Journal of Analytical and Applied Pyrolysis 101 (2013) 61 – 71.

[12] A. Stroh, F. Alobaid, J.-P. Busch, J. Ströhle, B. Epple, 3-d numerical simulation for co-firing of torrefied biomass in a pulverized-fired 1 MWth combustion chamber, Energy 85 (2015) 105 – 116.

[13] A. Toptas, Y. Yildirim, G. Duman, J. Yanik, Combustion behavior of different kinds of torrefied biomass and their blends with lignite, Bioresource Technology 177 (2015) 328 – 336.

[14] Key world energy statistics 2014 (2014).

[15] Coal - energy for sustainable development (2012).

[16] B. Buhre, L. Elliott, C. Sheng, R. Gupta, T. Wall, Oxy-fuel combustion technology for coal-fired power generation, Progress in Energy and Combustion Science 31 (2005) 283 – 307.

[17] L. Chen, S. Z. Yong, A. F. Ghoniem, Oxy-fuel combustion of pulverized coal: Characterization, fundamentals, stabilization and CFD modeling, Progress in Energy and Combustion Science 38 (2012) 156 – 214.

[18] D. Lindberg, R. Backman, P. Chartrand, M. Hupa, Towards a comprehensive thermodynamic database for ash-forming elements in biomass and waste combustion - current situation and future developments, Fuel Processing Technology 105 (2013) 129 – 141.

[19] UN documents gathering a body of global agreements: Report of the world commission on environment and development: Our common future, World Commission on Environment and Development A/42/427 (1987).
URL `http://www.un-documents.net/wced-ocf.htm`

[20] 2006 IPCC guidelines for national greenhouse gas inventories: Glossary (2006).
URL `http://www.ipcc-nggip.iges.or.jp/public/2006gl/pdf/0_Overview/V0_2_Glossary.pdf`

[21] M. L. de Souza-Santos, Solid Fules Combustion and Gasification Modeling, Simulation, and Equipment Operation, Marcel Dekker, 2004.

[22] B. Leckner, Co-combustion - a summary of technology, Thermal Science 11 (2007) 5 – 40.

[23] Y. Shao, J. Wang, C. C. Xu, J. Zhu, F. Preto, G. Tourigny, C. Badour, H. Li, An experimental and modeling study of ash deposition behaviour for co-firing peat with lignite, Applied Energy 88 (2011) 2635 – 2640.

[24] H. Kassman, J. Pettersson, B.-M. Steenari, L.-E. Åmand, Two strategies to reduce gaseous KCl and chlorine in deposits during biomass combustion - injection of ammonium sulphate and co-combustion with peat, Fuel Processing Technology 105 (2013) 170 – 180.

[25] D. V. Krevelen, Coal - Typology - Physics - Chemistry - Constitution, third completely revised Edition, Elsevier Science Publishers B.V., 1993.

[26] R. H. Hurt, Structure, properties, and reactivity of solid fuels, Symposium (International) on Combustion 27 (1998) 2887 – 2904.

[27] A. Bharadwaj, L. L. Baxter, A. L. Robinson, Effects of intraparticle heat and mass transfer on biomass devolatilization: Experimental results and model predictions, Energy & Fuels 18 (2004) 1021 – 1031.

[28] M. J. Prins, Thermodynamic analysis of biomass gasification and torrefaction, Ph.D. thesis, Technische Universiteit Eindhoven (2005).

[29] M. J. P. Prins, K. J. Ptasinski, F. J. Janssen, Torrefaction of wood: Part 1. weight loss kinetics, Journal of Analytical and Applied Pyrolysis 77 (2006) 28 – 34.

[30] J. H. Peng, H. T. Bi, S. Sokhansanj, J. C. Lim, A study of particle size effect on biomass torrefaction and densification, Energy & Fuels 26 (2012) 3826 – 3839.

[31] M. Cantarella, L. Cantarella, A. Gallifuoco, A. Spera, F. Alfani, Comparison of different detoxification methods for steam-exploded poplar wood as a substrate for the bioproduction of ethanol in SHF and SSF, Process Biochemistry 39 (2004) 1533 – 1542.

[32] S. Turn, C. Kinoshita, W. Kaar, D. Ishimura, Measurements of gas phase carbon in steam explosion of biomass, Bioresource Technology 64 (1998) 71 – 75.

[33] P. S. Lam, Steam explosion of biomass to produce durable wood pellets, Ph.D. thesis, University of British Columbia (2011).

[34] O. Karlström, A. Brink, M. Hupa, Time dependent production of NO from combustion of large biomass char particles, Fuel 103 (2013) 524 – 532.

[35] R. Weber, T. Kupka, K. Zajac, Jet flames of a refuse derived fuel, Combustion and Flame 156 (2009) 922 – 927.

[36] M. B. Tilghman, R. E. Mitchell, Characterizing char particle fragmentation during pulverized coal combustion, Proceedings of the Combustion Institute 34 (2013) 2461 – 2469.

[37] L. Sørum, P. A. Campbell, N. E. L. Haugen, R. E. Mitchell, An experimental study of the reactivity of cellulosic-based chars from wastes, Fuel 130 (2014) 306 – 314.

[38] L.-P. Wiktorsson, W. Wanzl, Kinetic parameters for coal pyrolysis at low and high heating rates: a comparison of data from different laboratory equipment, Fuel 79 (2000) 701 – 716.

[39] F. F. Costa, G. Wang, M. Costa, Combustion kinetics and particle fragmentation of raw and torrified pine shells and olive stones in a drop tube furnace, Proceedings of the Combustion Institute 35 (2015) 3591 – 3599.

[40] K. Papadikis, S. Gu, A. Bridgwater, H. Gerhauser, Application of CFD to model fast pyrolysis of biomass, Fuel Processing Technology 90 (2009) 504 – 512.

[41] W. E. Ranz, J. W. R. Marshall, Evaporation from drops, part II, Chem. Eng. Prog. 48 (1952) 173 – 180.

[42] D. Merrick, Mathematical models of the thermal decomposition of coal: 2. specific heats and heats of reaction, Fuel 62 (1983) 540 – 546.

[43] C. Dupont, R. Chiriac, G. Gauthier, F. Toche, Heat capacity measurements of various biomass types and pyrolysis residues, Fuel 115 (2014) 644 – 651.

[44] J. Tomeczek, H. Palugniok, Specific heat capacity and enthalpy of coal pyrolysis at elevated temperatures, Fuel 75 (1996) 1089 – 1093.

[45] D. J. Maloney, R. Sampath, J. W. Zondlo, Heat capacity and thermal conductivity considerations for coal particles during the early stages of rapid heating, Combustion and Flame 116 (1999) 94 – 104.

[46] W. Sonderegger, S. Hering, P. Niemz, Thermal behaviour of norway spruce and european beech in and between the principal anatomical directions, Holzforschung 65 (2011) 369 – 375.

[47] M. Grønli, A theoretical and experimental study of the thermal degradation of biomass, Ph.D. thesis, The Norwegian University of Science and Technology (1996).

[48] P. R. Solomon, M. A. Serio, E. M. Suuberg, Coal pyrolysis: experiments, kinetic rates, and mechanisms, Progress in energy and combustion science 18 (1992) 133 – 220.

[49] P. R. Solomon, D. G. Hamblen, M. A. Serio, Z.-Z. Yu, S. Charpenay, A characterization method and model for predicting coal conversion behaviour, Fuel 72 (1993) 469 – 488.

[50] H. Kobayashi, J. Howard, , A. Sarofim, 16th symposium (international) on combustion, in: Coal Devolatilizationat High Temperatures, The Combustion Institute, 1976, pp. 411–425.

[51] J. Lehto, Development: and characterization of test reactor with results of its application to pyrolysis kinetic of peat and biomass fuels, Ph.D. thesis, Tampere University of Technology (2007).

[52] M. Rodriguez-Avila, Study of oxy-fuel combustion of single coal char particles: Experimental and modeling, Ph.D. thesis, Tampere University of Technology (2012).

[53] W. Fu, B. Zhang, S. Zheng, A relationship between the kinetic parameters of char combustion and the coal's properties, Combustion and Flame 109 (1997) 587 – 598.

[54] O. Karlström, A. Brink, J. Hercog, M. Hupa, L. Tognotti, 16th IFRF members' conference: Combustion and sustainability: new technologies, new fuels, new challenges, boston, in: Kinetic combustion parameters for chars using the IFRF solid fuel data base, 2009.

[55] I. W. Smith, The combustion rates of coal chars: A review, The Combustion Institute In 19th Symposium on Combustion (1982) 1045 – 1065.

[56] ANSYS Fluent Theory Guide, release 15.0 Edition, ANSYS, Inc., 2013.

[57] S. K. Bhatia, D. D. Perlmutter, A random pore model for fluid-solid reactions: I. isothermal, kinetic control, AIChE Journal 26 (1980) 379 – 386.

[58] J. Ochoa, M. Cassanello, P. Bonelli, A. Cukierman, CO_2 gasification of argentinean coal chars: a kinetic characterization, Fuel Processing Technology 74 (2001) 161 – 176.

[59] H. Umetsu, H. Watanabe, S. Kajitani, S. Umemoto, Analysis and modeling of char particle combustion with heat and multicomponent mass transfer, Combustion and Flame 161 (2014) 2177 – 2191.

[60] N. M. Laurendeau, Heterogeneous kinetics of coal char gasification and combustion, Progress in energy and combustion science 4 (1978) 221 – 270.

[61] R. C. Reid, J. M. Prausnitz, B. E. Poling, The Properties of Gases & Liquids, 4th Edition, McGraw-Hill, Inc. New York., 1987.

[62] A.F.Mills, Basic Heat and Mass Transfer, Prentice Hall, 1999.

[63] M. Simone, E. Biagini, C. Galletti, L. Tognotti, Evaluation of global biomass devolatilization kinetics in a drop tube reactor with CFD aided experiments, Fuel 88 (2009) 1818 – 1827.

[64] J. Ballester, S. Jiménez, Kinetic parameters for the oxidation of pulverised coal as measured from drop tube tests, Combustion and Flame 142 (2005) 210 – 222.

[65] F. Mermoud, S. Salvador, L. V. de Steene, F. Golfier, Influence of the pyrolysis heating rate on the steam gasification rate of large wood char particles, Fuel 85 (2006) 1473 – 1482.

[66] J. Lehto, Determination of kinetic parameters for Finnish milled peat using drop tube reactor and optical measurement techniques, Fuel 86 (2007) 1656 – 1663.

[67] A. D. Lewis, Sawdust pyrolysis and petroleum coke CO_2 gasification at high heat, Master's thesis, Brigham Young University, pp. 131-137 (2011).

[68] T. Joutsenoja, Pyrometric thermometry and sizing of fuel particles in combustion, Ph.D. thesis, TTKK (1998).

[69] M. Paananen, Kaksiväripyrometrian soveltaminen eri happipitoisuuksissa poltettavien kivihiilihiukkasten lämpötilan ja koon mittaamiseen, Master's thesis, Tampere University of Technology (2008).

[70] L. Kokko, A method for finding suitable particle sizes for thermal conversion processes by using a simulation tool focusing on wood particle heat transfer and chemical kinetics, Ph.D. thesis, Tampere University of Technology (2014).

[71] H. Lu, E. Ip, J. Scott, P. Foster, M. Vickers, L. L. Baxter, Effects of particle shape and size on devolatilization of biomass particle, Fuel 89 (2010) 1156 – 1168.

[72] M. Momeni, C. Yin, S. K. Kær, T. B. Hansen, P. A. Jensen, P. Glarborg, Experimental study on effects of particle shape and operating conditions on combustion characteristics of single biomass particles, Energy & Fuels 27 (2013) 507 – 514.

[73] J. Riaza, R. Khatami, Y. A. Levendis, L. Álvarez, M. V. Gil, C. Pevida, F. Rubiera, J. J. Pis, Single particle ignition and combustion of anthracite, semi-anthracite and bituminous coals in air and simulated oxy-fuel conditions, Combustion and Flame 161 (2014) 1096 – 1108.

[74] E. S. Hecht, C. R. Shaddix, M. Geier, A. Molina, B. S. Haynes, Effect of co2 and steam gasification reactions on the oxy-combustion of pulverized coal char, Combustion and Flame 159 (2012) 3437 – 3447.

[75] O. Karlström, A. Brink, M. Hupa, Desorption kinetics of CO in char oxidation and gasification in O_2, CO_2 and H_2O, Combustion and Flame 162 (2015) 788 – 796.

Appendix: Original publications

Publication I

Lauri Kokko, Henrik Tolvanen, Kai Hämäläinen, Risto Raiko

Comparing the energy required for fine grinding torrefied and fast heat treated pine

Biomass and Bioenergy, Volume 42, July 2012, Pages 219-223.

Available online at www.sciencedirect.com

SciVerse ScienceDirect

http://www.elsevier.com/locate/biombioe

Short communication

Comparing the energy required for fine grinding torrefied and fast heat treated pine

Lauri Kokko, Henrik Tolvanen, Kai Hämäläinen, Risto Raiko*

Department of Energy and Process Engineering, Tampere University of Technology, Korkeakoulunkatu 1, 33720 Tampere, Finland

ARTICLE INFO

Article history:
Received 19 January 2012
Received in revised form
13 March 2012
Accepted 14 March 2012
Available online 7 April 2012

Keywords:
Torrefaction
Grinding
Heating value
Pyrolysis
Fluidized bed

ABSTRACT

The purpose of the study was to compare torrefaction to partial pyrolysis conducted with a fast heat treatment process. Both torrefaction and the fast heat treatment tests were performed in a bubbling fluidized bed reactor. The study investigated the anhydrous weight losses, the fine grinding energy requirements, and the lower heating values of the samples produced with the two methods i.e. torrefaction and the fast heat treatment. The effect of particle size to these quantities was also investigated. The measurements demonstrated that the fine grinding energy requirement decreased rapidly as a function of anhydrous weight loss. The overall energy content remaining in the solid product decreased linearly as a function of anhydrous weight loss. The study shows that there is only little difference in the final products of the two processes when using particle sizes less than 4 mm. This means that it is possible to get similar products from the fast heat treatment process that takes only seconds compared to the slower torrefaction process that takes minutes.

1. Introduction

Depending on its origin biomass can be considered to be a carbon-neutral fuel source [1]. Biomass is also relatively evenly distributed around the world. Thus, it is very suitable for local energy production even if there is no well established national infrastructure for power generation. However, using biomass as an alternative fuel in already existing coal power plants is more complicated. A large proportion of these power plants operate by using pulverized fuel firing technology [2]. This means that in order to use biomass as a fuel source in these types of power plants; the fuel must first be ground into a suitable size fraction. The energy requirement for fine grinding fibrous biomasses is much higher than the energy required to grind fossil coal. One possible solution for lowering the energy required is to use heat treatment to achieve partial degradation of the holocellulose fraction in the biomass. This kind of treatment has a considerable impact on the fine grinding energy requirement [3]. Other challenges for the utilization of biomass in the already existing coal plants arise, for example, from the high alkali content of biomass materials. These challenges, however, are not discussed in this article [4].

Torrefaction is a process in which biomass is treated in temperatures under 300 °C [5]. Earlier studies have shown that the energy requirement of fine grinding decreases rapidly during torrefaction especially during the initial 10% mass loss [3]. Torrefaction, however, is a slow process, this is not desirable for industrial applications. A typical residence time of the feedstock in a pilot scale torrefaction reactor is

* *Corresponding author*. Tel.: +358 44 34 34 306.
E-mail address: lauri.kokko@tut.fi (L. Kokko).
0961-9534/$ – see front matter © 2012 Elsevier Ltd. All rights reserved.
doi:10.1016/j.biombioe.2012.03.008

10–60 min [6]. In this article torrefaction was compared to a more rapid heating process in which the particles undergo partial pyrolysis. The biomass for the tests was chosen to be Scots Pine (Pinus sylvestris). The rapid process in this study was chosen to last for 10 s, which is roughly the particle residence time in a circulating fluidized bed pyrolysator [7]. The idea was to compare the two processes by studying the evolutions of fine grinding energy requirement and lower heating value as a function of anhydrous weight loss.

2. Materials and methods

2.1. Experimental procedure

The wood samples examined in this study were sawed Pinus sylvestris timber. Torrefaction tests were conducted with 3 mm cubes. The fast heat treatment tests were conducted with 3, 4, 5, and 6 mm cubes. Both the torrefaction and the fast heat treatment tests were conducted in a laboratory scale bubbling fluidized bed reactor. After the thermal treatments, the mass loss of the samples was determined. The samples were fine ground and the grinding energy consumption was determined. For comparison a sample of high volatile C-bituminous fossil coal was also ground [8]. The coal sample was prepared by sieving a fraction using sieve sizes of 3.15 mm and 5 mm. The lower heating values of the pine samples were also determined.

2.2. Sample preparation

The samples were prepared by sawing pine plank with a band saw into different sized cubes. The cube sizes were selected to be 3, 4, 5, and 6 mm. The cube size of 3 mm was chosen because it was estimated to represent the smallest easily achievable chip size of an industrial chipper. This estimation was based on the average fiber length of pine. The cube size of 6 mm is the largest cube size suitable for easy operation of the necessary experimental setup for fine grinding energy requirement. Cube form was selected because it was considered to be the easiest to manufacture consistently. Furthermore, when using the cube form, the modeling of the internal heat transfer of the particles remains relatively simple. The sample size was approximately 5 g of oven-dry cubes.

2.3. Bubbling fluidized bed reactor

The bubbling fluidized bed reactor consisted of a flame resistant steel tube of which was 85.3 mm the inner diameter. Inside the tube was a kaowool grate which held a quartz sand bed in place. Pre-heated nitrogen was fed into the reactor from below the kaowool grate. The wood particles were fed into the reactor with a stainless steel cage. The residence time of the particles in the reactor was manually measured with a stopwatch. Manual measuring caused a small variation to the residence times due to human error. The temperature of the bed was constantly measured with a thermocouple placed in the sand. All sample particles were first oven-dried and weighed before feeding into the reactor. Quenching was done by removing the sample holding cage and submerging it into liquid nitrogen for a few seconds. After quenching the particles were oven-dried again to remove moisture that condensed from ambient air to the cold surface of the sample particles. Any remaining bed sand was removed from the samples and the samples were weighed.

2.4. Setup for measuring the fine grinding energy requirement

The main instrument of the fine grinding energy requirement setup was a Retsch ZM200 ultra-centrifugal mill. The mill was equipped with a 750 μm reinforced ring sieve and a 6 teeth stainless steel rotor. A Christ Elektronik CLM1000PP energy consumption meter was used for monitoring the power draw of the mill. The grinding energy requirement was calculated by subtracting the idle running power of the mill from the measured values. The idle running power of each run was determined by calculating an average of 10 s from the beginning of each measurement. The resulting power curve was then numerically integrated with the help of the trapezoidal rule. All grinding energy measurements were done with oven-dried samples which were allowed to cool down to room temperature in a desiccator for at least 15 min.

2.5. Lower heating value

The lower heating values of the samples were determined by Labtium Ltd. according to the CEN/TS 14918 standard. The heating values given in the results are calculated from the calorimetric heating values by subtracting a constant value of 1.349 MJ/kg from them [9].

3. Results and discussion

3.1. Anhydrous weight loss

The anhydrous weight loss of the torrefied samples was studied and the results are presented in Table 1.

The results for the anhydrous weight loss in the fast thermal treatment tests are given as a function of temperature and cube size, since the residence time was kept constant. The results are shown in Fig. 1.

Some of the measured points in Fig. 1 are inconsistent. This is most likely due to the inaccuracy in the manual residence time measurement or the heterogeneous nature of the samples.

Table 1 – The anhydrous weight loss (%) of torrefied pine.

Time (s)	Temperature			
	250 °C	275 °C	300 °C	325 °C
30	0.9	1.2	1.8	2.2
60	1.4	2.1	3.9	8.3
180	2.6	5.5	10.6	18.2
300	3.5	7.4	14.5	26.4
1800	7.1	18.4	32.8	56.0

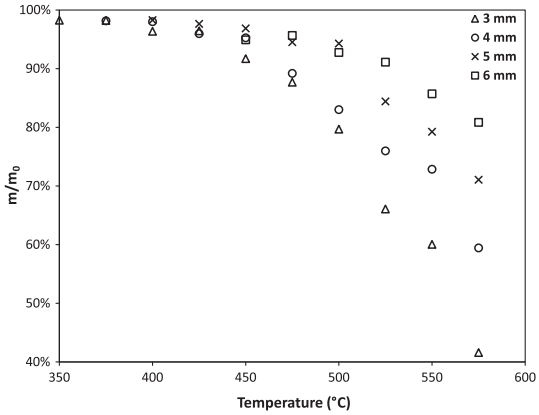

Fig. 1 – The anhydrous weight loss of the fast heat treated pine.

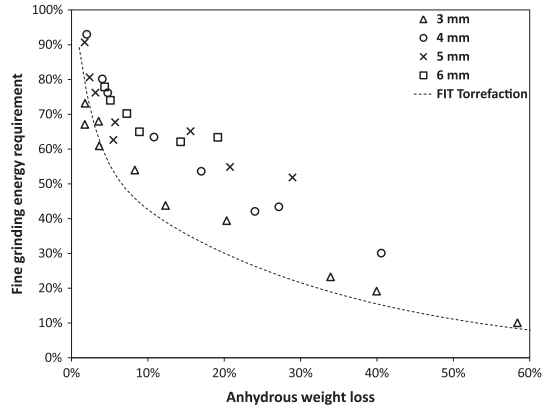

Fig. 3 – The fine grinding energy requirement for the fast heat treatment process and torrefaction as a function of anhydrous weight loss.

3.2. *Fine grinding energy requirement*

The fine grinding energy requirement was first measured for the torrefied samples. Since the fine grinding energy requirement is dependent on the grinding method, the figures are shown as percentual change compared to the untreated sample fine grinding energy requirement. This also makes the comparison of the different particle sizes more feasible since the fine grinding energy requirement also depends on the particle size. The fine grinding energy requirement for the fossil coal sample was compared to the fine grinding energy requirement of the raw 3 mm pine sample. The results are given in Fig. 2.

The results shown in Fig. 2 have a similar decreasing trend as those presented in Repellin et al., 2010 [3]. However, due to the difference in the ring sieve size, direct comparison of the results is not possible. A function fit for the grinding energy requirement as a function of mass loss was made for the torrefied samples. This was done for the purpose of comparing of the two processes i.e. torrefaction and fast heat treatment. The comparison and the results of the fine grinding energy requirement for the fast heat treatment process are presented in Fig. 3.

The fine grinding energy requirement measurement points for the 3 mm sized cubic particles seem to be very near to the curve fit obtained from the torrefied samples. As the particle size increases, the measurement points shift upwards and to the right from the curve, especially for weight loss values above 5%. There are some inconsistencies in the 5 mm particle size behavior compared to the 4 mm particle size. The difference is probably the result of a measurement error related to the grinding process.

3.3. *Lower heating value*

The results for the lower heating values of the torrefied wood samples are given in Fig. 4.

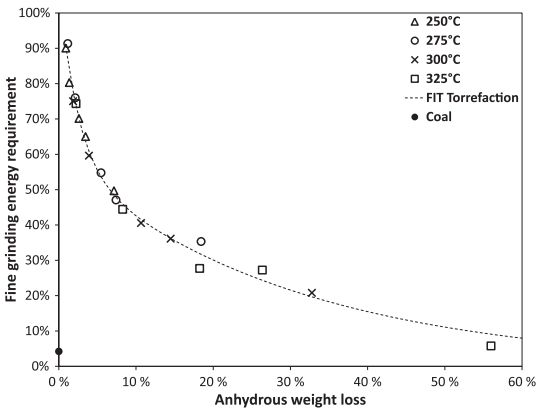

Fig. 2 – The fine grinding energy requirement for the torrefied samples as a function of anhydrous weight loss.

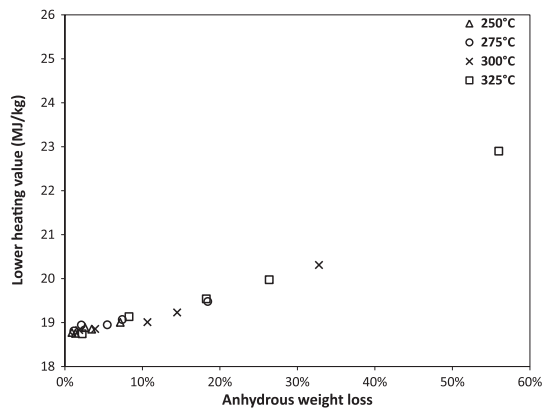

Fig. 4 – Lower heating values for the torrefied samples as a function of anhydrous weight loss.

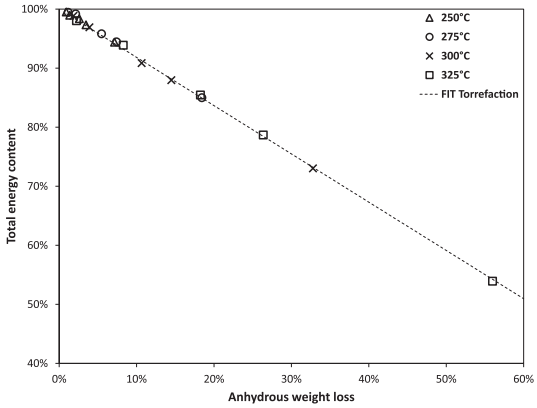

Fig. 5 – The total energy content of the solid product as a function of anhydrous weight loss.

Fig. 4 shows that the lower heating value of the samples clearly increase as a function of anhydrous weight loss. The ratio of the total energy content remaining in the solid product to the raw sample energy content is presented in Fig. 5.

By looking at Fig. 5, it is clear that even though the lower heating value of the samples increases, the net loss of energy is a linear function of anhydrous weight loss. A linear function fit was created in order to compare torrefaction and the fast heat treatment process. The comparison of the two methods is presented in Fig. 6.

Fig. 6 indicates that there is only little difference in the behavior of the total energy content for the two processes. However, the fast heat treatment process seems to lose slightly more of the total energy content from the solid as a function of anhydrous weight loss compared to the slow torrefaction process. A probable cause for this behavior is that in the fast heat treatment process the surface of the particle is almost completely charred while the center of the particle hardly reacts at all.

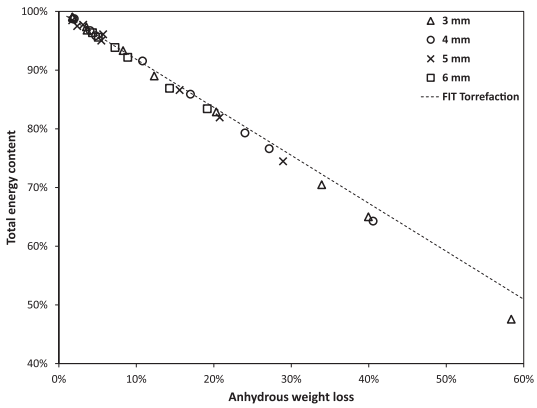

Fig. 6 – A comparison of the total energy content for fast heat treatment process and torrefaction.

4. Conclusion

The results for the torrefied samples are similar to those already presented in literature and therefore they are suitable when comparing of the two thermal pre-treatment methods [3,10]. The results from the fast heat treatment method indicate that it is a promising way to conduct torrefaction with smaller process units and with shorter residence times. However, the fast process has some disadvantages: more energy for fine grinding is required and slightly more of the solid's energy content is lost due to a conversion gradient in the particles. Nevertheless these disadvantages are only marginal when using a particle size less than 4 mm.

The financial feasibility of the two processes can be evaluated according to the results obtained from the study presented in this article. The mutual dependency of the fine grinding energy requirement and the total energy content left in the solid is now known. For a more thorough investigation of the financial feasibility one must also know the investment costs of the both processes, and the price of fine grinding energy compared to the price of the feedstock. A key issue is to find out how much conversion is really needed in order to reach the desired properties of torrefied fuel, for example, how much of the fine grinding energy requirement must be removed before the grindability is considered to be adequate. The storage properties of the torrefied fuel must also be studied to estimate the adequate stage of conversion.

Acknowledgments

The authors gratefully acknowledge the financial support of Metso Co. and UPM-Kymmene Co., for this study.

REFERENCES

[1] Reijnders L. Conditions for the sustainability of biomass based fuel use. Energ Policy 2006;34(7):863–76. doi:10.1016/j.enpol.2004.09.001. URL: http://www.sciencedirect.com/science/article/pii/S0301421504002915.

[2] Williams A, Pourkashanian M, Jones JM. Combustion of pulverised coal and biomass. Prog Energ Combust Sci 2001;27(6):587–610. doi:10.1016/S0360-1285(01)00004-1. URL: http://www.sciencedirect.com/science/article/pii/S0360128501000041.

[3] Repellin V, Govin A, Rolland M, Guyonnet R. Energy requirement for fine grinding of torrefied wood. Biomass Bioenerg 2010;34(7):923–30. doi:10.1016/j.biombioe.2010.01.039. URL: http://www.sciencedirect.com/science/article/pii/S096195341000053X.

[4] Skrifvars B-J, Hupa M, ja palaminen Poltto. International flame research foundation - Finnish flame research committee; 2002.

[5] Prins MJ, Ptasinski KJ, Janssen FJ. Torrefaction of wood: part 1. Weight loss kinetics. J Anal Appl Pyrolysis 2006;77(1):28–34. doi:10.1016/j.jaap.2006.01.002. URL: http://www.sciencedirect.com/science/article/pii/S0165237006000179.

[6] Kiel J, Verhoeff F, Zwart R. Torrefaction and pelletisation of biomass feedstocks. URL: http://www.ecn.nl/fileadmin/ecn/units/bio/Leaflets/b-11-018.pdf; 2011.

[7] Scott DS, Piskorz J, Bergougnou MA, Graham R, Overend RP. The role of temperature in the fast pyrolysis of cellulose and wood. Ind Eng Chem Res 1988;27(1):8–15. doi:10.1021/ie00073a003. URL: http://pubs.acs.org/doi/pdf/10.1021/ie00073a003. URL: http://pubs.acs.org/doi/abs/10.1021/ie00073a003.
[8] Smoot DL. Fossil fuel combustion a source book. John Wiley and Sons; 1991.
[9] Arvilommi S. Analyysituloksia. In: Tech Rep; 2011. Labtium Ltd.
[10] Chen W-H, Hsu H-C, Lu K-M, Lee W-J, Lin T-C. Thermal pretreatment of wood (lauan) block by torrefaction and its influence on the properties of the biomass. Energ 2011; 36(5):3012–21. doi:10.1016/j.energy.2011.02.045. URL: http://www.sciencedirect.com/science/article/pii/S0360544211001411.

Publication II

Henrik Tolvanen, Lauri Kokko, Risto Raiko

Fast pyrolysis of coal, peat, and torrefied wood: Mass loss study with a drop-tube reactor, particle geometry analysis, and kinetics modeling

Fuel, Volume 111, September 2013, Pages 148-156.

Fuel 111 (2013) 148–156

Contents lists available at SciVerse ScienceDirect

Fuel

journal homepage: www.elsevier.com/locate/fuel

Fast pyrolysis of coal, peat, and torrefied wood: Mass loss study with a drop-tube reactor, particle geometry analysis, and kinetics modeling

Henrik Tolvanen *, Lauri Kokko, Risto Raiko

Department of Chemistry and Bioengineering, Tampere University of Technology, Korkeakoulunkatu 1, 33720 Tampere, Finland

HIGHLIGHTS

- Drop-tube reactor should be coupled with optical study methods.
- Liquid nitrogen can be used to aid particle collection from drop-tube reactor.
- Particle geometry determination is necessary in biomass fast pyrolysis studies.
- Torrefied wood particle shape changes during pyrolysis with small particles.
- Density and initial volume measurements are crucial in pyrolysis modeling.

ARTICLE INFO

Article history:
Received 18 December 2012
Received in revised form 28 March 2013
Accepted 16 April 2013
Available online 4 May 2013

Keywords:
Pyrolysis
Coal
Peat
Torrefied wood
Chemical kinetics

ABSTRACT

The purpose of this study was to experimentally test and compare the fast pyrolysis behavior of torrefied wood, peat, and two types of coal. The experiments were conducted in a laboratory-scale drop-tube reactor (DTR) at a temperature range of 700–900 °C. Before pyrolysis, the sample particles were sieved with vibration sieves the opening of which was 100–125 μm. The initial size distribution of the sample particles and their diameter evolution during pyrolysis was studied by using optical techniques. According to the optical measurements particle swelling during pyrolysis occurred with the tested coal types but not with peat or torrefied wood. With torrefied wood the particle shape changed during pyrolysis from elongated to spherical. The density of the samples was measured with a mercury porosimeter. The mass loss of the sample particles during pyrolysis was modeled with two first order models: the single-step one reaction kinetics model and a model in which two reactions competed to form char and volatiles from the virgin matter. The kinetic parameters of the reactions and the diameter evolution equation coefficients were determined with both models and with all fuels. The optical measurement data from the particles was used to discretize the particle size distribution. The discretized size fractions were then used in the model calculations instead of a mono-sized single particle approach.

1. Introduction

Due to coal's significant role in energy production and its harmful environmental impacts, new clean combustion technologies need to be developed if the use of coal continues. In addition to creating cleaner combustion technologies, alternative fuels must also be found and researched to replace fossil coal as an energy source. Fortunately peat and torrefied wood can be considered as fuels capable of replacing fossil coal, to some extent even in the existing power plants. However, compared to coal these fuels have different pyrolysis and combustion properties [1,2]. The differences in the volatile yield and composition between these fuels can be a major issue. The chemical kinetics, porosity, and particle shape behavior of the torrefied wood may also cause problems for example in the operation of a fuel burner in a boiler. Therefore, the usage of bio fuels in power plants and especially the modeling of these processes require more in-depth information about the fuel behavior during pyrolysis and combustion.

Torrefied wood is thermally pretreated wood that has some of the good properties of fossil coal, such as hydrophobicity. The benefit of torrefied wood as a fuel is its ability to withstand outdoor storing without losing its heating value. Compared to untreated wood it is also easier to grind [3,4]. Moreover, torrefied wood can be considered to be carbon dioxide neutral fuel. Therefore, in the world of emissions trading, many energy production companies have expressed more interest towards it. Nevertheless, the effects of torrefaction on biomass pyrolysis and combustion have

* Corresponding author. Tel.: +358 40 86 16 718.
E-mail address: henrik.tolvanen@tut.fi (H. Tolvanen).

0016-2361/$ - see front matter © 2013 Elsevier Ltd. All rights reserved.
http://dx.doi.org/10.1016/j.fuel.2013.04.030

yet to be studied in depth. Since the torrefied wood has been planned as a replacement fuel for fossil coal, the kinetics studies should be conducted with coal references.

Laboratory-scale testing provides useful and necessary information on solid fuel behavior during pyrolysis. This information can be used later on when designing larger power plants and burning facilities. Plenty of laboratory-scale equipment has already been developed for pyrolysis and combustion research. For example, a drop-tube reactor (DTR) can be used to simulate the temperature level, atmosphere, and heating rate of fluidized bed combustion and pulverized fuel firing; processes that are characteristic for power plants. Among others [5] have noticed that pyrolysis kinetics change substantially when the heating rate varies. Therefore, new advanced experimental setups should be developed in order to provide insight on the behavior of both fossil fuels and different types of biomass under conditions that resemble those of industrial-scale plants. As a result of the high heating rate a DTR can be seen as a more appropriate tool for studying solid fuel pyrolysis than, for example, a thermogravimeter. Experimental and modeling studies have also been conducted in fluidized bed environment. Papadikis combined multiphase flows with discrete particle tracking by incorporating an external user defined function in FLUENT and modeled biomass particle fast pyrolysis in a bubbling fluidized bed reactor [6,7]. Bruchmüller's et al. [8] work investigated fast pyrolysis in a fluidized bed reactor from a particle-scale perspective taking also into account mixing, segregation and entrainment of the biomass. However, the measurement setup used in this work enables the investigation of the sample particles' actual size and shape before and after pyrolysis. This information is important if different particle geometries are taken into account in modeling. Among others Lu has showed in his work [9] that biomass particle shape has a great impact on the conversion rate.

Several types of models have already been presented in the literature and employed to describe the pyrolysis process of solid fuel particles [6]. However, despite the ability of these models to accurately describe the phenomena related to pyrolysis, strongly simplified kinetics models have also been used successfully [10,11]. If the results of these kinetic analyses are to be used in computational fluid dynamics (CFD) calculations, it is clear that complex models are more time demanding. Therefore, simplified models should be favored if their accuracy is close to the complex ones. Instead of complicated models the emphasis should be on defining accurate initial parameters for the modeling calculations. Thus, it is important to note that the initial parameters of pyrolysis modeling, such as fuel density and diameter distribution, have a tremendous effect on the calculated kinetic parameters. The novelty value of this work lies in the complementary usage of optical techniques and mercury porosimeter in the sample particle shape and mass determination as well as in the liquid nitrogen drop-tube reactor collecting system.

2. Materials and methods

2.1. Fuel composition and sample preparation

In this study, four different solid fuels were tested: two types of coal, peat, and torrefied wood. The two coal types formed a reference to which the peat and torrefied wood samples could be then compared. The ultimate and proximate analyses of the fuels were conducted by Enas Co. and the results are presented in Table 1.

It can be seen from Table 1 that there is only minor difference in the composition of the two coal samples. The largest fractional difference was in their sulfur content.

The torrefied wood sample material was received in the form of pellets. From the torrefied wood raw material 90% was softwood, and the rest was hardwood. The stem wood raw material was first chipped and then torrefied. The torrefaction was done at 250 °C in a continuous operated reactor. The residence time of the chips in the reactor was approximately 0.5 h. The mass yield of the torrefaction process was 89.6% from the original weight. The torrefied wood was then pelletized with a ring matrix pelletizer.

The density of the samples used in the experiments was measured with a Micromeritics Poresizer 9320 mercury porosimeter in the Department of Civil Engineering at Tampere University of Technology. The density measurements were conducted with the same sample particle size as used in the pyrolysis tests. The measured intrinsic (skeletal) density of the sample fuel materials and the evaluated apparent density values of the ground sample particles are presented in Table 2. The intrinsic density of the samples was calculated according to the mercury intrusion volume when all the pores greater than 6 nm were filled. The apparent density was evaluated with a mercury intrusion threshold of 26 μm. The threshold value was chosen according to the evaluated resolution of the already defined particle projection surface area. In the mercury intrusion volume curve as a function of average pore diameter, the 26 μm value appeared to be the point where mercury had filled most of the gaps between the particles and started intruding inside them. In this way, the evaluated particle apparent density and the particle volume based on image analysis could be used to calculate the mass of the particles.

The coal 1 sample batches treated at 700 °C and 850 °C were sieved with ring sieves sized 100–125 μm and the batch at 900 °C later on with 112–125 μm sieves. The coal 2 sample batches were all sieved with 100–125 μm sieves. The peat sample batches were sieved with 112–125 μm sieves but there were two different batches, one for 700 °C and 850 °C temperatures and one for 900 °C. Finally, the torrefied wood sample batches were all sieved with 112–125 μm sieves. Before sieving the samples were dried in an oven at 105 °C for 24 h and the crushed with a Retsch ZM 200 centrifugal mill. The sieving was conducted several times for a single sample with a vibration sieve in order to obtain a narrow size fraction. Between the sample preparation and the measurements, the sample was kept in an exicator with silica gel to remove the moisture from it. Therefore, in the modeling phase the particles were assumed to be dry when they entered the reactor.

2.2. Drop-tube reactor

The DTR system used in this study was designed by the first author. The design was based on the previous versions constructed at the Tampere University of Technology. The reactor consisted of three different modular parts: a feeding probe, a reactor part, and a new improved fuel collecting system. The reactor itself was an austenitic stainless steel tube with an inside diameter of 26.7 mm, and with a temperature resistance up to 1300 °C. The reactor was covered with 2–7 $\Omega\,m^{-1}$ resistance wire sets, which formed eight separately adjustable heating elements. The heating elements were insulated with an approximately 7 cm thick layer of kaowool. The heating zone length of the reactor was 65 cm and it was followed by 2.5 cm of unheated zone. The DTR and the auxiliary equipment are presented in Fig. 1.

Furthermore, windows for optical measurement purposes were built into the reactor, and they were placed at the lower end of the heating zone. The center point of the windows was 53.5 cm below the start of the heating zone. The windows were placed as low as possible in the reactor to enable particle velocity measurements with longer residence times. As already mentioned, after the heating zone end, there was a 2.5 cm section of unheated reactor tube, which was left between the resistance wires and the collecting system to prevent excess heating of the collecting vessel.

Table 1
The results of the ultimate and proximate analyses for the tested fuels.

Analysis	Peat	Coal 1	Coal 2	Torrefied wood	Unit
Ash content (815 °C)	7.1	13.7	15.4	0.2	dry wt.%
Volatile matter	65.4	34.5	31.4	81.9	dry wt.%
Sulfur	0.14	0.33	1.37	<0.02	dry wt.%
Carbon	52.6	67.8	64.8	53.2	dry wt.%
Hydrogen	5.5	4.6	4.5	6	dry wt.%
Nitrogen	1.24	2.04	2.07	<0.2	dry wt.%
Oxygen (calculated)	33.42	11.53	11.86	40.38	dry wt.%
Calorimetric heating value	20.96	28.05	28.2	21.07	MJ/kg
Lower heating value	19.76	27.06	27.24	19.77	MJ/kg

Table 2
The measured intrinsic densities of the samples and the evaluated apparent densities of the sample particles.

Sample	Intrinsic density (kg/m^3)	Apparent density (kg/m^3)
Peat	1245	459.7
Coal 1	1412	1050
Coal 2	1353	1251
Torrefied wood	1208	931.0

The main function of the feeding probe was to carry the particles to a wanted level inside the reactor and maintain them at a low enough temperature before entering the heating zone. The particles were inserted to the feeding probe from a feeding silo. Around the particle feeding tube was a water cooling jacket that kept the inside temperature of the probe at less than 80 °C. This ensured that the pyrolysis process of the sample particles started only after they entered the reactor itself. The temperature of the reactor wall was constantly measured from eight points and the gas temperature inside the reactor was measured before every run. From this data, average temperature profiles were first generated for the reactor wall and gas temperatures. These temperature profiles were then used in the energy balance equation as the gas and wall temperatures. The volume flow of nitrogen inside the reactor at 0 °C was 1.585 l mol^{-1}, which corresponded with the average gas velocities of 0.1735 m s^{-1}, 0.200 m s^{-1}, and 0.209 m s^{-1} at furnace temperatures of 700 °C, 850 °C and 900 °C respectively. The calculated Reynolds number for the reactor gas flow was well in the laminar zone in each of the aforementioned conditions.

The collecting system was designed to quench and cool down the particles very rapidly. This was achieved by floating the collecting vessel on liquid nitrogen. The vessel was placed near the reactor exit and while the gases erupted out from the edges, the collecting vessel acted as an impactor and collected the particles. The evaporating nitrogen kept the atmosphere totally inert. This collecting system improved the accuracy of the measurements significantly. As the drop-tube reactor was constructed the mass loss measurement accuracy was tested with coal and biomass particles. A simple way of testing the system accuracy was pyrolyzing sample particles in the reactor and increasing the reactor length after the final volatile yield was reached. If the yield stayed the same with greater particle falling lengths it meant that no particles were lost to the walls. Tests were also made in cold state to see whether all the particles that were fed were collected. The collecting system made it possible to collect all the particles that were dropped to the reactor, which in turn made the mass loss measurements simple and accurate.

2.3. High-speed camera

A high-speed camera was used for taking photographs of the particle stream inside the reactor through the measuring windows. The recorded pictures were then analyzed with a computer program in order to determine the velocity of the particles. The camera was an AVT Marlin 145-B2 with a 1380 × 1090 resolution and with a black and white CCD-cell. The camera was placed in front of the measurement windows, and the background led-light was placed to the opposite side of the reactor. The falling particles generated a double shadow to the image because of the pulsating LED-light located on the opposite side of the reactor. Based on the distance of the shadows and the time delay between the two pulses, the analysis program could determine the velocity of the particles. However, the images had to be scaled before the measurements.

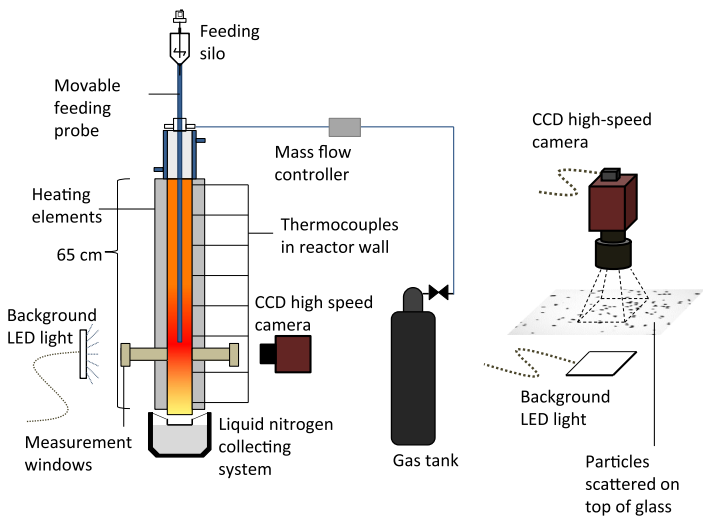

Fig. 1. A description of the DTR on the left and the diameter measurement system on the right.

Before recording, the camera was focused by running some particles through the reactor and adjusting the camera distance and aperture accordingly. Using a high-speed camera eliminated the need to calculate the particle residence time in the reactor with the particle motion equation. Instead, the velocity was first measured from several stages in the reactor by moving the position of the particle feeding probe. Based on these measurements, velocity profiles were generated for each cases and the residence time could then be integrated from them. An example of the velocity measurements and the generated fits can be seen in Fig. 2.

Fig. 2 shows that the velocity profile of the particles was not even, since there was a rather large increase in the gas velocity after the probe tip. However, it was visually observed that this acceleration in the speed did not spread the particle stream. The acceleration in the speed resulted from the geometry inside the reactor.

2.4. Determining particle diameter

The diameter of the particles was determined in a separate stage after the reactor treatment. First, the particles were scattered on a glass plate that was luminated from below. Here, the CCD camera was used to take pictures of the particle projections. On top of the plate the particles were easier to focus than while falling inside the reactor. The images were analyzed with a program developed by PhD Markus Honkanen from Tampere University of Technology. The analysis program recognized the particle projection outlines and calculated the pixel based projection area. In each diameter measurement round, altogether over thousand particles were detected from the images. The mass mean diameter of the sample particles could be determined by first calculating their volume and assuming they all had the same density. Fig. 3 illustrates the particle projection outline recognition of the crushed and sieved sample particles.

Fig. 3 shows remarkably that the vibration sieving process produced mostly homogeneously sized and shaped spherical particles with the coal samples. Unfortunately, this was not the case for peat and especially for torrefied wood. The torrefied wood particles were highly elongated. This can most likely be explained by the fibrous structure of wood. If the projection area of the torrefied wood and peat particles would have been considered as projection of a sphere, it would have highly exaggerated the initial particle mass. Therefore, the elongated particles were considered to be the shape of cylinders.

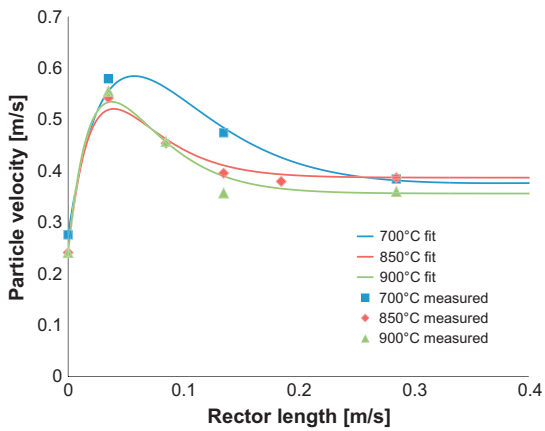

Fig. 2. The measured velocity values and the generated fits for the peat sample particles. The zero point in the horizontal axis represents the probe tip.

The analysis program made an ellipse fit to describe the particle dimensions and outlines. The dimensions of the ellipse could be used to estimate the sphericity of the particle. A set value of 1.5 was used for the individual particle ellipse maximum to minimum length ratio to distinguish between spheres and cylinders. If the particle had a ratio below 1.5 when calculating its volume, it was assumed as sphere when calculating its volume and if equal or over 1.5, the shape was assumed to be cylindrical. The cylinder thickness was calculated by dividing the projection area with the maximum ellipse length of the particle. The maximum ellipse length was used instead of the minimum, since the ellipse fit seemed to exaggerate the minimum length for the elongated particles. With this approach the particle volume could be calculated more accurately. The presented mass mean diameters were calculated backwards from the volume. For easier comparability, the presented diameters are those of a sphere with an equal volume. Therefore, the diameter values presented in this study describe more the volume change than the actual shape change of the particles. The heat transfer coefficient for all particles was calculated according to the spherical diameter. The particle size data in turn was used to calculate the volume distribution of the particles. Finally, the volume distribution was discretized for the modeling stage.

3. Modeling

3.1. Modeling the mass loss chemical kinetics

The mass loss chemical kinetics of the samples was modeled with two simple models: a one reaction and a two-competing reactions model. The one reaction model was chosen as it is commonly used in CFD calculations. The two competing reactions model was chosen to serve the need to preform solid fuel pyrolysis CFD calculations with a wider particle diameter distribution. The kinetic parameters related to the models were calculated with an optimization routine that minimized the difference between the measured values and the model prediction.

In the one reaction model there was a predetermined amount of volatiles in the particle that was released through one global reaction. The one reaction mass loss rate was expressed as follows:

$$-\frac{dm_p}{dt} = k(VM_0 - X_{DAF})m_0(1 - Ash) \quad (1)$$

The term m_p is the mass of the particle (kg) at given time, m_0 is the initial mass of the particle (kg), t is the time (s), k is the reaction rate coefficient (s^{-1}), and X_{DAF} is the conversion stage (–) of the particle that indicates the amount of fractional mass loss in dry ash-free (DAF) form. The term VM_0 describes the initial fractional amount of volatiles in the particle and it has to be determined at each temperature. It was also used in DAF form. The term Ash is the fractional amount of ash in the particle based on its initial dry mass. The reaction rate coefficient was of the Arrhenius form:

$$k = Ae^{\left(-\frac{E_a}{R_u T_p}\right)} \quad (2)$$

where A is the pre-exponential factor of the reaction rate coefficient (s^{-1}), E_a is the exponential factor of the reaction rate coefficient (J mol^{-1}), R_u is the universal gas constant (J mol^{-1} K^{-1}), and T_p is the particle temperature (K). In the two reaction model both reactions competed to form volatiles and char. Therefore, no predetermined amount of volatiles at a certain temperature was needed in the calculations. This was an advantage compared to the one reaction model. The mass loss rates of the two competing reactions were expressed as follows:

$$-\frac{dm_p}{dt} = \frac{dm_{volatiles}}{dt} = k_{volatiles}(1 - X_{char} - X_{volatiles})m_0(1 - Ash) \quad (3)$$

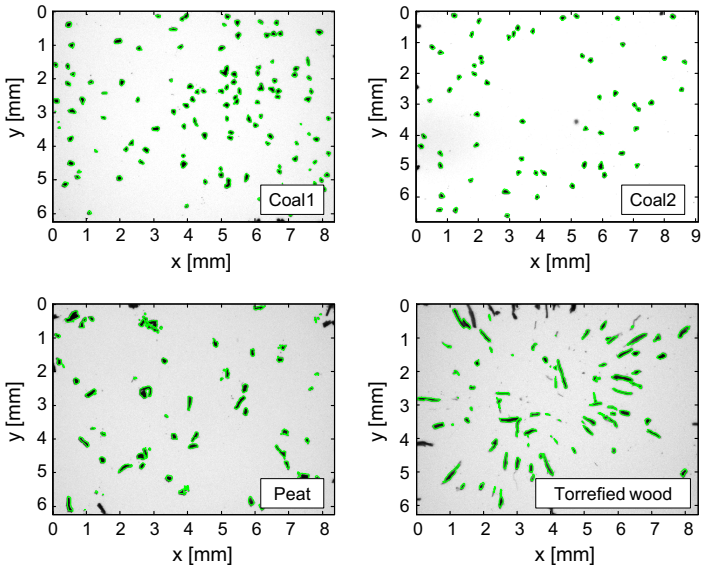

Fig. 3. The particle projection outline recognition with the diameter analysis program from the sieved sample parties before pyrolysis. The green line around the particles illustrates the outline recognition.

$$\frac{dm_{char}}{dt} = k_{char}(1 - X_{char} - X_{volatiles})m_0(1 - Ash) \tag{4}$$

where $m_{volatiles}$ is the amount of volatiles released (kg), m_{char} is the amount of virgin matter converted to char (kg), k_{char} and $k_{volatiles}$ describe the reaction rate coefficients for the char and volatiles formation reactions (s^{-1}) respectively. The term X_{char} is the fractional amount of DAF virgin material converted to char (–), and $X_{volatiles}$ is the fractional amount of DAF virgin material converted to volatiles (–). Both reactions stopped when all the virgin material had transformed into char or volatiles.

3.2. Modeling the particle diameter evolution

The diameter evolution for peat and torrefied wood particles during pyrolysis was modeled with the following equation:

$$d = d_0(1 - X)^{\beta} \tag{5}$$

where d is the diameter of the particle (m) at a given time and d_0 is the particle initial diameter (m). If the term β is 0, the particle diameter remains constant and its density decreases during pyrolysis. If β is negative it means that the particle size increases as the virgin matter conversion to volatiles advances. The maximum value of 1/3 for β describes a situation where the density remains constant and the diameter decreases. This equation was suitable to describe the shrinkage of the peat and torrefied wood particles during pyrolysis. Nevertheless, with the coal samples an additional term was introduced to the diameter evolution equation to describe the swelling that occurred especially at the highest temperature of 900 °C, where also the mass loss rate was the highest. Therefore, the swelling term was set to be dependent on the mass loss rate as follows:

$$d = d_0\left((1 - X)^{\beta} + \frac{dX}{dt}\varphi\right) \tag{6}$$

The coefficient φ described the magnitude of the swelling. In both Eqs. (5) and (6) the conversion stage X was in the dry form in the range of $0 \ldots X_{char}(1 - Ash)$.

3.3. Particle energy balance

The following equation describes the energy balance of the pyrolyzing particle in the DTR:

$$m_p c_p \frac{dT_p}{dt} = \theta A h_c (T_{gas} - T_p) + A_p \varepsilon \sigma \left(T_{wall}^4 - T_p^4\right) + h_{pyr}\frac{dm}{dt} \tag{7}$$

where m_p is the mass of the particle (kg), c_p is the specific heat capacity of the particle (J kg^{-1} K^{-1}), T_p is the temperature of the particle (K), t is the time (s), the term θ describes the effect of the Stefan flow on the particle convective heat transfer (–), A_p is the surface area of a spherical particle (m^2) with a diameter of d_p, h_c is the heat transfer coefficient (W m^{-2} K^{-1}), T_{gas} is the measured gas temperature in the rector (K), ε is the emissivity of the particle (–), σ is the Stefan–Boltzmann constant (W m^{-2} K^{-4}), T_{wall} is the measured wall temperature of the reactor (K), and h_{pyr} is the pyrolysis enthalpy (J kg^{-1}). The term on the left hand side describes the energy stored in the particle. The first term on the right hand side describes the heat convection to the particle from the surrounding gas, the second term describes the radiative heat transfer between the wall and the particle, and the third term describes the internal heat generation or consumption due to the chemical reactions taking place during pyrolysis. The heat transfer coefficient was calculated with the Ranz and Marshall [12] correlation. The heat capacity of the DAF material in the particle was modeled according to Merrick [13]:

$$c_{p,DAF} = \frac{R_u}{M_{ave}}\left[\left(\frac{T_{E1}}{T_p}\right)^2 \frac{e^{T_{E1}/T_p}}{\left(e^{T_{E1}/T_p} - 1\right)^2} + 2\left(\frac{T_{E2}}{T_p}\right)^2 \frac{e^{T_{E2}/T_p}}{\left(e^{T_{E2}/T_p} - 1\right)^2}\right] \tag{8}$$

where M_{ave} is the average molar mass of the elements in the DAF matter (kg^{-1} mol) and T_{E1} and T_{E2} are the Einstein temperatures (K). The Einstein temperatures selected for the heat capacity determining were 380 K and 1800 K. The heat capacity for the ash was calculated as follows:

$$c_{ash} = 754 + 0.586T_p \tag{9}$$

The Stefan flow term θ in the convection part of the energy balance equation was used as presented in [14]. The following correlation applies to the Reynolds numbers up to 400 [14]:

$$\theta = e^{(-0.6B)} \tag{10}$$

where B is related to the total gas release from a particle (–):

$$B = \frac{c_{vol}}{2\pi d_p k_g}\left(\frac{dm_p}{dt}\right) \tag{11}$$

Above c_{vol} is the heat capacity of the volatiles (J kg^{-1} K^{-1}) and k_g is the conductivity of the gas (W m^{-1} K^{-1}). As a result of the unknown content of the volatile gases, in this research article their heat capacity was assumed to be the same as that of carbon dioxide.

The emissivity of the particle in the radiation part was set to be 0.9 as proposed by [15]. Due to the small size of the particles the Biot number was small enough for the assumption that they were thermally thin. Studies suggest that biomass particle diameter of about 250 μm is the upper limit for a uniform temperature (Bi < 1) [16]. Also Papadikis et al. [7] showed in his calculations that with a convective heat transfer coefficient of approximately one third in comparison to the one in this study and with 500 μm particles the internal temperature gradient is negligible. Therefore, the internal heat transfer of the particles was not taken into consideration in the calculations in this study. The pyrolysis enthalpy for all the reactions in the two models was set to be 120 kJ kg^{-1}(endothermic). The particle temperature was solved from the energy balance equation by first linearizing the radiation term according to [17] and then discretizing the time dependance of the variables.

3.4. Discretizing the particle size distribution

The particle size distribution was calculated for the initial samples according to the analyzed diameter data. The distribution was discretized into ten equal-sized volume fractions. After this, the volume mean diameter of each fraction was calculated. The volume mean diameters obtained were then used as initial diameters in the model calculations. Thus, the model results were volume-averaged. The averaging was done as follows:

$$F_{avg} = \sum_{n=1}^{10} F_n v_n \tag{12}$$

where F_{avg} is the averaged variable (X, T_p, c_p, or d_p), F_n is a variable ($X_n, T_{p,n}, c_{p,n}$, or $d_{p,n}$) related to the nth volume fraction, and $v_n = 0.1$ is the volume fraction. Fig. 4 shows an example of the minimum, the maximum, and the volume-averaged mass loss values calculated with both models.

Fig. 4 shows that with the two competing reactions model the final mass loss levels of the volume fractions were not the same. This results from the different heating rates. With smaller particles the heating rate was higher and the temperature in the particles increased more rapidly. The higher temperature in the small particles favored the reaction that formed volatiles. With the one reaction model, the fixed amount of volatiles resulted in even final volatile matter amounts between the volume fractions. Due to the small particle size their terminal velocity was small compared to the gas velocity. Thus, the velocity of the particles in the reactor was assumed to be the same regardless of the particle size. Therefore, there was no difference in the residence times between different volume fractions.

3.5. Objective function and the optimization routine

A MATLAB-based objective function was written to determine the kinetic parameters of the selected reactions. The objective function minimized the square error between the mass loss and diameter model predictions and the measured values. The optimization routine used MATLAB's fminsearch function. The errors from the mass loss and diameter comparisons were summed in such a way that the mass loss error was emphasized ten fold compared to the diameter error. This was done because of the greater variance in the diameter measurements and because the mass loss was of greater importance when determining the chemical kinetic parameters. A lower limit of 20 kJ mol^{-1}was set for the exponential factors of the reaction rate coefficients.

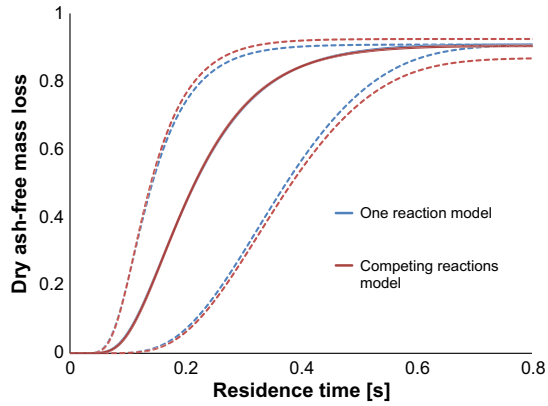

Fig. 4. The dry ash-free mass loss as a function of residence time for torrefied wood. The dashed lines are the maximum and minimum diameter groups and the middle one is the average value of all 10 volume fractions.

4. Results and discussion

4.1. Experimental and modeling results

The behavior of peat and torrefied wood during pyrolysis differed greatly from that of the two types of coal both in terms of diameter evolution and the rate of mass loss. The absolute reaction rates (kg s^{-1}) of the torrefied wood were much higher than those of the coals even though their densities were similar. It was also noted that during pyrolysis swelling of the particles occurred with the coals but not with peat or torrefied wood. The volume fractions of the samples that were determined based on the images from the initial samples are presented in Fig. 5.

The volumes of the particles for Fig. 5 were calculated according to the procedure described in the Section 2.4. The coal 1 histogram in Fig. 5 shows the effect of switching the lower sieve from 100 μm to 112 μm. For both coal types the diameter distribution is reasonable in relation to the sieve sizes. The peat and torrefied wood histograms, on the other hand show higher volume concentrations on significantly larger diameters than the sieve sizes. It can be explained with elongated particles and the spherical equivalent diameter calculation. This shows that if the initial mass of the particles is calculated purely based on the sieve opening sizes and an assumption of particle sphericity, the possibility of a major error increases.

The measured mass loss in DAF form and the diameter values along with the mass loss fit from the two-competing reactions model and the diameter evolution equation fit are presented in Figs. 6–9. The model values were calculated up to 40 cm reactor length. The one reaction model results are not presented in the figures. They were similar with the competing reactions model. However, the error function value was always greater in all the one reaction model results.

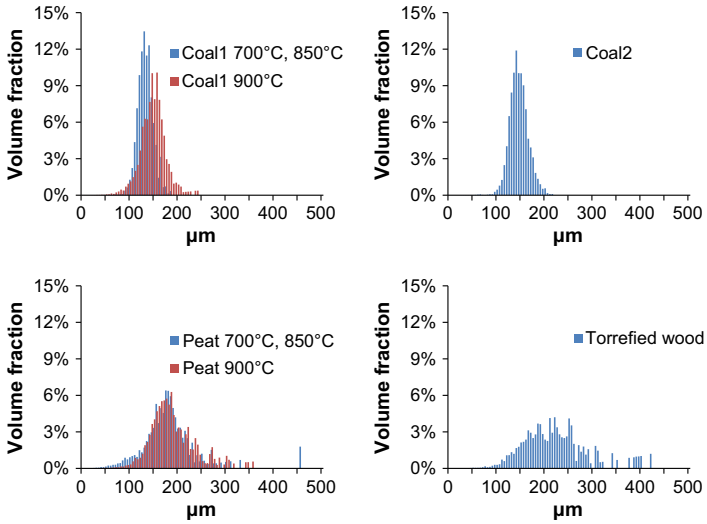

Fig. 5. The initial sample volume fractions based on the image analysis. The temperatures in the coal 1 and peat sample legends refer to the reactor temperatures at which the batches were used.

For easier comparability the measured diameter values in Figs. 7 and 9 were calculated based on particle volumes and presented as diameters of spheres with equal volumes. Fig. 6 shows that the competing-reactions model was able to describe the measured mass loss fairly accurately with coal 1. With peat the model did not meet the measured values as well at the two highest temperatures quite so well. In this study, torrefied wood had the highest mass loss rate during pyrolysis. With Peat, at 850 °C and 900 °C all the measured values were already close to the final volatile matter. It also seemed that no distinct isoconversion level was reached with peat, and the measured mass loss values slowly increased towards the end of the measurements. This can be explained, for example by slower reactions taking place or merely by a slight error in the mass loss measurements. These phenomena most likely reduced the accuracy of the determined kinetic parameters for the peat sample. However, in Fig. 8 the measured mass loss values matched the model prediction as closely as with coal 1.

The char yield for torrefied wood in Fig. 8 was approximately 5% in DAF form at 900 °C. A very similar value for woody biomass particles sized 0.35 mm char yield in a DTR was reported in [18]. The conversion profile of the torrefied wood particles is very similar to that reported by Umeki et al. [19] for same sized lignocellulosic biomass particles in an entrained flow reactor. The residence time differences in reaching the maximum conversion level might be due to different temperature profiles in the reactors. Lehto [11] reported a DAF volatile yield of approximately 88% for Finnish milled peat tested in a DTR at 800 °C with a same particle size fraction as used in this work. The volatile matter amount of peat differs from the one measured in this work most likely due to the different decomposition stages of the peat samples.

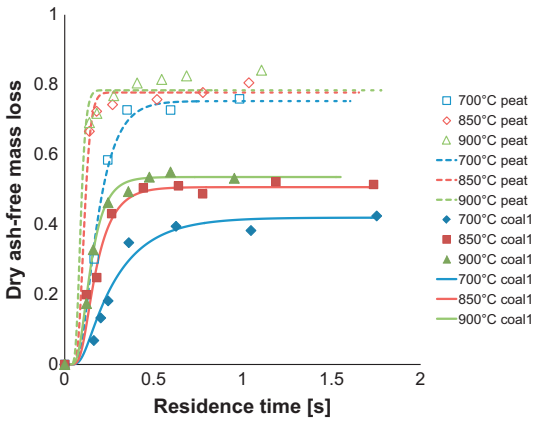

Fig. 6. The dry ash-free mass loss as a function of residence time for peat and coal 1. The dots represent the measured values and the continuous and the dashed lines the model.

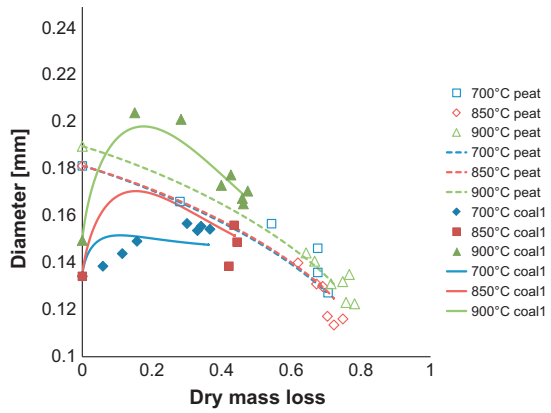

Fig. 7. The particle diameter evolution as a function of dry mass loss for peat and coal 1. The dots represent the measured values and the continuous and the dashed lines the model.

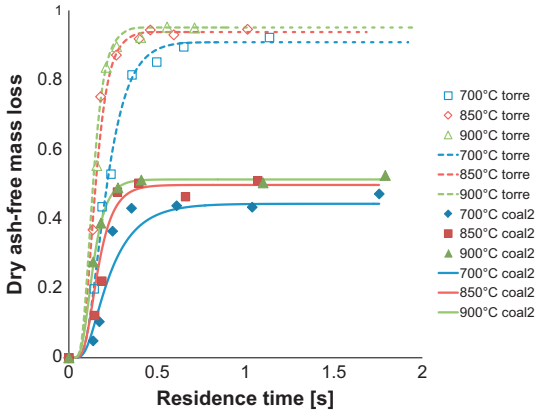

Fig. 8. The dry ash-free mass loss as a function of residence time for torrefied wood and coal 2. The dots represent the measured values, and the continuous and the dashed lines the model.

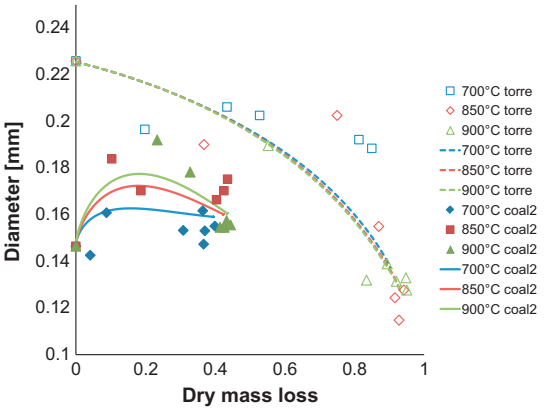

Fig. 9. The particle diameter evolution as a function of dry mass loss for torrefied wood and coal 2. The dots represent the measured values, and the continuous and the dashed lines the model.

The peat and coal 1 sample batches treated at 900 °C were different than those treated at 700 °C and 850 °C. Therefore, the initial volume mean diameter of the particles was somewhat different between them. This shows clearly in Fig. 7. Figs. 7 and 9 show that both coals swoll during the pyrolysis. However, the swelling did not occur with peat or torrefied wood.

Even though 112–125 μm sieves were used the sample particle initial diameters were much higher in each case as can be seen from Figs. 7 and 9. The deviation is most likely caused by the elongation of the particles, especially with the peat and torrefied wood samples. As the particles were scattered on top of the glass after pyrolysis they were on their side and thus created the largest possible projection from themselves. Even with the rather spherical coal particles this resulted in measured initial volume mean diameters that were slightly higher than the sieve sizes. The large initial diameter of the particles could also have been a result of too small resolution when imaging the particles. However, when the camera was zoomed closer, the results were more or less the same. The main goal in the imaging stage was to have as many particles in the picture with adequate resolution as possible.

The images that were taken for the diameter analysis also revealed the changes in the sample particle shapes during pyrolysis. First of all, the coal particles seemed to remain spherical. The peat sample particles also seemed to maintain their elongated shape.

Table 3
The one reaction model kinetic parameter and the diameter evolution equation coefficients.

Sample	(1/s)	(kJ/mol)	(–)	(–)
Peat	577,800	87.46	0.2806	–
Coal 1	1230	44.78	−0.2019	0.08049
Coal 2	1352	42.42	−0.1530	0.04265
Torrefied wood	19,250	56.78	0.1989	–

Table 4
The final volatile matter amount for the samples at each temperature measured with the DTR.

Sample	At 700 °C	At 850 °C	At 900 °C
Peat	0.6860	0.7249	0.7686
Coal 1	0.3459	0.4393	0.4656
Coal 2	0.3750	0.4209	0.4343
Torrefied wood	0.9067	0.9358	0.9489

Table 5
The two-competing-reactions kinetic parameters and the diameter evolution equation coefficients.

Sample	(1/s)	(kJ/mol)	(1/s)	(kJ/mol)	(–)	(–)
Peat	942,600	102.7	17,010,000	116.7	0.2930	–
Coal 1	276.2	37.20	5260	62.97	−0.2031	0.07606
Coal 2	420.0	38.23	1472	48.92	−0.1460	0.04323
Torrefied wood	10.95	20.00	34,550	61.44	0.2170	–

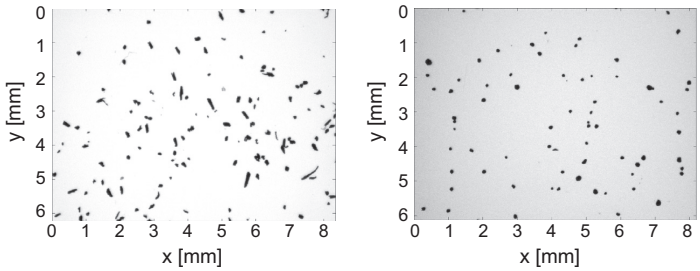

Fig. 10. The shape of the peat and torrefied wood sample particles at the end of pyrolysis. Both samples were treated at 850 °C for 40 cm in the reactor. Peat is on the left and torrefied wood on the right.

The torrefied wood sample particles, on the other hand looked like droplets at the end of pyrolysis. This can be seen in Fig. 10.

The same observation could be made from the ellipse fit maximum and minimum length based aspect ratios. With peat the aspect ratio remained close to the initial value, but the ratio for torrefied wood decreased so that in the end it was close to one. The reason for this behavior could be the differences in the chemical composition of the peat and torrefied wood samples. For instance, some of the components in torrefied wood may have liquid intermediates. Biagini et al. [20] reported slight decrease in the aspect ratio of woody biomass particles. The particles in Biagini's study were sized >0.3 mm. However, the change in the aspect ratio was not as high as observed in this study. Peat has a higher content of ligning compared to torrefied wood, which in turn has a higher amount of cellulose and hemicellulose in it. The high amount of lignin in peat could result as more durable shape structure of small particles during pyrolysis.

4.2. Fitted parameters

The chemical kinetic parameters and the diameter evolution equation coefficients were calculated with the MATLAB-based optimization algorithm by comparing the model prediction to the measurements conducted. The parameters related to the one reaction model are presented in Table 3.

The final volatile matter amounts for the sample fuels at all the measured pyrolysis temperatures are presented in Table 4.

The volatile matter amounts in Table 4 are in dry form. They were determined from the measured mass loss values by calculating the average of the mass loss after it had reached a clear plateau. The chemical kinetic parameters and the diameter evolution equation coefficients related to the two-competing-reactions model are presented Table 5.

The diameter evolution equation exponent β was negative and the swelling magnitude term φ was above zero for the coal samples in both Tables 3 and 5. This indicates that the diameter of the coal particles increased due to the swelling.

5. Conclusion

The constructed DTR measurement system proved to be a fast and accurate tool for conducting mass loss and diameter evolution measurements with coal and biomass particles. Especially the new liquid nitrogen quench collecting system and the particle falling velocity measurement with the high-speed camera eliminated a large number of uncertainties from the mass loss measurements and from determining the particle residence times. The measurements indicated that the from all the four tested fuels, torrefied wood had the greatest volatile matter amount. With all four fuels the final volatile yield in the DTR was larger than the proximate analysis had indicated. This shows again how important it is to use a suitable heating rate in chemical kinetic studies in relation to industrial applications. The optical study of the sample particles demonstrated that the sample material had a clear influence on the shape of the particles. With fibrous material the outcome of the preprocessing is most likely to be elongated or cylindrical particles. Therefore, if the initial mass of the particles is calculated purely based on the sieve sizes and on the assumption of spherical particle geometry, there is a possibility of great error. The image analysis also showed that with the torrefied wood sample the shape of the particles seemed to change from elongated to spherical during pyrolysis. The volume calculation based on particle projection coupled with the mercury-porosimeter-based density measurement offered means to improve the accuracy of the particle initial mass calculation. The two chosen pyrolysis models were able to describe the mass loss behavior of the fuels fairly well. Furthermore, the diameter evolution equations provided means to predict the volume change of the sample particles.

Acknowledgments

The authors gratefully acknowledge the financial support of Metso Co., Fortum Co., UPM-Kymmene Co., Pohjolan Voima Co., and Helen Co., for this study.

References

[1] Jones J, Bridgeman T, Darvell L, Gudka B, Saddawi A, Williams A. Combustion properties of torrefied willow compared with bituminous coals. Fuel Process Technol 2012;101(0):1–9. ISSN 0378-3820.
[2] Steenari B-M, Lindqvist O. Fly ash characteristics in co-combustion of wood with coal, oil or peat. Fuel 1999;78(4):479–88. ISSN 0016-2361.
[3] Kokko L, Tolvanen H, Hämäläinen K, Raiko R. Comparing the energy required for fine grinding torrefied and fast heat treated pine. Biomass Bioenergy 2012;42(0):219–23. ISSN 0961-9534.
[4] Repellin V, Govin A, Rolland M, Guyonnet R. Energy requirement for fine grinding of torrefied wood. Biomass Bioenergy 2010;34(7):923–30. ISSN 0961-9534.
[5] Wiktorsson L-P, Wanzl W. Kinetic parameters for coal pyrolysis at low and high heating rates: a comparison of data from different laboratory equipment. Fuel 2000;79(6):701–16. ISSN 0016-2361.
[6] Papadikis K, Gu S, Bridgwater A, Gerhauser H. Application of CFD to model fast pyrolysis of biomass. Fuel Process Technol 2009;90(4):504–12. ISSN 0378-3820.
[7] Papadikis K, Gu S, Bridgwater A. CFD modelling of the fast pyrolysis of biomass in fluidised bed reactors. Part B: Heat, momentum and mass transport in bubbling fluidised beds. Chem Eng Sci 2009;64(5):1036–45. ISSN 0009-2509.
[8] Bruchmüller J, van Wachem BGM, Gu S, Luo KH, Brown RC. Modeling the thermochemical degradation of biomass inside a fast pyrolysis fluidized bed reactor. AIChE J 2012;58(10):3030–42. ISSN 1547-5905.
[9] Lu H, Ip E, Scott J, Foster P, Vickers M, Baxter LL. Effects of particle shape and size on devolatilization of biomass particle. Fuel 2010;89(5):1156–68. ISSN 0016-2361.
[10] Blondeau J, Jeanmart H. Biomass pyrolysis in pulverized-fuel boilers: derivation of apparent kinetic parameters for inclusion in CFD codes. Proc Combust Inst 2011;33(2):1787–94. ISSN 1540-7489.
[11] Lehto J. Determination of kinetic parameters for Finnish milled peat using drop tube reactor and optical measurement techniques. Fuel 2007;86:1656–63. ISSN 0016-2361.
[12] Ranz JWE, Marshall WR. Evaporation from drops, part II. Chem Eng Prog 1952;48:173–80.
[13] Merrick D. Mathematical models of the thermal decomposition of coal: 2. Specific heats and heats of reaction. Fuel 1983;62(5):540–6. ISSN 0016-2361.
[14] Solomon PR, Serio MA, Suuberg EM. Coal pyrolysis: experiments, kinetic rates, and mechanisms. Prog Energy Combust Sci 1992;18:133–220.
[15] Solomon PR, Hamblen DG, Serio MA, Yu Z-Z, Charpenay S. A characterization method and model for predicting coal conversion behaviour. Fuel 1993;72(4):469–88. ISSN 0016-2361.
[16] Yang YB, Sharifi VN, Swithenbank J, Ma L, Darvell LI, Jones JM, et al. Combustion of a single particle of biomass. Energy Fuels 2008;22(1):306–16.
[17] Mills AF. Basic heat and mass transfer. Prentice Hall; 1999.
[18] Septien S, Valin S, Peyrot M, Spindler B, Salvador S. Influence of steam on gasification of millimetric wood particles in a drop tube reactor: experiments and modelling. Fuel 2013;103(0):1080–9. ISSN 0016-2361.
[19] Umeki K, Kirtania K, Chen L, Bhattacharya S. Fuel particle conversion of pulverized biomass during pyrolysis in an entrained flow reactor. Ind Eng Chem Res 2012;51(43):13973–9.
[20] Biagini E, Narducci P, Tognotti L. Size and structural characterization of lignin-cellulosic fuels after the rapid devolatilization. Fuel 2008;87(2):177–86. ISSN 0016-2361.

Publication III

Henrik Tolvanen, Risto Raiko

An experimental study and numerical modeling of combusting two coal chars in a drop-tube reactor: A comparison between N2/O2, CO2/O2, and N2/CO2/O2 atmospheres

Fuel, Volume 124, 15 May 2014, Pages 190-201.

Fuel 124 (2014) 190–201

Contents lists available at ScienceDirect

Fuel

journal homepage: www.elsevier.com/locate/fuel

An experimental study and numerical modeling of combusting two coal chars in a drop-tube reactor: A comparison between N_2/O_2, CO_2/O_2, and $N_2/CO_2/O_2$ atmospheres

Henrik Tolvanen *, Risto Raiko

Department of Chemistry and Bioengineering, Tampere University of Technology, Korkeakoulunkatu 8, 33720 Tampere, Finland

HIGHLIGHTS

- Combustion of coal char in a drop-tube reactor in N_2/O_2 and CO_2/O_2 was studied.
- Kinetic parameters were calculated for the oxidation and gasification reactions.
- Information on the particle size distribution is necessary for combustion modeling.
- Particle temperature decreased significantly when N_2 was replaced with CO_2.
- Gas property differences alone might not explain the temperature drop.

ARTICLE INFO

Article history:
Received 22 November 2013
Received in revised form 22 January 2014
Accepted 30 January 2014
Available online 13 February 2014

Keywords:
Char combustion
Coal
Chemical kinetics
Carbon dioxide
Oxy-fuel

ABSTRACT

The purpose of this study was to examine how CO_2 affects the burning behavior of two coal chars, char 1 and char 2. The work consisted of experiments and numerical modeling. The experiments were conducted under high heating rates in a laboratory-scale drop-tube reactor (DTR). The char samples were produced by pyrolyzing coal particles in the DTR at 850 °C in pure N_2. Before pyrolysis, the coal particles were ground and sieved to a particle size fraction of 100–125 μm. The mass loss of the char particles was determined after the DTR combustion process. The surface temperature of the char particles was measured with a two-color pyrometer during combustion. The diameter evolution and the falling velocity of the particles were studied optically with a CCD high-speed camera. The oxygen concentrations used in the measurements were 2–12 vol.% in either N_2 or CO_2. The combustion was assumed to take place within the Zone I and Zone II regimes. Zone I describes the conditions where the combustion process is controlled by chemical kinetics. In Zone II both chemical kinetics and intraparticle diffusion control the combustion. With char 2 the effect of replacing N_2 gradually with CO_2 was also tested. This was done for the purpose of examining the interactions of the oxidation and CO_2 gasification reactions. When the N_2 was entirely replaced with CO_2 from the reactor atmosphere, the mass loss rate of both chars decreased slightly compared to the N_2 setting. A more drastic decrease was observed in the particle surface temperature. This study also presents the numerical modeling results of combusting the two coal chars in the DTR in N_2/O_2 and CO_2/O_2 atmospheres. The apparent chemical kinetic parameters of the oxidation reactions were calculated based on the measurement results in the N_2/O_2 atmosphere. The apparent chemical kinetic parameters of the CO_2 gasification reaction were also calculated for char 2. In the modeling calculations the internal heat transfer of the char particles, oxygen diffusion in the boundary layer, Stefan flow, and the size distribution of the particles were taken into consideration. The modeling results indicated the importance of determining the initial size distribution of the sample particles. An average diameter model could not explain the large variation in the measured particle surface temperatures. As a result, a comparison between the modeling results and the measurement results suggested that high CO_2 partial pressure in the combustion atmosphere can affect the combustion process in other ways than merely through the differences in the gas properties.

* Corresponding author. Tel.: +358 40 86 16 718.
E-mail address: henrik.tolvanen@tut.fi (H. Tolvanen).

http://dx.doi.org/10.1016/j.fuel.2014.01.103
0016-2361/

1. Introduction

Demand for electricity is increasing throughout the world, but especially in developing countries. A growing concern about climate change will most likely generate pressure to reduce the use of fossil fuels. Due to coal's significant role in energy production and its harmful environmental effects, new clean combustion technologies need to be developed, if the use of coal continues. One possibility towards carbon–neutral coal usage is the carbon capture and storage (CCS) technology. Several applications are being developed for CO_2 capture and sequestration from coal-fired plants. Among them, oxy-fuel combustion is one of the most economical [1]. It is also the most likely technology to be employed when retrofitting existing coal-fired power plants [2]. However, there are still several hurdles to overcome before oxy-fuel combustion can fully be commercialized.

The main difference between oxy-fuel combustion and the conventional technologies is the significantly higher CO_2 partial pressure. The elevated CO_2 levels have been noted to affect the coal combustion process e.g. as a result of its higher specific heat [3] and differences in the oxygen diffusivity [4]. Bejarano and Levendis [5] studied the combustion of single coal particles in O_2/N_2 and O_2/CO_2 environments in a drop-tube reactor (DTR) at 1127 °C and 1327 °C. Their observation was that coal particles burned at higher mean temperatures and more rapid combustion times in O_2/N_2 than in O_2/CO_2 environments.

Based on their literature review, Hecht et al. [6] suggested that the apparent relative rate of the $C + CO_2$ reaction to the $C + O_2$ reaction is roughly $0.1–3.0 \times 10^{-4}$ at 1073 K. Considering that the gasification reaction has an activation energy of approximately 250 kJ/mol, they suggested that these relative rates scale to values of $0.1–3.0 \times 10^{-2}$ at a typical pulverized coal char combustion temperature of 2000 K. This would suggest that the CO_2 gasification reaction has a very minor effect on the overall combustion process. However, Senneca and Cortese concluded in their article [7] that the assumption that the reactions with oxygen and CO_2 occur in parallel, without interactions, and with no distinction as regards the nature of the carbon active sites, is probably inappropriate to describe the kinetics of char oxy-combustion. Umemoto et al. concluded in their article [8] that their modified Langmuir–Hinshelwood gasification model proposed that CO_2 gasification and H_2O gasification share partially active sites. One goal of this work was to find out if such interaction between the oxidation and gasification reactions could clearly be seen with the tested fuels. However, even with the results of this work, the matter remains unclear.

This article concentrates on examining the effect of CO_2 partial pressure on char particle combustion temperature and mass loss rate. Similar studies of pulverized coal combustion in oxy-fuel conditions have been recently conducted in DTR, e.g. by [3,9–11]. The measurement setup in this work offers the possibility to accurately determine the residence time of the sample particles in the reactor, and presents a liquid N_2 quenching system for the collected particles. In addition, the sample particle size distribution measurement system and the use of the diameter distribution instead of a single mono-sized particle model in the calculations seemed to be more capable of providing explanations to the particle surface temperature measurement results. Calculating the oxidation reaction kinetic parameters requires knowledge on both the mass loss of the sample particles, and their temperature history.

2. Materials and methods

2.1. Fuel composition and sample preparation

Both char samples were produced from bituminous coals. The ultimate and proximate analysis of the coal samples are presented in Table 1. The original coal samples are referred to as coal 1 and coal 2. The char samples were produced from the coals by pyrolyzing them in the DTR at 850 °C in pure N_2. Before pyrolysis, the coals were ground and sieved to a size fraction of 100–125 μm. The volatile matter amounts of the coals in dry form measured in the DTR were 0.439 for coal 1 and 0.421 for coal 2. Both coals swelled during pyrolysis, and thus the final mass mean diameter after pyrolysis was slightly greater than the initial diameter. To avoid absorption of moisture or impurities, the char samples were stored in air sealed containers. A comparison of the initial size distributions of the char samples is presented in Fig. 1.

Table 1
The results of the ultimate and proximate analyses for the tested coals.

Analysis	Coal 1	Coal 2	Unit
Ash content (815 °C)	13.7	15.4	dry wt%
Volatile matter	34.5	31.4	dry wt%
Sulfur	0.33	1.37	dry wt%
Carbon	67.8	64.8	dry wt%
Hydrogen	4.6	4.5	dry wt%
Nitrogen	2.04	2.07	dry wt%
Oxygen (calculated)	11.53	11.86	dry wt%
Calorimetric heating value	28.05	28.2	MJ/kg
Lower heating value	27.06	27.24	MJ/kg

The density of the char particles was calculated according to the density of the coal samples and the volatile matter amount released in the DTR. The size change of the particles during pyrolysis was so minor that it was not taken into account in the density calculation. The densities of the sample particles for char 1 and char 2 were 589 kg/m^3 and 724 kg/m^3 respectively. In the modeling calculations the char particles were assumed to consist of elementary carbon and ash.

2.2. Drop-tube reactor

The DTR system used in this study was designed by the first author. The design was based on previous versions constructed at Tampere University of Technology (TUT). The same reactor was used in the pyrolysis study of the two coals examined in this work [12]. The reactor design, the reactor temperature profile, and the auxiliary devices are presented in Fig. 2.

In this study, the only difference compared to the previous reactor setup was the use of a two-color pyrometer. Fig. 2 shows how the CCD camera and the two-color pyrometer were placed on the

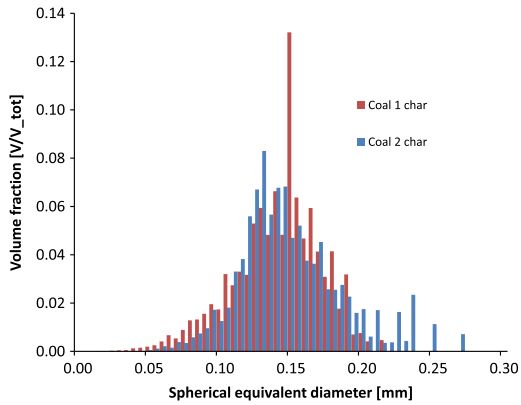

Fig. 1. The initial sample volume fractions, which were determined on the basis of the image analysis, as a function of the spherical equivalent diameter.

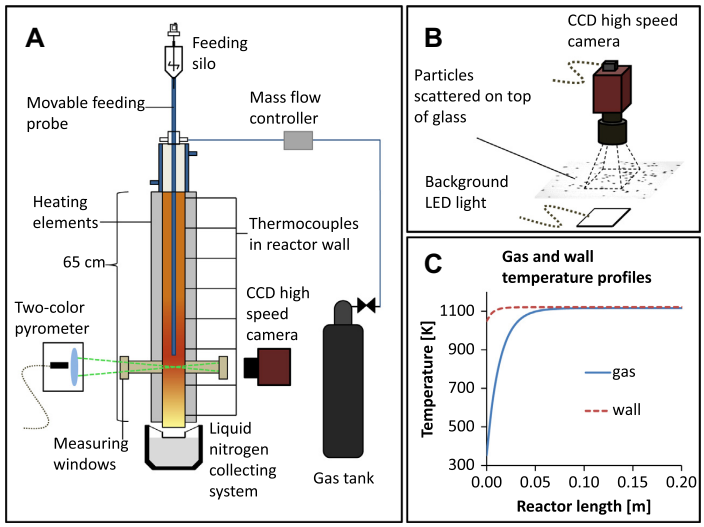

Fig. 2. A description of the DTR (A), particle diameter measurement system (B), and the DTR gas and wall temperature profiles (C). In the graph shown in section C the beginning of the x-axis corresponds to the movable feeding probe tip shown in section A.

opposite sites of the reactor. However, a simultaneous measurement with the camera and the pyrometer was not possible. The camera required an LED background light and as the pyrometer was used the windows were covered to avoid any background radiation. The reactor quartz window material was chosen so that it would cause as little interference to the pyrometric measurements as possible.

The DTR gas temperature was measured with a thermocouple from the center line of the reactor. The gas temperature could only be measured before the actual char combustion tests. The wall temperature was monitored with eight separate thermocouples. These thermocouples were placed in cavities drilled for them in the reactor wall. The gas and wall temperatures were measured before every run. Based on these measurements analytical functions were generated to describe the average gas and wall temperatures as functions of the reactor length. These temperature profiles are shown in Fig. 2C. The presented temperature profiles were used in all the calculation cases.

The gases used in the measurements have different thermal properties and replacing N_2 with CO_2 changed the gas and wall temperatures slightly. However, every time the measurement setup was changed the reactor heating elements were adjusted to obtain a similar temperature profile as in the previous runs. This procedure did not by any means guarantee that the temperature profiles during every reactor setup would have been exactly the same. With the shorter reactor lengths especially the measured gas temperature rise was a little sharper than with the longer ones. Nevertheless, the vast amount of the measurement setups and the degree of the difference compelled the authors to use the average temperature profiles.

Due to the structure of the reactor, the gas temperature was measured without a radiation shield. Therefore, the measured temperature had to be corrected for the calculations. The correction was made following the principles presented in [13].

The particles were inserted to the feeding probe from a feeding silo shown in Fig. 2A. Around the particle feeding tube was a water cooling jacket that kept the inside temperature of the probe at less than 80 °C. This ensured that the combustion process of the sample particles started only after they entered the reactor itself. The particle feeding rate to the reactor was approximately 0.005 g of char per minute. With this rate the char combustion was not assumed to reduce the bulk gas oxygen concentration or increase the gas temperature.

For char 1 the measurements were conducted at a reactor temperature of 1123 K in 2, 3, 6, and 8 vol.% of O_2 in both N_2 and CO_2. For char 2, the O_2 concentrations were 3, 6, 10, and 12 vol.% of O_2 in both N_2 and CO_2. An additional set of tests, in which the O_2 concentration was kept constant at 12 vol.% and the N_2 was gradually replaced with CO_2, was made for char 2. The N_2/CO_2 concentrations in these cases were 88/0, 68/20, 48/40, 28/60, 8/80, and 0/88 vol.%. The low O_2 concentrations were chosen in order to emphasize the role of chemical kinetics and to increase the time resolution of the process.

2.3. High-speed camera

A high-speed camera was used for taking photographs of the particle stream inside the reactor through the measuring windows. To determine the velocity of the particles the photographs were then analyzed with a computer program. The camera was an AVT Marlin 145-B2 with 1380 × 1090 resolution and with a black and white CCD-cell. The camera was placed in front of the measurement windows, and a background LED-light was placed to the opposite side of the reactor. The falling particles generated a double shadow to the image because of the pulsating LED-light located on the opposite side of the reactor. Based on the distance of the shadows and the time delay between the two pulses, the analysis program could determine the velocity of the particles. However, the images had to be scaled before the measurements.

Before the actual pyrolysis, the camera was focused by running some particles through the reactor and by adjusting the camera distance and aperture accordingly. Using a high-speed camera eliminated the need to calculate the particle residence time in the reactor with the particle motion equation. Instead, the velocity was first measured from several sections in the reactor by moving the position of the particle feeding probe. Based on these measurements, velocity profiles for each measurement case were generated. These velocity functions described the particle falling

velocity as a function of the reactor length. First the reactor length was divided into small place steps. A constant velocity was assumed inside the step. The value was determined based on the velocity function. Thus, the length and the particle velocity inside the steps was known and the residence time of the particles along the reactor length could be calculated. An example of the velocity profiles is given in [12]. There was a clear acceleration in particle velocity immediately after they entered the reactor from the probe. The acceleration in the speed was resulted from the reactor geometry and the flow conditions inside. However, it was visually observed that this acceleration in the speed did not spread the particle stream.

2.4. Determining particle diameter

The particle volume mean diameter was determined in a separate stage after the reactor treatment. First, the particles were scattered on a glass plate that was illuminated from belo was shown in Fig. 2B. The CCD camera was used to take pictures of the particle projections. On top of the plate the particles were easier to focus than while falling inside the reactor. The images were analyzed with a program developed by PhD Markus Honkanen from TUT. The program is described in more detail in his article [14]. The analysis program recognized the particle projection outlines and calculated the pixel-based projection area. In each diameter measurement round, altogether over thousand particles were detected from the images. The mass mean diameter of the sample particles could be determined by first calculating their volume and assuming they all had the same density. The particles were categorized to spheres and cylinders based on their minimum and maximum lengths. If the ratio of the particle's maximum to minimum length was under 1.5 it was assumed to be a sphere, otherwise a cylinder. The presented mass mean diameters were calculated backwards from the determined particle volumes. For easier comparability, all the presented diameters are of a sphere with an equal volume.

2.5. Two-color pyrometer

The two-color pyrometer used in the measurements was assembled by M.Sc. Matti Paananen from the Department of Physics at TUT. The two-color pyrometer measured particle radiation with two narrow wavelength bands. The temperature of the combusting particle could then be determined from the ratio of these wavelength measurements. The chosen wavelength bands were 1.0 and 1.6 μm for the main signals, and 1.25 μm for the reference signa l. The bandwidths for the 1.0 and 1.6 μm wavelength bands were 125 and 67 nm respectively. The selection of the wavelengths was mainly dependent on the following factors: there had to be enough spectral radiation at the selected wavelengths and at the reactor temperatures, and the effect of thermal radiation absorbing into the reactor gases had to be minimized. Transferring the radiation of the particles from the optic's focal point to the detector was carried out with a 1 mm diameter main optical fiber. Ensuring that only one particle at a time was measured was realized with 0.1 mm diameter reference fibers placed around the main fiber. These reference fibers were used to detect when a single particle was entirely in the main fiber's field of view. The pyrometer used in this study was mainly based on the creation of [15].

3. Modeling

3.1. Particle energy balance

In the combustion modeling the particles were assumed to be spherical and they were divided into 50 cores, each of which had the same initial volume. The energy balance equation was solved numerically, and each core had its own carbon consumption reaction rate and properties based on its temperature. The core thickness was calculated again at each step according to the mass loss and the volume change equation. The general energy balance equation for a combusting char particle can be written as:

$$\frac{\partial\left(\rho_p T_p\right)}{\partial t} = \frac{1}{c_p}\frac{1}{r^2}\left(\frac{\partial}{\partial r} r^2 k_p \frac{\partial T_p}{\partial r}\right) + \frac{1}{c_p}\dot{r}(-\Delta h), \tag{1}$$

where ρ_p is the density of the particle (kg m^{-3}), c_p is the heat capacity of the particle (J kg^{-1} K^{-1}), t is the time (s), r is the radius of the particle (m), k_p is the heat conductivity (W m^{-1} K^{-1}), T_p is the temperature of the particle (K), $\dot{r}$ is the reaction rate at which carbon is consumed (kg s^{-1}), and Δh is the reaction enthalpy (J kg^{-1}). The reaction enthalpies of the oxidation and gasification reactions were found from literature, e.g [16]. The term on the left hand side describes the energy stored in the particle. The first term on the right hand side describes the heat conduction, and the second term the internal heat generation or consumption due to the chemical reactions taking place during the combustion process. As a result of symmetry, the heat flux is zero at the particle center point. The boundary condition for the particle surface can be written as:

$$-k_p \frac{\partial T_p}{\partial r} = \theta h_c\left(T_{gas} - T_p\right) + \varepsilon\sigma\left(T_{wall}^4 - T_p^4\right), \tag{2}$$

where θ is a coefficient related to the Stefan flow (–), h_c is the convective heat transfer coefficient (W m^{-2} K^{-1}), T_{gas} is the gas temperature (K), T_{wall} is the wall temperature (K), ε is the emissivity of the particle, and σ is the Stefan–Boltzmann constant (W m^{-2} K^{-4}). The term on the left hand side describes the heat conduction. The first term on the right hand side describes the heat convection to the particle from the surrounding gas, and the second term describes the radiative heat transfer between the wall and the particle. As a result of the measurements, both the gas and wall temperature profiles were known. The heat conductivity inside the particle was assumed to be a constant value of 0.1 W m^{-1} K^{-1}. This term included both the conduction of the char itself as well as the effect of the gas conductivity and radiation in the particle pores. The heat transfer coefficient was calculated with the Ranz and Marshall [17] correlation that is widely used in combustion-related literature. The emissivity of the particle in the radiation stage was set to be 0.9 as proposed by [18]. The heat capacity of the DAF material in the particle was modeled according to Merrick [19]:

$$c_{p,DAF} = \frac{R_u}{M_{ave}}\left[\left(\frac{T_{E1}}{T_p}\right)^2 \frac{e^{T_{E1}/T_p}}{\left(e^{T_{E1}/T_p} - 1\right)^2} + 2\left(\frac{T_{E2}}{T_p}\right)^2 \frac{e^{T_{E2}/T_p}}{\left(e^{T_{E2}/T_p} - 1\right)^2}\right], \tag{3}$$

where M_{ave} is the average molar mass of the elements in the DAF matter (kg^{-1} mol) and T_{E1} and T_{E2} are the Einstein temperatures (K). Merrick's model uses the Einstein form of quantum theory to describe the dependence of specific heat on temperature. The effect of the substance composition is considered by assuming that all the atoms in solid matter oscillate independently in three dimensions. This oscillation occurs with a common characteristic frequency. The mean atomic vibration is described in the model with the Einstein temperatures. The Einstein temperatures selected for the heat capacity calculation were 380 K and 1800 K. The heat capacity for the ash was calculated as follows:

$$c_{ash} = 754 + 0.586 T_p \tag{4}$$

The Stefan flow term θ in the convection term of the energy balance equation was used as presented in [20]. The following correlation applies to the Reynolds numbers up to 400 [20]:

$$\theta = e^{(-0.6B)}, \tag{5}$$

where B is related to the total gas release from a particle (–):

$$B = \frac{c_{gas}}{2\pi d_p k_g}\left(\frac{dm_p}{dt}\right) \quad (6)$$

In the equation above c_{gas} is the heat capacity of the product gas (J kg^{-1} K^{-1}), m_p is the mass of the particle (kg), d_p is the particle diameter (m), and k_g is the conductivity of the gas (W m^{-1} K^{-1}).

3.2. Mass loss chemical kinetics

The mass loss chemical kinetics of the char samples was modeled with two char oxidation reactions: reaction 1: $C + O_2 \rightarrow CO_2$, and reaction 2: $C + \frac{1}{2}O_2 \rightarrow CO$. The effect of the CO_2 gasification reaction was tested afterwards, thus, reaction 3: $C + CO_2 \rightarrow 2CO$. The general model that can be used to predict the reaction rate of the oxidation reactions can be written as [21]:

$$\dot{R}'' = k_c\left(C_{O_2}\right)^n, \quad (7)$$

where $\dot{R}''$ is the reaction rate (mol s^{-1} m^{-2}), k_c is the reaction rate coefficient (m s^{-1}), C_{O_2} is the concentration of oxygen (mol m^{-3}), and n is the reaction order. A similar approach can be used for the CO_2 gasification reaction rate. In this study the apparent reaction rate of the char particle $\dot{r}$ (kg s^{-1}) consisted of the three aforementioned reactions and was formulated as follows:

$$\dot{r} = \sum_{i=1}^{3}\dot{R}''_{c,i}(1 - X_{DAF})^s A_p M_C, \quad (8)$$

where

$$\dot{R}''_{c,i} = k_{c,i}\left(C_g\right)^{n_i}, \quad (9)$$

where the subscript i refers to reactions 1, 2 and 3, $\dot{r}_{c,i}$ is the reaction rate at which carbon is consumed (mol s^{-1} m^{-2}), $C_{g,s}$ is the concentration of the reacting gas (mol m^{-3}), M_C is the molar mass of carbon (kg mol^{-1}), A_p is the apparent reactive surface area (m^2), X_{DAF} is the dry ash-free carbon conversion (–), and s describes the apparent surface area's dependance of the particle conversion. The term $(1 - X_{DAF})^s A_p$ described how the reactive surface area evolved as the conversion advanced. The reaction order n_i was defined based on the global reactions 1, 2 and 3. The obtained values were 1, 0.5, and 1. The reaction rate coefficient $k_{c,i}$ was of the Arrhenius form [21]:

$$k_{c,i} = A_i e^{\left(-\frac{E_{a,i}}{R_u T_p}\right)}, \quad (10)$$

where A is the pre-exponential factor of the reaction rate coefficient (m s^{-1}), E_a is the exponential factor of the reaction rate coefficient (J mol^{-1}), R_u is the universal gas constant (J mol^{-1} K^{-1}), and T_p is the particle temperature (K). The kinetic parameters describe the apparent reaction rate of the particles and include the effect of internal gas diffusion.

3.3. Gas diffusion

The mass transfer processes of a combusting spherical particle can be described with the following equation:

$$\frac{\partial C}{\partial t} = \frac{1}{r^2}\left(\frac{\partial}{\partial r} r^2 D \frac{\partial C}{\partial r}\right) + \dot{C}, \quad (11)$$

where C is the gas concentration (mol m^{-3}), r is the radius (m), and the last term $\dot{C}$ describes the consumption of the diffusing gas species due to chemical reactions (mol m^{-3} s^{-1}). The boundary condition on the particle surface can be calculated with the help of gas film diffusion theory. A common approach to model gas film diffusion is to use a simple, integrated form of Fick's Law [21]:

$$\dot{N}''_{gas} = k_d\left(C_{gas,\infty} - C_{gas,s}\right), \quad (12)$$

where $\dot{N}''_{gas}$ is the molar flow of gas through a surface (mol s^{-1} m^{-2}), $C_{gas,\infty}$ is the concentration of the gas outside the boundary layer, and $C_{gas,s}$ is the gas concentration on the particle surface. The concentration of the boundary layer was calculated at the average temperature of the bulk gas and the particle surface. The mass transfer coefficient k_d (m s^{-1}) was calculated from the Ranz Marshall correlation expressing the Sherwood number as a function of the Reynolds and Schmidt numbers. The diffusion coefficient was calculated according to [22]:

$$D_{AB} = \frac{266T^{\frac{3}{2}}}{p(M_{AB})^{\frac{1}{2}}\sigma_{AB}^2\Omega_D} \quad (13)$$

where D_{AB} is the diffusion coefficient (cm^2 s^{-1}), T is the temperature (K), p is the pressure (Pa), σ_{AB} is the characteristic length (Å), and Ω_D is a diffusion collision integral (–). The term M_{AB} can be written as:

$$M_{AB} = 2\left[\frac{1}{M_A} + \frac{1}{M_B}\right]^{-1}, \quad (14)$$

where M_A and M_B are the molecular weights (g mol^{-1}) of gases A and B.

Inside the particle the diffusion phenomenon of the reacting gas consists of Knudsen diffusion and molecular diffusion. If the pores of the particle are small, Knudsen diffusion becomes the dominant factor. There are various methods to model gas diffusion inside a combusting char particle. However, since there was no measurement data on the pore diameter or the reactive surface area evolution during the combustion process, the internal diffusion could not be modeled accurately. Therefore, Eqs. (11) and (12) were used to calculate the reacting gas concentration on the particle surface and inside each particle core while assuming that the diffusion inside the particle was infinitely fast. As a result of this approach, the calculated kinetic parameters describe only the apparent combustion process of the particles.

3.4. Particle diameter evolution

The diameter evolution for char 1 and char 2 particles during pyrolysis was modeled with the following equation [23]:

$$d = d_0(1 - X)^{\beta}, \quad (15)$$

where d is the diameter of the particle (m) at a given time, and d_0 is the particle initial diameter (m). If the term β is 0, the particle diameter remains constant and its density decreases during pyrolysis, which represents the shrinking core model. The maximum value of 1/3 for β describes a situation where the density remains constant and the diameter decreases, which represents the shrinking particle model. Calculating the kinetic parameters and the other modeling was performed with particles consisting of 50 cores, all of which had the same volume in the beginning. All the cores had different temperature histories, and thus different reaction rates. Therefore, instead of using Eq. (15), the diameter of the particle was calculated according to the volume change of each individual core. The volume change equation could be written as:

$$V_e = V_{e,0}(1 - X)^{3\beta}, \quad (16)$$

where V_e is the volume of the element, $V_{e,0}$ is the initial volume of the element, and X is the element mass loss in dry form.

3.5. Discretizing the particle size distribution

The particle size distribution was calculated for the initial samples according to the analyzed diameter data. The distribution was discretized into ten equal-sized volume fractions. After this, the volume mean diameter of each fraction was calculated. The

obtained volume mean diameters were then used as initial diameters in the model calculations. Thus, the model results were volume-averaged. The averaging was done as follows:

$$F_{avg} = \sum_{n=1}^{10} F_n v_n, \quad (17)$$

where F_{avg} is the averaged variable (X, T_p, c_p, or d_p), F_n is a variable (X_n, $T_{p,n}$, $c_{p,n}$, or $d_{p,n}$) related to the n:th volume fraction, and $v_n = 0.1$ is the volume fraction. This results from the different heating rates. With smaller particles the heating rate was higher and the temperature in the particles increased more rapidly. In the modeling calculations only the temperature of the particle surface core was compared to the measurements. Due to the small particle size, their terminal velocity was small compared to the gas velocity. Thus, the velocity of the particles in the reactor was assumed to be the same regardless of the particle size. Therefore, there was no difference in the residence times between different volume fractions.

3.6. The objective function and the optimization routine

A MATLAB-based objective function was created to determine the kinetic parameters of the chosen reactions. The objective function minimized the square error between the mass loss, particle surface temperature, and diameter model predictions between the measured values. The optimization routine used MATLAB's fminsearch function. The errors from the mass loss, particle surface temperature, and diameter comparisons were summed in such a manner that the mass loss and temperature error were emphasized more than the diameter error. This was done because of the greater variance in the diameter measurements and because the mass loss and temperature were of greater importance when determining the chemical kinetic parameters. A lower limit of 10 kJ mol^{-1} was set for the exponential factors of the reaction rate coefficients. Another limitation in the optimization routine was that the reaction rate coefficient on the reaction forming CO had to be higher than that of the reaction forming CO_2 at high temperatures. The kinetic parameters were optimized from all the four N_2/O_2 concentration setups for both fuels. However, due to difficulties in modeling, the mass loss at the two lower O_2 concentration cases were emphasized three fold compared to the two lower ones. The fminsearch algorithm had a tendency to find only local minimums of the error function. Therefore, multiple initial guesses were introduced in order to determine the kinetic parameters.

4. Results and discussion

4.1. Replacing N_2 with CO_2

This subsection presents the mass loss, diameter, and particle surface temperatures of the char samples measured in the DTR in the N_2/O_2 and CO_2/O_2 atmospheres, as well as the numerical modeling results. The chemical kinetic parameters of the char oxidation reactions were determined with the optimization routine from the measurements in N_2/O_2. The CO_2/O_2 model calculations were conducted with the same kinetic parameters. Hence, the difference in the model prediction between the N_2/O_2 and CO_2/O_2 atmospheres originates solely from the difference between the gas thermal properties and diffusivities. With this procedure it was possible to examine if the high concentration of CO_2 had an influence on the oxidation reaction kinetics.

The oxygen concentration clearly had a strong effect on the carbon conversion rate, as can be seen from Fig. 3. With 8 vol.% of oxygen the carbon conversion reached 100% at approximately 1.65 s. A notable fact is that especially with 2 and 3 vol.% of oxygen, the reactions consuming carbon begin with a significant delay compared to the model prediction. This ignition delay might have been caused by, for example, impurities adsorbed to the char surface during storage or when the sample was inserted to the feeder, which is when the sample was exposed to the ambient air.

Fig. 3 shows that an ignition delay also occurs in the CO_2 atmosphere. With 67.5 cm heating length in the CO_2 and O_2 mixture, the particle flow spread to such an extent that the particles were colliding to the reactor wall, which is why the final conversion values of the measurements in CO_2 had to be left out of consideration. They are not shown in the figures. A similar spreading phenomenon was not noticed in the N_2 and O_2 mixture, which might be the result of differences in the gas viscosities. Replacing N_2 from the DTR atmosphere with CO_2 seemed to delay the carbon conversion, especially with the highest O_2 concentrations. The CO_2/O_2 model predictions were calculated with the same chemical kinetic parameters obtained from the optimization program. While comparing the differences in the mass loss and also in the temperature figures, it is necessary to take into account the different temperature histories of the char particles between the N_2/O_2 and CO_2/O_2 atmospheres, which are caused by the different particle velocities. The model result seemed to be rather accurate at the two higher oxygen concentrations, but since there was no element in the model that would consider the ignition delay, the two lower concentration predictions were not so successful. Khatami et al. [24] concluded in their article that the burnout times of coal particles in N_2/O_2 atmospheres were faster than the corresponding times in CO_2/O_2. The oxygen concentrations used in their work were higher than those used in this study. Nevertheless, the same behavior regarding the burnout times could be seen in Fig. 3 with the two higher oxygen concentrations.

For char 2 the oxygen concentrations used in the measurements were 3, 6, 10, and 12 vol.%. The dry ash-free mass loss values and the modeling results of the char 2 combustion measurements are presented in Fig. 4.

The mass loss rate of char 2 was significantly lower than that of the char 1 sample. Even with the 12 vol.% of O_2 the total ash-free mass loss was not even close to 100% in the final section of the reactor, as was noted with char 1. A similar ignition delay as in the N_2 could be noted especially with lower O_2 concentrations. Shaddix and Molina [25,26] stated in their articles that the presence of CO_2 delays single-particle coal ignition. Also Khatami et al. concluded in their article [27] that all of the coal samples they studied ignited later in O_2/CO_2 than O_2/N_2 atmospheres. Similar

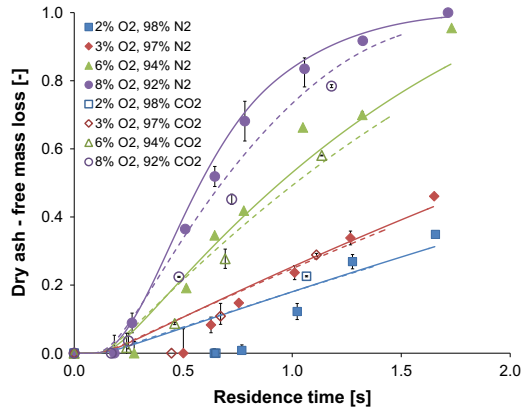

Fig. 3. The dry ash-free mass loss for char 1 as a function of residence time in the reactor.

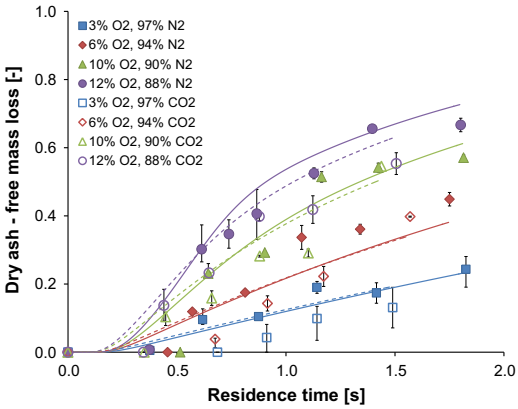

Fig. 4. The dry ash-free mass loss for char 2 as a function of residence time in the reactor.

phenomena can be observed with char 2 at 3 and 6 vol.% of oxygen. The time resolution at the higher oxygen concentrations is not sharp enough to allow any similar conclusions to be drawn. With char 2 the measured mass loss difference between the N_2/O_2 and CO_2/O_2 atmospheres was more clear than with char 1.

Figs. 5–8 show the measured and modeled particle surface temperatures. The lines represent the calculation results of each particle size discretized from diameter distribution. In the calculations a constant particle density was assumed. Therefore, according to the model, the smallest particles had the smallest amount of carbon to burn, and they were consumed by the oxidation reactions more rapidly. This approach did not take into account cenospheric particles. In the future it would be appropriate to develop the particle imaging system and analysis program to identify not only the outlines of the particle but also whether it is cenospheric or not. In this way, the model could consider two kinds of particles from which the other would be cenospheric.

In addition to the particle size the notable variation in the measured particle temperatures could also result from the differences in the scale of internal burning. According to Mitchell [28], with this approach the particles of the same size can vary in temperature and in overall burning rate per unit external area. The dots in the figures indicate the average of the measured values, and the error bars mark the standard deviation in the measurements. Fig. 5 shows that the oxygen concentration clearly had an effect on the particle surface temperatures. With char 1 a minor difference in the temperatures can be seen already at 0.2 s. The 2% and 3% oxygen concentrations behaved in a similar fashion, but especially with 8% concentration the temperature peak was much higher in comparison with the other measurements. The highest average temperature was approximately 1313 K.

Fig. 6 shows that the particle surface temperature decreased when replacing the N_2 with CO_2. Bejarando and Levendis [5] reported in their work that replacing N_2 with CO_2 reduced coal char surface temperatures as much as 200 K. Moreover, Shaddix and Molina [25] showed results on two coal sample combustion at 1700 K and 12 vol.% of O_2 in both N_2 and CO_2. The measured particle temperature drop during char combustion between the N_2 and CO_2 atmospheres was approximately 150 K. The temperature decrease can partly be explained with the difference in heat capacity and diffusivity between N_2 and CO_2. The boundary layer diffusion of oxygen to the particles is slower in CO_2 than in N_2. Furthermore, CO_2 in the boundary layer stores more energy.

The model calculations seem to agree well with the measured values in the N_2/O_2 setting in Fig. 5, and be higher than the measured values with the CO_2/O_2 setting in Fig. 6. This indicates that the differences in the char particle surface temperature measurements cannot be fully explained by differences in the gas thermal properties. This could be a result of the endothermic effect of the CO_2 gasification reaction. Another additional explanation for the temperature drop could be that CO_2 might have also blocked part of the reaction between oxygen and solid carbon by occupying the active sites on the char particle surface.

In the case of char 2, replacing N_2 with CO_2 resulted again in lower particle surface temperatures. With both chars, the calculated temperature in the CO_2 atmosphere seemed to increase more rapidly in the beginning. This can better be seen from the mass loss

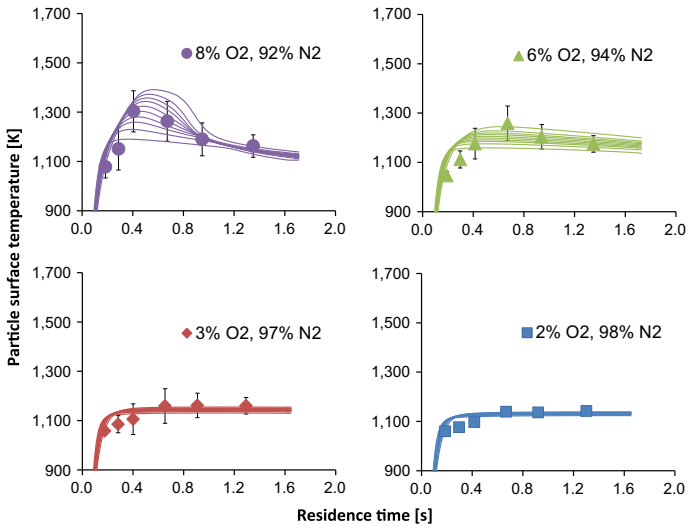

Fig. 5. The particle surface temperature for char 1 in O_2/N_2 atmosphere as a function of residence time in the reactor.

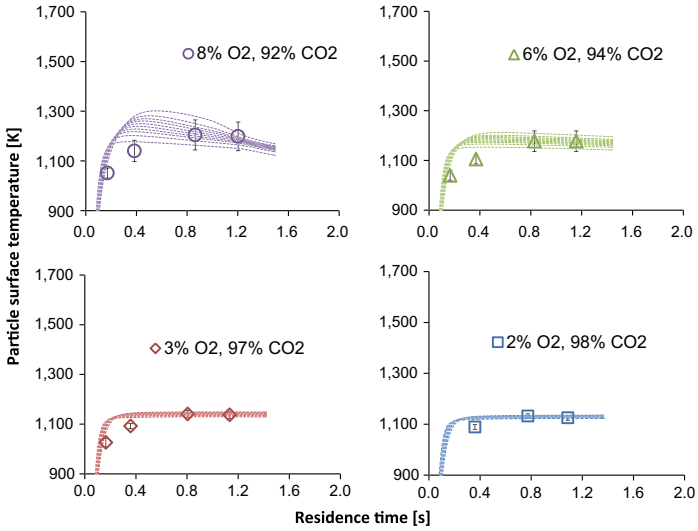

Fig. 6. The particle surface temperature for char 1 in O_2/CO_2 atmosphere as a function of residence time in the reactor.

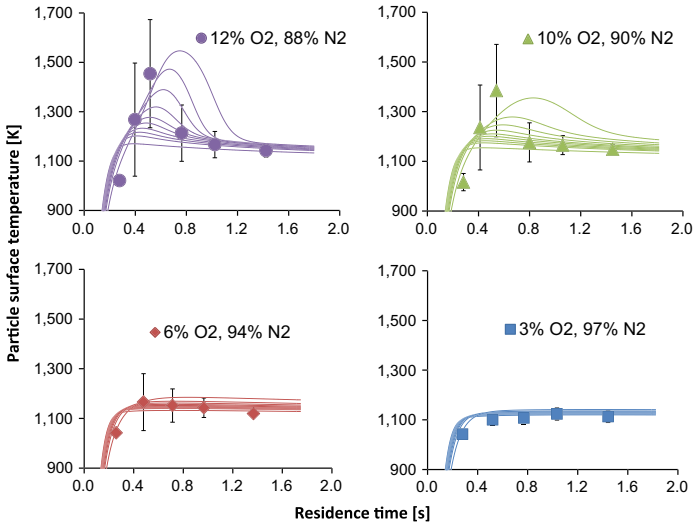

Fig. 7. The particle surface temperature for char 2 in O_2/N_2 atmosphere as a function of residence time in the reactor.

calculation results in Fig. 4 where the CO_2 atmosphere cases seem to be ahead of their N_2 counterpart in the beginning. This is caused by the higher velocity of the char particles compared to the N_2 atmosphere. The temperature profile in the first section of the reactor was shaped in the form of an asymptotic function. Higher particle velocity meant that the particles were subject to greater temperature difference. In Fig. 7 the model result of the particle surface temperature did not reach the measured values, and the temperature peak seemed to be delayed. This lower value and delay might, to some extent, result from the ignition delay at the beginning of the combustion process. If the ignition occurred later in the model calculations, the mass loss rate would have been more rapid, and the temperature would have peaked at a higher point.

According to Fig. 8, the measured temperatures at the end of the reactor were lower than the calculated ones. This could be caused by the endothermic effect of CO_2 gasification.

The measured particle surface temperatures and the particle size indicate that the combustion process of the particles took place within the Zone I and Zone II regime. Especially with the highest O_2 concentrations it would be reasonable to assume that the pore diffusion had some effect on the reaction rate.

The spherical equivalent diameters as functions of the dry ash-free mass loss measured from both atmospheres and samples are presented in Fig. 9. The spherical equivalent diameter seemed to decrease sharply after the particles were inserted to the reactor, even though the mass of the particle did not decrease significantly.

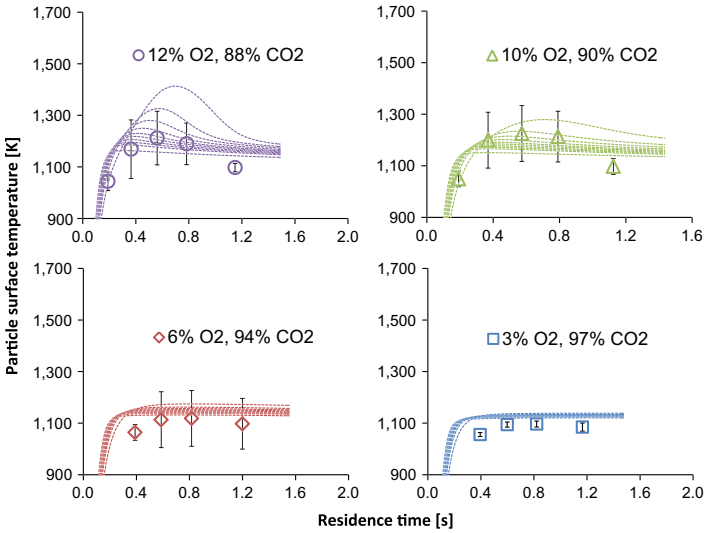

Fig. 8. The particle surface temperature for char 2 in O_2/CO_2 atmosphere as a function of residence time in the reactor.

This sudden drop in the measured diameters could result from partial fragmentation of the particles. However, this could not be visually observed in the reactor. Visual observation of the particles during the combustion process was conducted by removing the particle collecting system from underneath the DTR. The combusting particles could then be observed with a mirror from below while they were falling in the reactor. The mass loss could not be measured during these runs because the particles fell on top of the mirror. Nevertheless, a mere visual observation does not unambiguously remove the possibility of particle fragmentation. Jimenénez and Ballester [29] reported results of coal particle fragmentation in the early stages of combustion. They also emphasized the importance of taking into account the particle fragmentation and size distribution in numerical simulations. Ma and Mitchell [30] also reported that a large number of small fragments are generated during char oxidation. They concluded that taking the fragmentation into account would yield better predictions for particle size distribution.

4.2. Replacing N_2 gradually with CO_2

For char 2 the effect of replacing N_2 gradually with CO_2 was tested at a reactor temperature of 1123 K. The purpose of these tests was to find out if any interactions between the oxidation and the gasification reactions could be detected with the measurement setup. The oxygen concentration was kept at 12 vol.%. The measurements were complex and time-consuming which is why they were only conducted with char 2. The gas concentrations

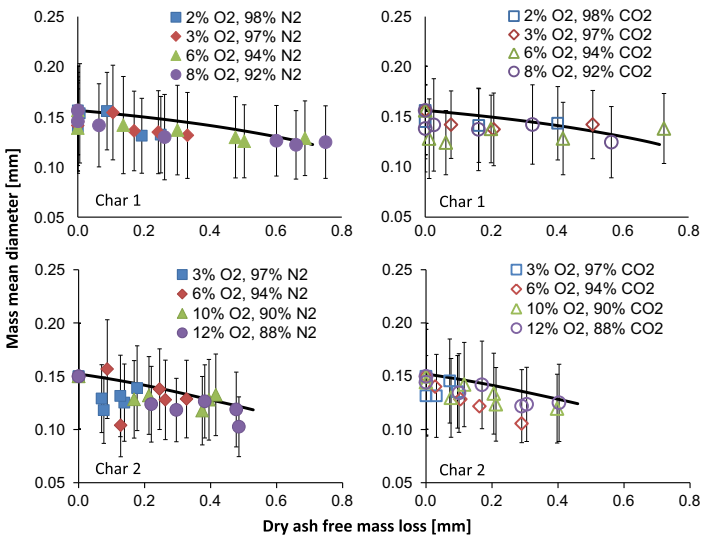

Fig. 9. The spherical equivalent mass mean diameter for char 1 and char 2 as a function of dry ash-free mass loss. The line represents the model fit.

can be seen from Fig. 10 legend. Fig. 10 shows that the conversion values of each set would form almost overlapping weight loss curves. Only the 12 vol.% O_2 and 88 vol.% of N_2 combination stood out as slightly higher.

The residence times of the mass loss and particle surface temperature points were calculated based on the pure N_2/O_2 and CO_2/O_2 setups. The particle surface temperature measurements seemed to follow the same trend than in the mass loss measurements: the pure N_2/O_2 case stood out from the rest. When 20 vol.% of N_2 was replaced with CO_2, the temperature drop was the highest. After further increasing the volume fraction of CO_2, the measured particle surface temperatures seemed to overlap each other. This can be seen from Fig. 11.

The effect of the CO_2 gasification reaction was excluded from the presented modeling results. Based on their results, Hecht et al. [6] stated that the CO_2 gasification reaction rate would be very minor compared to the char oxidation reaction at the temperatures measured in this study. However, the effect of the gasification reaction was examined by optimizing the pre-exponential and exponential parameters for the CO_2 gasification reaction-rate coefficient. The optimizations were conducted according to the measurement results presented in this subsection. Two cases are thus presented. In case 1 the mass loss and the particle surface temperature profiles are calculated with the optimized kinetic parameter for char 2. The differences in the results, as in the previous subsection, derive solely from the differences in the gas properties and velocities of falling particles in the reactor. Only the char oxidation reactions were examined. In case 2 the gasification reaction was activated, and the oxidation reactions were assumed to be independent from the gasification reaction. The modeling calculations were conducted with the same particle size distribution as presented for the char 2 sample. Fig. 12 shows the modeled dry ash-free mass loss and the particle surface temperatures of both cases. For clarification, only the average particle surface temperatures are shown in the charts.

The particle surface temperature in Fig. 12 appeared to increase more rapidly when the CO_2 concentration became higher. This was not only due to the higher specific heat capacity of CO_2 compared to N_2, but also because of the slightly different velocities of the particles between different gas atmospheres. Increased falling velocity meant higher temperature difference in the first section of the reactor. If the gasification reaction is assumed to take place without interfering with the oxidation reactions as in case 2, it seems that the temperature reduction resulting from increased CO_2 partial pressure is greater, and of the same magnitude, as in the measurements than without the gasification reaction. The mass loss prediction also seems to be more accurate: the mass loss is slightly reduced and the pure N_2/O_2 setting stands out more clearly. A third scenario, where the high concentration of CO_2 was assumed to block some of the oxidation reactions, was also tested. However, this approach led to less accurate predictions than in the second case. It appears that with the tested coal char the oxidation and gasification reactions affected the particle combustion process with little interference to one another. Moreover, the CO_2 gasification reaction seemed to have some significance. However, the accuracy and the number of the measurements is not adequate to unambiguously confirm these observations. Clearly, the matter requires more studying. Other possible explanations for the particle surface temperature reduction could be the change in the CO/CO_2 production ratio, or reduced homogenous CO oxidation due to high CO_2 concentration in the particle boundary layer.

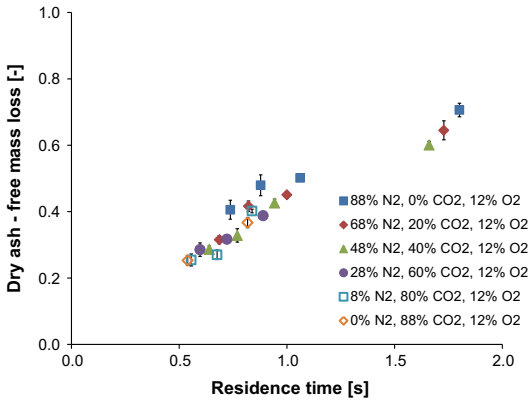

Fig. 10. The dry ash-free mass loss for char 2 as a function of residence time in the reactor. N_2 was gradually replaced with CO_2.

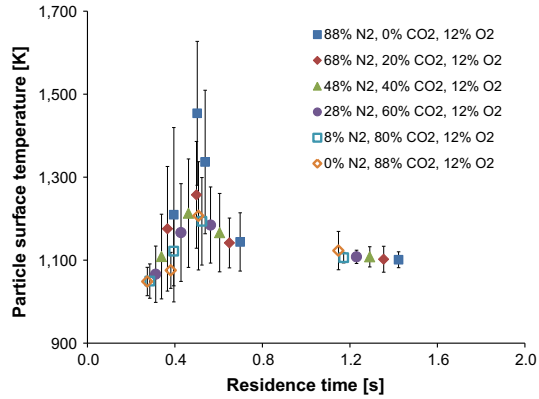

Fig. 11. The particle surface temperature for char 2 as a function of residence time in the reactor. N_2 was gradually replaced with CO_2.

4.3. Fitted parameters

The apparent kinetic parameters and the particle size evolution exponential factor, which were calculated on the basis of the N_2/O_2 measurement cases, are presented for both char samples in Table 2.

The subscripts 1 and 2 in the exponential and pre-exponential factors refer to the char oxidation reactions 1 and 2. Similarly, subscript 3 refers to the gasification reaction. Comparing the char parameters reveals that the size of the char 2 sample decreased according to the shrinking particle model, whereas in the case of char 1 the shrinkage was less significant. A notable difference is also in the term *s*, which was rather small for char 1. This would mean that the reaction rate was almost independent in the conversion phase, especially in the early stages of the combustion process. The gasification reaction kinetic parameters would indicate that the reaction 3 was very notable compared to the oxidation reactions. Moreover, the activation energy of the reaction seemed really low in comparison to the values suggested in [6,11]. However, the complexity of the reaction and diffusion phenomena especially in the particle boundary layer most likely reduce the accuracy of the calculated gasification parameters. Another possible reason for the low activation energy is that the gasification reaction was not as fast as the kinetic parameters indicated and reaction 3 in effect described the change in the oxidation reactions.

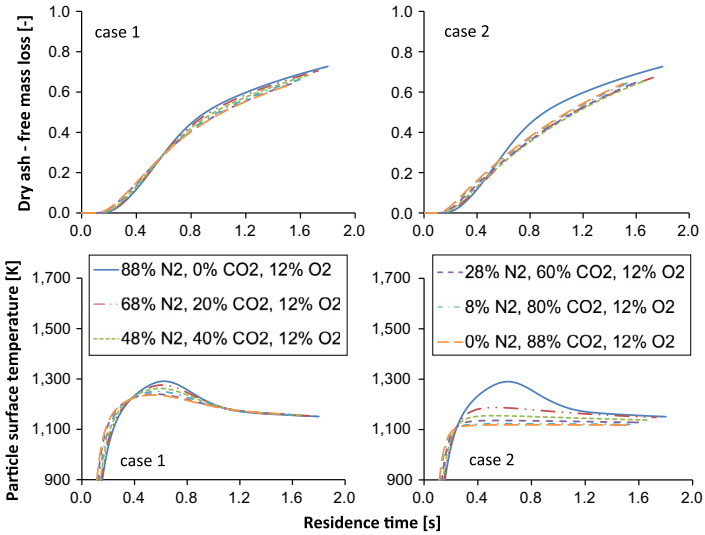

Fig. 12. Model calculations for the dry ash-free mass loss and particle surface temperature: examining the effect of the CO_2 gasification reaction. The legends apply for all separate charts.

Table 2
The kinetic parameters of the char oxidation and gasification reactions and the size evolution exponential factor.

Parameter	Char 1	Char 2	Unit
A_1	1915	846.9	m s^{-1}
$E_{a,1}$	80,105	76,600	J mol^{-1}
A_2	1284	853.2	m s^{-1}
$E_{a,2}$	82,490	81,570	J mol^{-1}
A_3	–	311.5	m s^{-1}
$E_{a,3}$	–	83,530	J mol^{-1}
m	0.119	0.465	–
β	0.197	0.333	–

5. Conclusion

In this study, char oxidation under high heating rates was tested with two coal char samples in a drop-tube reactor. The measurements were conducted in N_2/O_2 and CO_2/O_2 atmospheres, and the combustion was assumed to take place within the Zone I and Zone II regimes. The effect of high CO_2 concentration on the char combustion process in the case of both char samples was examined by replacing the N_2 entirely with CO_2. With char 2, replacing N_2 gradually with CO_2 was also tested. With both chars the change from N_2/O_2 to CO_2/O_2 atmospheres reduced the mass loss rate and the particle surface temperature. With the two lowest O_2 concentrations the ignition was delayed compared to the model prediction. This could have been caused by adsorption of impurities on the sample particle surface. In the case of char 2, at the two lowest O_2 concentrations, the CO_2 seemed to further delay the ignition. The numeric modeling indicated that taking into account the particle size distribution was an important factor when attempting to explain the wide range in the particle surface temperature measurements. Based on the comparison between modeling and measurement results, no clear interactions or competition could be detected between the gasification and oxidation reactions. Moreover, the gasification reaction appeared to be partially the reason for the particle surface temperature decrease when the CO_2 concentration was increased.

Acknowledgment

The authors gratefully acknowledge the financial support of Metso Co. and Fortum Co. for this study.

References

[1] Buhre B, Elliott L, Sheng C, Gupta R, Wall T. Oxy-fuel combustion technology for coal-fired power generation. Prog Energy Combust Sci 2005;31(4):283–307. http://dx.doi.org/10.1016/j.pecs.2005.07.001. ISSN 0360-1285. <http://www.sciencedirect.com/science/article/pii/S0360128505000225>.

[2] Chen L, Yong SZ, Ghoniem AF. Oxy-fuel combustion of pulverized coal: characterization, fundamentals, stabilization and CFD modeling. Prog Energy Combust Sci 2012;38(2):156–214. http://dx.doi.org/10.1016/j.pecs.2011.09.003. ISSN 0360-1285. <http://www.sciencedirect.com/science/article/pii/S0360128511000529>.

[3] Zhang L, Binner E, Qiao Y, Li C-Z. In situ diagnostics of Victorian brown coal combustion in O_2/N_2 and O_2/CO_2 mixtures in drop-tube furnace. Fuel 2010;89(10):2703–12. http://dx.doi.org/10.1016/j.fuel.2010.04.020. ISSN 0016-2361. <http://www.sciencedirect.com/science/article/pii/S0016236110001936>.

[4] Brix J, Jensen PA, Jensen AD. Coal devolatilization and char conversion under suspension fired conditions in O_2/N_2 and O_2/CO_2 atmospheres. Fuel 2010;89(11):3373–80. http://dx.doi.org/10.1016/j.fuel.2010.03.019. ISSN 0016-2361. <http://www.sciencedirect.com/science/article/pii/S0016236110001110>.

[5] Bejarano PA, Levendis YA. Single-coal-particle combustion in O_2/N_2 and O_2/CO_2 environments. Combust Flame 2008;153:270–87. http://dx.doi.org/10.1016/j.combustflame.2007.10.022. ISSN 0010-2180. <http://www.sciencedirect.com/science/article/pii/S0010218007003276>.

[6] Hecht ES, Shaddix CR, Molina A, Haynes BS. Effect of CO_2 gasification reaction on oxy-combustion of pulverized coal char. Proc Combust Inst 2011;33(2):1699–706. http://dx.doi.org/10.1016/j.proci.2010.07.087. ISSN 1540-7489. <http://www.sciencedirect.com/science/article/pii/S1540748910003718>.

[7] Senneca O, Cortese L. Kinetics of coal oxy-combustion by means of different experimental techniques. Fuel 2012;102(0):751–9. http://dx.doi.org/10.1016/j.fuel.2012.05.033. ISSN 0016-2361. [Special Section: {ACS} Clean Coal] <http://www.sciencedirect.com/science/article/pii/S0016236112003778>.

[8] Umemoto S, Kajitani S, Hara S. Modeling of coal char gasification in coexistence of CO_2 and H_2O considering sharing of active sites. Fuel 2013;103(0):14–21. http://dx.doi.org/10.1016/j.fuel.2011.11.030. ISSN 0016-2361. [Special Issue of The Second International Symposium on Gasification and its Application]<http://www.sciencedirect.com/science/article/pii/S0016236111007241>.

[9] Wang G, Zander R, Costa M. Oxy-fuel combustion characteristics of pulverized-coal in a drop tube furnace. Fuel 2014;115(0):452–60. http://dx.doi.org/10.1016/j.fuel.2013.07.063. ISSN 0016-2361. <http://www.sciencedirect.com/science/article/pii/S0016236113006625>.

[10] Maffei T, Khatami R, Pierucci S, Faravelli T, Ranzi E, Levendis YA. Experimental and modeling study of single coal particle combustion in O_2/N_2 and Oxy-fuel (O_2/CO_2) atmospheres. Combust Flame 2013;160(11):2559–72. http://dx.doi.org/10.1016/j.combustflame.2013.06.002. ISSN 0010-2180. <http://www.sciencedirect.com/science/article/pii/S0010218013002125>.

[11] Hecht ES, Shaddix CR, Geier M, Molina A, Haynes BS. Effect of CO_2 and steam gasification reactions on the oxy-combustion of pulverized coal char. Combust Flame 2012;159(11):3437–47. http://dx.doi.org/10.1016/j.combustflame.2012.06.009. ISSN 0010-2180. <http://www.sciencedirect.com/science/article/pii/S0010218012001897>.

[12] Tolvanen H, Kokko L, Raiko R. Fast pyrolysis of coal, peat, and torrefied wood: mass loss study with a drop-tube reactor, particle geometry analysis, and kinetics modeling. Fuel 2013;111(0):148–56. http://dx.doi.org/10.1016/j.fuel.2013.04.030. ISSN 0016-2361. <http://www.sciencedirect.com/science/article/pii/S0016236113003165>.

[13] Lewis AD. Sawdust pyrolysis and petroleum coke CO_2 gasification at high heat, master's thesis. Brigham Young University; 2011. p. 131–37.

[14] Honkanen M, Saarenrinne P, Stoor T, Niinimäki J. Recognition of highly overlapping ellipse-like bubble images. Meas Sci Technol 2005;16(9):1760–70. http://dx.doi.org/10.1088/0957-0233/16/9/007.

[15] Joutsenoja T. Pyrometric Thermometry and sizing of fuel particles in combustion, Ph.D. thesis. TTKK; 1998.

[16] Atkins PW. Physical chemistry. 6th ed. Oxford University Press; 1998. iSBN: 019850102.

[17] Ranz JWE, Marshall WR. Evaporation from drops, part II. Chem Eng Prog 1952;48:173–80.

[18] Solomon PR, Hamblen DG, Serio MA, Yu Z-Z, Charpenay S. A characterization method and model for predicting coal conversion behaviour. Fuel 1993;72(4):469–88. ISSN 0016-2361.

[19] Merrick D. Mathematical models of the thermal decomposition of coal: 2. Specific heats and heats of reaction. Fuel 1983;62(5):540–6. ISSN 0016-2361.

[20] Solomon PR, Serio MA, Suuberg EM. Coal pyrolysis: experiments, kinetic rates, and mechanisms. Progr Energy Combust Sci 1992;18:133–220.

[21] Laurendeau NM. Heterogeneous kinetics of coal char gasification and combustion. Progr Energy Combust Sci 1978;4:221–70.

[22] Reid RC, Prausnitz JM, Poling BE. The properties of gases & liquids. 4th ed. New York: McGraw-Hill, Inc; 1987.

[23] Smith IW. The combustion rates of coal chars: a review. In: 19th symposium (international) on combustion/the combustion institute; 1982. p. 1045–65.

[24] Khatami R, Stivers C, Joshi K, Levendis YA, Sarofim AF. Combustion behavior of single particles from three different coal ranks and from sugar cane bagasse in O_2/N_2 and O_2/CO_2 atmospheres. Combust Flame 2012;159(3):1253–71. http://dx.doi.org/10.1016/j.combustflame.2011.09.009. ISSN 0010-2180. <http://www.sciencedirect.com/science/article/pii/S001021801100294X>.

[25] Shaddix CR, Molina A. Particle imaging of ignition and devolatilization of pulverized coal during oxy-fuel combustion. Proc Combust Inst 2009;32(2):2091–8. http://dx.doi.org/10.1016/j.proci.2008.06.157. ISSN 1540-7489. <http://www.sciencedirect.com/science/article/pii/S1540748908002770>.

[26] Molina A, Shaddix CR. Ignition and devolatilization of pulverized bituminous coal particles during oxygen/carbon dioxide coal combustion. Proc Combust Inst 2007;31(2):1905–12. http://dx.doi.org/10.1016/j.proci.2006.08.102. ISSN 1540-7489. <http://www.sciencedirect.com/science/article/pii/S1540748906003658>.

[27] Khatami R, Stivers C, Levendis YA. Ignition characteristics of single coal particles from three different ranks in O_2/N_2 and O_2/CO_2 atmospheres. Combust Flame 2012;159(12):3554–68. http://dx.doi.org/10.1016/j.combustflame.2012.06.019. ISSN 0010-2180. <http://www.sciencedirect.com/science/article/pii/S001021801200199X>.

[28] Mitchell RE, kinetics-based An intrinsic. particle-population balance model for char oxidation during pulverized coal combustion. Proc Combust Inst 2000;28(2):2261–70. http://dx.doi.org/10.1016/S0082-0784(00)80636-0. ISSN 1540-7489. <http://www.sciencedirect.com/science/article/pii/S0082078400806360>.

[29] Jiménez S, Ballester J. Study of the evolution of particle size distributions and its effects on the oxidation of pulverized coal. Combust Flame 2007;151(3):482–94. http://dx.doi.org/10.1016/j.combustflame.2007.08.001. ISSN 0010-2180. <http://www.sciencedirect.com/science/article/pii/S0010218007001915>.

[30] Ma L, Mitchell R. Modeling char oxidation behavior under Zone II burning conditions at elevated pressures. Combust Flame 2009;156(1):37–50. http://dx.doi.org/10.1016/j.combustflame.2008.06.015. ISSN 0010-2180. <http://www.sciencedirect.com/science/article/pii/S001021800800285X>.

Publication IV

Tiina Keipi, Henrik Tolvanen, Lauri Kokko, Risto Raiko

The effect of torrefaction on the chlorine content and heating value of eight woody biomass samples

Biomass and Bioenergy, Volume 66, July 2014, Pages 232-239.

BIOMASS AND BIOENERGY 66 (2014) 232–239

Available online at www.sciencedirect.com

ScienceDirect

http://www.elsevier.com/locate/biombioe

The effect of torrefaction on the chlorine content and heating value of eight woody biomass samples

*Tiina Keipi**, *Henrik Tolvanen*, *Lauri Kokko*, *Risto Raiko*

Department of Chemistry and Bioengineering, Tampere University of Technology, Korkeakoulunkatu 1, 33720 Tampere, Finland

ARTICLE INFO

Article history:
Received 23 October 2013
Received in revised form
5 February 2014
Accepted 11 February 2014
Available online 12 March 2014

Keywords:
Torrefaction
Woody biomass
Chlorine reduction
Higher heating value
Energy yield

ABSTRACT

This study examined and compared the effect of torrefaction on the heating value, elementary composition, and chlorine content of eight woody biomasses. The biomass samples were torrefied in a specially constructed batch reactor at 260 °C for 30, 60, and 90 min. The original biomasses as well as the solid, liquid, and gaseous torrefaction reaction products were analyzed separately. The higher heating values (HHV) of dry samples increased from 19.5–21.0 MJ kg^{-1} to 21.2–23.2 MJ kg^{-1} during 60 min of torrefaction. In all samples, the HHV increased 9 % on average. Furthermore, the effect of torrefaction time on the biomass HHV was studied. Measurements showed that after a certain point, increasing the torrefaction time had no effect on the samples' HHV. This optimal torrefaction time varied considerably between the samples. For more reactive biomasses, i.e., birch and aspen, the optimal torrefaction time was close 30 min whereas the HHV of less reactive biomasses, e.g., stumps, increased markedly even after a 60-min torrefaction. Another significant observation was that torrefaction reduced the chlorine content of the biomass samples. The chlorine concentration of the solid product dropped in most samples from the original by half or even as much as 90 %. The highest relative chlorine decrease was observed in the *Eucalyptus dunnii* sample, which also had the highest chlorine content of all the studied biomasses. The relative carbon content of the biomass samples increased during torrefaction as the average elementary composition changed from $CH_{0.123}O_{0.827}$ to $CH_{0.105}O_{0.674}$ after a 60-min torrefaction.

1. Introduction

The growing world population and accelerating industrialization keep increasing the energy demand. The concurrent global warming and concerns about the depletion of fossil fuel reserves necessitate the development of sustainable ways to produce energy. Because biomass is considered a carbon-neutral source of energy, partial replacement of coal with biofuels in commercial combustion units lowers the carbon dioxide emissions [1]. However, biomass properties, such as heterogeneous and tenacious structure, hydrophilic nature, and high moisture content are posing challenges to using biomass for energy production.

Torrefaction, i.e., thermal treatment at temperatures ranging from 200 to 300 °C in the absence of oxygen, transforms biomass properties close to those of fossil coal [2,3]. Torrefaction increases biomass bulk density and improves its

* *Corresponding author*. Tel.: +358 400 899 364.
E-mail address: tiina.keipi@tut.fi (T. Keipi).
http://dx.doi.org/10.1016/j.biombioe.2014.02.015

storage and handling properties [4]. Furthermore, torrefaction reduces the biomass moisture content in two ways. First, increasing temperature evaporates the free water in biomass, and at above 200 °C releases the physically bound water [5]. Moreover, biomass loses partly its hydrophilic property as the hydroxyl groups decompose [1]. Torrefaction decreases the biomass oxygen content and increases the relative proportion of carbon, thus improving biomass fuel properties [2]. The vaporization of water and stripping of carbon dioxide (both with zero heating value) increase the biomass heating value. Even a 20-% increase in the biomass heating value during torrefaction has been observed [6]. Torrefaction has also shown to improve the grindability of biomass in terms of lowered energy demand and more spherical particles produced [7,8,9].

Arias et al. [10] have studied the effect of torrefaction on the reactivity and combustion properties of woody biomass and found out that torrefaction affects only to the most reactive hemicellulose components. Because of the low volatile content of torrefied biomass, the activation energy of the first stage of combustion increases [10]. Generally, hardwoods show better reactivity during torrefaction than softwoods because of their higher content of the most reactive hemicellulose component, i.e., glucuronoxylan, or xylan [6]. Compared to coal, the crucial problem in torrefied biomass use is its explosibility and higher flame speed referring to the ignition sensitivity of combustible dust and air mixture and the higher burning velocity of this powder, respectively [11].

This study focused on comparing the behavior of eight woody biomasses during torrefaction. Elementary analyses were conducted on the samples to better understand the changes in biomass during torrefaction. The effect of torrefaction on the biomass chlorine content was examined because fuel derived chlorine compounds may heavily corrode boilers [12,13,14,15] and in flue gas mitigate to the environment. Hydrogen chlorine (HCl) cause acidification [16] and dioxins are a risk to the human health because of their persistence, toxicity, and bio-accumulation resulted from their lipophilicity [17,18]. The effect of torrefaction on biomass chlorine content has not been studied commonly; however, methyl chloride has been detected in the volatile torrefaction products [19]. The torrefaction device in this study is a batch reactor with a relatively large sample particle size and sample volume together with slow torrefaction. Kim et al. [20] and Na et al. [21] have reported similar experimental set-ups.

2. Experimental

2.1. Materials

The experiments were run with eight woody biomass samples shown in Table 1. The chosen Eucalyptus samples represent globally important wood species and the other biomass samples represent common wood species in Finland.

The biomasses have been chipped, or crushed in the case of stumps, as a part of wood processing and the sample chip

Table 1 – Biomass samples.

Sample	Euca d.	Euca g.	Birch	Aspen	Pine	Spruce	Residue	Stumps
Species	*Eucalyptus dunnii*	*Eucalyptus grandis*	*Betula pubescens*	*Populus tremula*	*Pinus sylvestris*	*Picea abies*	97% pine 3% birch	100% spruce
Type	Hardwood	Hardwood	Hardwood	Hardwood	Softwood	Softwood	Softwood	Softwood
Geographic location	Forestal oriental plantation, Uruguay	Forestal oriental plantation, Uruguay	South-East Finland	South-East Finland	South-East Finland	Eastern Finland	Finland	South-East Finland
Date sample obtained	Spring 2012	Spring 2012	15.6.2012	15.6.2012	Spring 2012	27.3.2012	28.3.2012	5.6.2012
Diameter of original cross-section	Not known	Not known	1–15 cm	1–15 cm	15–30 cm	–	<7 cm	–
Age	9–11 years	9–11 years	Not known	Not known	70–80 years (final felling)	Not known	30–40 years (first thinning)	60–70 years
Storage conditions before sampling	Shipped in a container to Finland	Shipped in a container to Finland	Outdoors	Outdoors	Not known	In forest	In forest	In forest
Content	Stem wood	Stem wood	Stem wood, sticks, bark	Stem wood, sticks, bark	Stem wood from surface, no bark	Logging waste	Stem wood, bark, pine needles	Roots, foreign matter (soil, stones)
Maximum chip dimension	4 cm	4 cm	15 cm (sticks)	15 cm (sticks)	8 cm	12 cm	12 cm	12 cm
Moisture content, % (mass fraction)	31.8	39.5	31.7	47.1	51.4	57.2	48.2	44.8

size varied considerably. The dimensions shown in Table 1 are the maximum dimensions of each chipped species.

The samples were received as rough-grained. Thus, no further crushing was needed and those were used as such in the experiments. Using rough-grained particles is a realistic choice also in large-scale torrefaction applications because the better grindability achieved by torrefaction can then be utilized by crushing the fuel after torrefaction.

After receiving, a sample from each wood species was taken and stored in a freezer to retain its original moisture content until analysis. The remaining samples were dried to prevent molding during storage. Before experiments, each sample was oven-dried at 105 °C according to the European standard EN 14774-3 [22] to remove the moisture.

2.2. Test rig

The experiment system shown in Fig. 1 was constructed especially for this project at Tampere University of Technology (TUT). The torrefaction system consisted of an electrically heated oven, a reactor vessel made of stainless steel, and a product gas separation unit. The oven had a heating power of 9 kW and was pre-heated to the selected torrefaction temperature before each experiment. The stainless steel reactor vessel was a cylindrical with an outside diameter of 22 cm and a length of 31 cm. The cover of the reactor vessel was sealed with a graphite gasket and closed with a dense screw fastening. Because of the relatively large sample size, a heater, a coil of steel pipe with closed hot air circulation, was placed inside the reactor vessel to increase the sample heating rate.

At the beginning of each measurement run, the reactor vessel was filled with a sample and placed inside the oven. The gaseous product separation unit was then connected. The reactor vessel and pipeline connections were flushed with nitrogen to ensure inert conditions. A continuous nitrogen flow reported in most torrefaction studies was not used. This enabled collecting the undiluted gaseous reaction products in separate foil bags and analyzing the gas compositions later with FTIR.

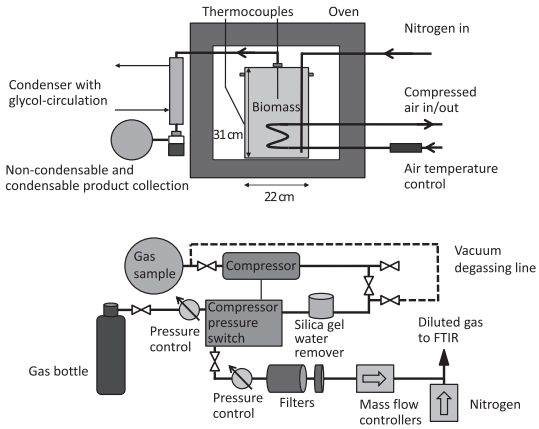

Fig. 1 – Torrefaction test rig above and the gaseous reaction product pressurization system below.

Attempts were made to construct a closed setup; however, some gaseous leakage may have occurred. The solid, liquid, and gaseous products were separated from each other during torrefaction. Therefore, it was possible to weigh the separate fractions afterwards and calculate the mass balance for those. The volatile products were separated into condensable and non-condensable fractions in a counterflow condenser with a closed glycol circulation. The condensable fraction of the volatile product was collected into glass bottles immersed in ice water and the non-condensable fraction in the foil bags. The solid reaction product remained in the reactor vessel.

One thermocouple was used to measure the sample's inner temperature at one-second intervals whereas another thermocouple was placed on the reactor side to control the oven temperature. The temperature of the air circulating inside the heater was controlled manually by measuring the temperature of the in flowing air. When a sample reached the targeted 260 °C, the timing began. The sample middle point temperature was chosen to be a constant; however, it oscillated around 260 °C, varying from 257 to 269 °C because of the coarse system control. Furthermore, because of the relatively large sample size, the temperature perhaps fluctuated at the other parts of the reactor vessel even more than was measured.

Quenching the solid residue started upon reaching the torrefaction time by turning off the oven, opening its cover, and switching the heater air circulation from hot to cold. After quenching, all parts of the closed reaction system were weighed for mass balance calculations and all fractions stored until further analysis.

2.3. Equations

The mass and energy yields describe how much of the original sample mass and energy content remain in the solid torrefaction product. The mass yield y_M is defined as

$$y_M = \left(\frac{m_{product}}{m_{feed}}\right)_{dry} \quad (1)$$

where $m_{product}$ is the mass (g) of the remaining torrefied biomass and m_{feed} is the feedstock initial mass (g), both measured as dry basis (dry). The energy yield is defined as

$$y_E = y_M\left(\frac{HHV_{product}}{HHV_{feed}}\right)_{dry} \quad (2)$$

where $HHV_{product}$ and HHV_{feed} are the higher heating values (MJ kg^{-1}) of torrefied biomass and initial feedstock (dry basis), respectively [23,24].

2.4. Experiments

This study focused on the effect of torrefaction on the elemental composition and fuel properties of woody biomasses. Furthermore, the effect of torrefaction time on mass and energy yields was studied. Two torrefaction times were used for each sample. All the samples were torrefied at 260 °C for 60 min, and the second torrefaction time depended on the relative reactivity in the first experiments. The more reactive samples, i.e., those with a high mass loss, were torrefied for

30 min and the less reactive samples, i.e., those with a little mass loss, for 90 min.

Because wood is a poor conductor of heat, it took relatively long for temperature to rise in a sample, despite the preheated oven and the internal heat source. Attempts were made to maintain the rise from room temperature to torrefaction temperature uniform in time, but it varied between 62 and 81 min. The sample volume too was chosen constant, but because sample bulk densities varied, so did the masses between 800 and 1600 g.

2.5. *Analyses*

Solid, liquid, and gaseous reaction products were analyzed separately. The solid materials were analyzed by Enas Co. The analyses were run on both the original biomass samples and the solid reaction products of 60-min torrefaction. These analyses comprised ultimate and proximate analyses, ash melting behavior, bulk density, and the concentrations of following the metals: sodium, potassium, calcium, magnesium, silicon, phosphorus, iron, aluminum, and titanium, and the following heavy metals: cadmium, thallium, mercury, antimony, arsenic, chromium, cobalt, copper, manganese, nickel, vanadium, lead, tin, and zinc. Furthermore, the samples were fractionated with water, acetate, and hydrochloric acid to determine the solubility of sodium, potassium, calcium, magnesium, silicon, phosphorus, iron, aluminum, titanium, manganese, and chlorine in them. The reaction products from 30- and 90-min torrefaction were analyzed only for higher and lower heating values. The analyses were not replicated.

The gaseous reaction products were analyzed at TUT. The qualitative and quantitative content of gases were measured with a Gasmet DX4000 Fourier transform infrared spectroscopy (FTIR) analyzer. Before analysis, liquid impurities were filtered out from gas samples, and the gas was pressurized and diluted with gaseous nitrogen (the gas pre-treatment system is shown in Fig. 1). Because the FTIR analyzer does not detect biatomic homonuclear molecules, e.g., nitrogen, gas content could not be directly measured; instead, it was iterated by the least square method.

The chlorine content of the selected liquid products was analyzed by the Institute for Environmental Research at University of Jyvaskyla.

3. Results and discussion

3.1. *Chlorine content and liquid products*

The most significant experimental result was that the biomass chlorine content decreased during torrefaction. The elementary chlorine content (Fig. 2) dropped markedly in nearly all samples during a 60-min torrefaction, except for the pine sample, which retained its initial chlorine concentration. However, this chlorine concentration was the lowest of all the samples and linked perhaps to the low bark content in the pine sample. The greatest relative decreases in chlorine concentrations were measured for both eucalyptus samples, which originally had the highest chlorine content of all the

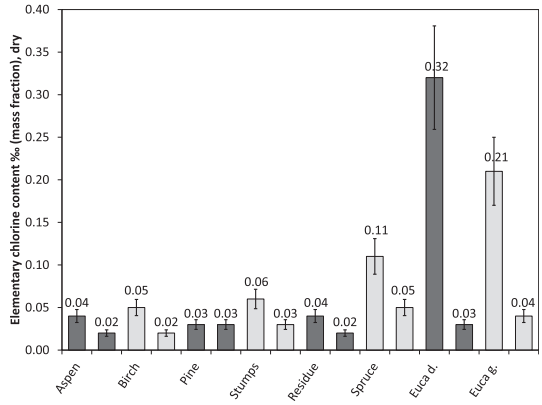

Fig. 2 – The elementary chlorine content of the original samples (left columns) and the solid products of a 60-min torrefaction (right columns).

samples. Torrefaction reduced as much as 90 % of the initial chlorine in the *Eucalyptus dunnii* sample.

It is not commonly known how chlorine is bound in biomass [25] but it can be largely extracted from various biomasses by leaching with water [26,27]. According to the conducted fractionation analyses, chlorine in experimented biomass samples was mostly in water soluble form, e.g., in original Eucalyptus samples over 95 %. Biomass chlorine reduction in pyrolysis has been frequently studied in connection with alkali release [25,28].

Dioxins, the general name of polychlorinated dibenzodioxins (PCDDs) and dibenzofurans (PCDFs), are generally formed according to the following general reaction equation [29]

$$Cl_2 + \text{organic molecules} \rightarrow \text{chlorinated molecules (e.g. PCDD/Fs)} \quad (3)$$

The formation of PCDDs and PCDFs is the most efficient at temperatures around 300 °C [30]. Molecular chlorine needed in the reaction (3) can be formed through the known Deacon reaction [31]

$$4HCl + O_2 \rightarrow 2H_2O + 2Cl_2 \quad (4)$$

which can be catalyzed by elemental copper or certain copper components [29,31]. The elementary copper content in the original experimented wood samples was between 0.73 and 3.6 mg kg^{-1} of dry sample.

Sulfur has been detected to inhibit dioxin formation by reducing both the Cl_2 levels and copper-catalyst levels [31,32]

$$SO_2 + Cl_2 + H_2O \leftrightarrow SO_3 + 2HCl \quad (5)$$

$$CuO + SO_2 + \frac{1}{2}O_2 \leftrightarrow CuSO_4 \quad (6)$$

The thermodynamic equilibrium constants of the reaction (5) for the temperature range of 0–900 °C in Ref. [31] reveal that the reaction towards the products is favored at lower temperatures. However, the low amount of sulfur present in the

experimented samples, at maximum 0.04 % of the dry sample mass, considerably limits the reactions (5) and (6). In general, the fuel molar ratio between sulfur and chlorine higher than 4 indicates low risk and less than 2 high risk of corrosion in a boiler [14]. In reference to this, the analysis results indicated a high risk of corrosion for both original Eucalyptus samples. On the contrary, after torrefaction all the experimented samples had a low risk of corrosion.

Björkman and Strömberg [16] have determined how four biomasses with relatively high chlorine content (0.18–0.79 % of total weight) lost chlorine 0–10 % and 3–23 % of the initial weight during pyrolysis at temperatures 200 and 300 °C, respectively. Jensen et al. [25] have reported 50 % release of total chlorine in straw between pyrolysis temperatures 200 and 300 °C and it is suggested in the article that at the temperature range of 200–400 °C the chlorine is released as HCl or potassium chloride (KCl).

The equations in this chapter describe the biomass chlorine reactions at experimented torrefaction temperatures. Based on these equations, it is reasonable to claim that torrefaction can theoretically affect to the biomass chlorine content. The presented results of other studies further support the chlorine reduction behavior of torrefaction.

The analysis of all the gaseous torrefaction products revealed only a hint of chlorine in the form of HCl. Therefore, four chosen liquid products were also analyzed. The literature reports various analyses of liquid torrefaction yield [6,8], yet chlorine content has not been measured in those studies. The chlorine content analyses were conducted for the liquid products of pine, spruce, euca d., and euca g. of 60-min torrefaction. The samples were selected because they represented extreme chlorine reduction behavior among the tested samples. In all reaction products, only pine registered the total measured chlorine as equivalent to that of its initial original sample. For the other samples, a significant proportion of the original chlorine content was not detected in the analyses of solid and liquid reaction products, as shown in Fig. 3.

The following may explain why all chlorine could not be detected. First, the methods used to analyze especially gaseous and liquid products may have been unsuitable for detecting all the possible chemical chlorine compounds. For example, the FTIR cannot discriminate chemical components from each other if the absorption spectrums of those components are overlapping. Second, sampling may have been selective due to the segregation of the gaseous and liquid products in the sampling containers. For example, some volatile compounds may have condensed on foil bag inner surfaces instead of in the liquid collection system. Third possibility is that during torrefaction some chlorine escaped from the system as gas. According to the United States Environmental Protection Agency [33] HCl has "an irritating, pungent odor", but during the experiments it was impossible to discriminate the odor of HCl from the dominant odor of tars.

3.2. *Heating value*

An important question in torrefaction research is how much the process can improve the heating value of biomass. In this study, the higher heating value (HHV) increased 9 % on average in all the samples. The HHV of the original biomasses were between 19.5 and 21.0 MJ kg^{-1} and after a 60-min torrefaction between 21.2 and 23.2 MJ kg^{-1}. The biomass specific heating value increased with torrefaction time, i.e., when the mass loss increased (the measured HHV of the original biomasses and the solid reaction products shown as a function of mass loss in Fig. 4 (upper points)). The uncertainty of the heating value analysis was reported as 1 %. The uncertainty of the O to C-ratio is not presented as the uncertainty of this analysis was not reported.

Clear differences were observed in reactivity between hardwoods and softwoods. The former, birch and aspen, reacted readily, producing lower mass yields and more volatiles than the latter. Consequently, torrefaction improved most the heating values of the hardwoods.

According to an accepted mass and energy balance for torrefaction, a solid torrefaction product contains 90 % of its

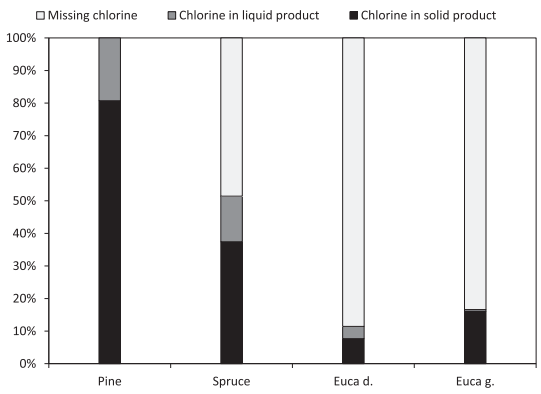

Fig. 3 – The proportions of detected chlorine in solid and liquid products of total chlorine content in selected original biomasses.

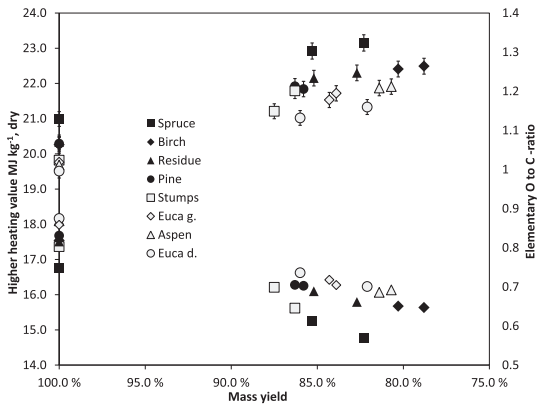

Fig. 4 – The biomass higher heating value (MJ kg^{-1}, dry) as a function of solid mass yield in torrefaction (upper points) and the biomass elementary O to C-ratio as a function of solid mass yield in torrefaction (lower points).

initial biomass energy but only 70 % of the initial mass; the ratio of energy to mass yield is thus 1.3 [34]. Such positive results were achieved neither in this study nor have they generally appeared in studies presented in literature [35]. In this study, the mass yield of a 60-min torrefaction varied from 78.8 to 87.5 % and the maximum ratio of energy to mass yield, i.e., 1.11, was measured for aspen and birch.

The heating values of the hardwoods, aspen and birch, were almost the same with both torrefaction times of 30 and 60 min. Therefore, for those biomasses the optimal torrefaction time was closer to 30 min. However, as far as the ratio of energy to mass yield is concerned, the less reactive stump sample benefited from longer torrefaction time. After a 90-min torrefaction, its HHV was 0.6 MJ kg^{-1} higher than after a 60-min torrefaction.

Moisture content is one important fuel property. The total moisture content of the original biomasses varied between 31.7 % and 57.2 % of the total mass. However, after torrefaction the moisture content was between 0.7 % and 1.8 %. The uncertainty of moisture content analysis was reportedly 5 %.

The fuel oxygen content is related to its combustion properties. The biomass elementary O to C-ratio decreased in torrefaction, as shown in Fig. 4 (lower points). The average elementary content of the biomass samples changed from $CH_{0.123}O_{0.827}$ to $CH_{0.105}O_{0.674}$ in the 60-min torrefaction, indicating an increase in the biomasses' relative carbon content. The uncertainty of C and H analysis was reportedly 1 % and 2 %, respectively. The decrease in the O to C-ratio results in an increase in the biomass heating value.

3.3. *Other fuel properties of the solid products*

The nitrogen and sulfur contents of the solid products were below those suggested by van Loo and Koppejan [12] to cause problems during industrial combustion. The biomass volatile content was analyzed according to the European standard EN 15148 [36]. In torrefaction, the volatile content of the samples decreased between 7 % and 10 %, yet the volatile content remained between 70 % and 80 % of the dry sample mass. This is higher than the coal values, 17–48 % [37]. The uncertainty of the volatile analysis was reportedly 1 %.

Ash melting behavior was analyzed for the original biomass samples and the solid products of the 60-min torrefaction. Four different temperatures were measured in an oxidative atmosphere: deformation temperature, sphere temperature, hemispherical temperature, and fluid temperature. The critical temperature descriptions are given in the literature [38]. According to the analysis results of the experimented biomasses, the critical temperatures of most samples were above the detection limit of 1450 °C. Therefore, the effect of torrefaction cannot be clearly observed. Nevertheless, the critical temperatures of experimented wood samples registered in the same range or even higher than those of coal [39,40]. There is no unambiguous relation between the ash melting behavior in analysis and in actual boiler; however, those have some connection [39]. Therefore, in co-combustion the reactions between different ashes can be detected only experimentally and even a small proportion of molten ash can cause problems in combustion.

According to the conducted experiments, torrefaction do not have any unambiguous influence on the biomass ash content. The ash contents of the original biomasses and solid products of a 60-min torrefaction were measured after burning the samples at 815 and 550 °C. The ash contents varied between 0.3 % and 4.0 % of the dry sample mass, which is again below the coal values, 6–28 % [19].

Torrefaction had no clear effect on the metals concentrations listed in Section 2.5, except for iron, whose concentration decreased in all samples. Bear in mind though that metal concentrations are not crucial in fuels; their chemical interreactions are the decisive factor. The above listed heavy metals concentrations were negligible compared to the reference values for coal [41], except for those of manganese. At all points, its concentration was almost same as or even higher than the coal reference values.

3.4. *Gaseous products*

The gaseous reaction product masses varied from 3.1 % to 5.4 % of the original sample masses. Here, the losses during torrefaction, 2.3–4.1 % of original sample masses, are assumed to be gaseous and are added up. According to the FTIR measurements, the average gas content was 79 % of carbon dioxide, 21 % of carbon monoxide, and a trace of methane. Variations between different samples were a few percentage points. The lower heating value of the gaseous products was a maximum of 2 kJ kg^{-1} or 3.3 kJ m^{-3} n, which is negligible compared, e.g., to methane (50 MJ kg^{-1} or 33 MJ m^{-3} n). Thus the combustion of the non-condensable torrefaction product alone is not profitable.

4. Conclusion

In torrefaction experiments with woody biomass samples, hardwoods and softwoods behaved differently. The hardwood samples were the most reactive as their energy densities increased most during torrefaction. The HHV of all the samples increased from 19.5–21.0 MJ kg^{-1} to 21.2–23.2 MJ kg^{-1} during a 60-min torrefaction at 260 °C. However, the energy densification of biomass by a factor of 1.3 that is commonly reported in the literature was not achieved. The highest achieved ratio of energy to mass yield was 1.11 for aspen and birch. Furthermore, the heating values of gaseous products were negligible.

The effect of torrefaction on biomass chlorine content has not been widely reported in the literature. It is presented in this study how the chlorine concentration of the experimented biomass samples dropped during torrefaction. The highest reduction in chlorine content, 90 %, was observed in the *E. dunnii* sample. The chemical reactions of chlorine at torrefaction temperatures are shown in chapter 3.1. Chlorine in biomass is theoretically reactive at torrefaction temperatures; however, better analytical methods are required to experimentally determine this phenomenon precisely.

Furthermore, torrefaction improved also other biomass properties. The elementary O to C-ratio decreased, indicating better combustion properties and the increase of heating value. The ash melting behavior of solid torrefaction products

was comparable with that of coal and the total ash content of solid products was well below the respective coal values. However, the behavior of ash in a solid torrefaction product during combustion must be studied experimentally.

Acknowledgments

The authors gratefully acknowledge the financial support of UPM Co.

REFERENCES

[1] Basu P. Biomass gasication and pyrolysis: practical design and theory. USA: Elsevier Inc.; 2010.
[2] van der Stelt MJC, Gerhauser H, Kiel JHA, Ptasinski KJ. Biomass upgrading by torrefaction for the production of biofuels: a review. Biomass Bioenergy 2011;35:3748–62.
[3] Bourgois J, Guyonnet R. Characterization and analysis of torrefied wood. Wood Sci Technol 1988;22:143–55.
[4] Wu MR, Schott DL, Lodewijks G. Physical properties of solid biomass. Biomass Bioenergy 2011;35:2093–105.
[5] Bergman PCA, Boersma AR, Zwart RWR, Kiel JHA. Torrefaction for biomass co-firing in existing coal-fired power stations "BIOCOAL". The Netherlands: The Energy research Centre of the Netherlands (ECN); 2005. Report No.: ECN-C-05–013.
[6] Prins MJ, Ptasinski KJ, Janssen FJJG. Torrefaction of wood: part 2. Analysis of products. J Anal Appl Pyrol 2006;77:35–40.
[7] Tolvanen H, Kokko L, Raiko R. Fast pyrolysis of coal, peat, and torrefied wood: mass loss study with a drop-tube reactor, particle geometry analysis, and kinetics modeling. Fuel 2013;111:148–56.
[8] Chen WH, Hsu HC, Lu KM, Lee WJ, Lin TC. Thermal pretreatment of wood (lauan) block by torrefaction and its influence on the properties of the biomass. Energy 2011;36:3012–21.
[9] Bergman PCA, Boersma AR, Kiel JHA, Prins MJ, Ptasinski KJ, Janssen FJJG. Torrefaction for entrained-flow gasification of biomass. The Netherlands: The Energy research Centre of the Netherlands (ECN); 2005. Report No.: ECN-C-05–067.
[10] Arias B, Pevida C, Fermoso J, Plaza MG, Rubiera F, Pis JJ. Influence of torrefaction on the grindability and reactivity of woody biomass. Fuel Process Technol 2008;89:169–75.
[11] Huéscar Medina C, Phylaktou HN, Sattar H, Andrews GE, Gibbs BM. The development of an experimental method for the determination of the minimum explosible concentration of biomass powders. Biomass Bioenergy 2013;53:95–104.
[12] van Loo S, Koppejan J. The handbook of biomass combustion and co-firing. USA: Earthscan; 2008.
[13] Antunes RA, de Oliveira MCL. Corrosion in biomass combustion; A materials selection analysis and its interaction with corrosion mechanisms and mitigation strategies. Corros Sci 2013;76:6–26.
[14] Miltner A, Beckmann G, Friedl A. Preventing the chlorine-induced high temperature corrosion in power boilers without loss of electrical efficiency in steam cycles. Appl Therm Eng 2006;26:2005–11.
[15] Uusitalo MA, Vuoristo PMJ, Mäntylä TA. High temperature corrosion of coatings and boiler steels below chlorine-containing salt deposits. Corros Sci 2004;46:1311–31.
[16] Björkman E, Strömberg B. Release of chlorine from biomass at pyrolysis and gasification conditions. Energy Fuel 1997;11:1026–32.
[17] Lavric ED, Konnov AA, De Ruyck J. Dioxin levels in wood combustion – a review. Biomass Bioenergy 2004;26:115–45.
[18] Pluim HJ, van der Goot M, Olie K, van der Slikke JW, Koppe JG. Missing effects of background dioxin exposure on development of breast-fed infants during the first half year of life. Chemosphere 1996;33:1307–15.
[19] Shang L, Ahrenfeldt J, Holm J, Barsberg S, Zhang R, Luo Y, et al. Intrinsic kinetics and devolatilization of wheat straw during torrefaction. J Anal Appl Pyrol 2013;100:145–52.
[20] Kim YH, Lee SM, Lee HW, Lee JW. Physical and chemical characteristics of products from the torrefaction of yellow poplar (Liriodendron tulipifera). Bioresour Technol 2012;116:120–5.
[21] Na BI, Kim YH, Lim WS, Lee SM, Lee HW, Lee JW. Torrefaction of oil palm mesocarp fiber and their effect on pelletizing. Biomass Bioenergy 2013;52:159–65.
[22] EN 14774-3 Solid biofuels – determination of moisture content – oven dry method – moisture in general analysis sample. Finland: The Finnish Standards Association (SFS); 2010.
[23] Sarvaramini A, Larachi F. Integrated biomass torrefaction – chemical looping combustion as a method to recover torrefaction volatiles energy. Fuel 2014;116:158–67.
[24] Bridgeman TG, Jones JM, Shield I, Williams PT. Torrefaction of reed canary grass, wheat straw and willow to enhance solid fuel qualities and combustion properties. Fuel 2008;87:844–56.
[25] Jensen PA, Frandsen FJ, Dam-Johansen K, Sander B. Experimental investigation of the transformation and release to gas phase of potassium and chlorine during straw pyrolysis. Energy Fuel 2000;14:1280–5.
[26] Dayton DC, Jenkins BM, Turn SQ, Bakker RR, Williams RB, Belle-Oudry D, et al. Release of inorganic constituents from leached biomass during thermal conversion. Energy Fuel 1999;13:860–70.
[27] Jenkins BM, Bakker RR, Wei JB. On the properties of washed straw. Biomass Bioenergy 1996;10:177–200.
[28] Olsson JG, Jäglid U, Pettersson JBC, Hald P. Alkali metal emission during pyrolysis of biomass. Energy Fuel 1997;11:779–84.
[29] Tuppurainen K, Halonen I, Ruokojärvi P, Tarhanen J, Ruuskanen J. Formation of PCDDs and PCDFs in municipal waste incineration and its inhibition mechanisms: a review. Chemosphere 1998;36:1493–511.
[30] Fängmark I, Strömberg B, Berge N, Rappe C. Influence of postcombustion temperature profiles on the formation of PCDDs, PCDFs, PCBzs, and PCBs in a pilot incinerator. Environ Sci Technol 1994;28:624–9.
[31] Gulyurtlu I, Crujeira AT, Cabrita I. Measurement of dioxin emissions during co-firing in a fluidised bed. Fuel 2007;86:2090–100.
[32] Thomas VM, McCreight CM. Relation of chlorine, copper and sulphur to dioxin emission factors. J Hazard Mater 2008;151:164–70.
[33] United States Environmental Protection Agency [homepage on the Internet]. Technology Transfer Network – Air Toxics Web Site – Hydrochloric Acid (Hydrogen Chloride). Available from: http://www.epa.gov/ttn/atw/hlthef/hydrochl.html.
[34] Bergman PCA. Combined torrefaction and pelletisation – the TOP process. The Netherlands: The Energy research Centre of the Netherlands (ECN); 2005. Report No.: ECN-C-05–073.
[35] Agar D, Wihersaari M. Bio-coal, torrefied lignocellulosic resources – key properties for its use in co-firing with fossil coal – their status. Biomass Bioenergy 2012;44:107–11.
[36] EN 15148 Solid biofuels – determination of the content of volatile matter. Finland: The Finnish Standards Association (SFS); 2009.
[37] McMullan J, Morgan R, Murray R. Energy resources and Supply. John Wiley & Sons; 1977.

[38] Hansen LA, Frandsen FJ, Dam-Johansen K, Sørensen HS. Quantification of fusion in ashes from solid fuel combustion. Thermochim Acta 1999;326:105–17.
[39] Raiko R, Saastamoinen J, Hupa M, Kurki-Suonio I. Poltto ja palaminen. International Flame Research Foundation. Finland: Gummerus Kirjapaino Oy; 2002 [Finnish].
[40] Alakangas E. Properties of fuels used in Finland. Finland: Technical Research Centre of Finland (VTT); 2000. Report No.: 2045. [Finnish].
[41] Clarke LB, Sloss LL. Trace elements – emissions from coal combustion and gasification. London: IEA Coal Research; 1992.

Publication V

Henrik Tolvanen, Tiina Keipi, Risto Raiko

A study on raw, torrefied, and steam-exploded wood: fine grinding, drop-tube reactor combustion tests in N_2/O_2 and CO_2/O_2 atmospheres, particle geometry analysis, and numerical kinetics modeling

Fuel, Volume -, Submitted in August 2015.

A study on raw, torrefied, and steam-exploded wood: fine grinding, drop-tube reactor combustion tests in N_2/O_2 and CO_2/O_2 atmospheres, particle geometry analysis, and numerical kinetics modeling

Henrik Tolvanen[a], Tiina Keipi[a], and Risto Raiko[a]

[a]*Department of Chemistry and Bioengineering, Tampere University of Technology, Korkeakoulunkatu 1, 33720 Tampere, Finland*

Corresponding author: Henrik Tolvanen, Tel.:+358 40 86 16 718, E-mail address: henrik.tolvanen@tut.fi

Keywords: combustion, biomass, chemical kinetics, carbon dioxide, drop-tube reactor

Abstract

The purpose of this study was to compare the fine grinding properties and combustion behavior of three wood pellet products: raw, torrefied, and steam-exploded wood. The energy required to fine grind the pellets was tested, and so was the geometry and size distribution of the resulted grinding products. Out of all the samples the steam-exploded wood pellet required the most energy for grinding. However, it also produced more sphere-like particles compared to the other two types of samples. The combustion behavior of the samples was tested in a laminar drop-tube reactor (DTR). The samples were preground and the particles were sieved with vibration sieves with an opening of 112-125 µm. The pyrolysis process was examined separately at a temperature range of 973-1173 K. The combined pyrolysis and combustion tests were carried out at a reactor temperature of 1123 K. The O_2 concentrations used in the measurements were 3–21 vol-% in either N_2 or CO_2 atmospheres. The initial size distribution

of the sample particles as well as their diameter evolution during pyrolysis and combustion was studied by using optical techniques. The surface temperature of the combusting particles was measured with a two-color pyrometer from within the DTR. The density, specific surface area, and pore diameter were measured from the ground samples with a mercury porosimeter. The chemical kinetic parameters, which describe the pyrolysis and char oxidation rates of the samples, were determined by using the data from the measurements.

1. Introduction

Biomass as a power production fuel has a great number of shortcomings compared to fossil coal. It has a lower energy density and, due to its firbour nature, more energy is required for grinding and milling it than fossil fuels. The shape of ground coal particles is usually round whereas biomass particles tend to be elongated. This characteristic can affect particle trajectories in furnaces. Due to biological degradation, the storability of biomass is also inferior to that of coal. Nevertheless, it is possible to at least partially overcome these shortcomings by thermally pretreating biomass. Torrefaction and steam explosion are pretreatment processes that can improve both the energy density of biomass and its grindability [1].

Torrefaction can be defined as a roasting process or incomplete pyrolysis. The temperature range is usually defined as 200–300 °C. A key attribute of torrefaction is that it is carried out in the absence of oxygen. [2] The acclaimed benefits of torrefaction are that it changes the properties of biomass from hydrophilic to hydrophobic, and it also reduces the energy required for fine grinding the feedstock [3] and [4]. Steam explosion, on the other hand, is a process where the water inside the pores of biomass tissue undergoes adiabatic expansion. It results in both mechanical deformation and chemical degradation of the feedstock [5].

One of the most likely applications of thermally pretreated biomass is to co-fire it with fossil coal in pulverized fuel furnaces. The combustion properties of biomasses in general are not as well defined as with coal. Furthermore, if flue gas recirculation or gasification of the feedstock are applied, information on the fuel reactivity in reducing atmosphere is required because it is not yet well known how reducing environment affects the oxidation rate. Unfortunately, especially in the case of torrefied and steam-exploded biomasses, this type of information is not yet available.

The objective of this study was to investigate the pyrolysis and combustion behavior of ground raw, torrefied, and steam-exploded wood pellets. It has been noted in literature, among others [6] and [7], that pyrolysis kinetics and the resulting char porosity change substantially when the heating rate varies. A drop-tube reactor (DTR) can be used to simulate the temperature level, oxygen concentration, and especially the heating rates of fluidized bed combustion and pulverized fuel firing. Therefore, a DTR was chosen as the main study instrument in this work. Along with the DTR, this study uses a combination of optical and physical measurement techniques in order to examine the overall combustion process of the aforementioned types. The study also shows how important it is to use kinetic modeling when comparing the reactivities of different woody biomasses. The combustion tests were conducted both in O_2/N_2 or O_2/CO_2 atmospheres.

The kinetic parameters related to the char oxidation reaction were determined based on the O_2/N_2 environment tests. The DTR setup was not suited for determining the gasification reaction between CO_2 and solid carbon. Thermogravimeter (TGA) based tests suggest that the CO_2 gasification reaction accounts for well over 20% of the solid fuel mass loss at high temperatures [8]. A comparison of the oxidation and CO_2 gasification reaction rates based on low

heating rate measurements can be found in [9]. This paper suggests that the gasification reaction is notable compared to oxidation. However, there is very little data reported on the ratio of the oxidation and gasification reactions in high heating rates. Therefore, in this work, the O_2/CO_2 model calculations were conducted with the kinetic parameters derived from the O_2/N_2 tests and without the effect of the gasification. This approach was also used to simplify the models as much as possible for later use in CFD codes. The experimental results matched rather well with the model calculations both in terms of mass loss and particle surface temperature. This would indicate that the gasification reaction would not have been as significant as the low heating rate tests would imply. However, the DTR measurement system is not precise enough to provide any conclusive evidence on this.

2. Materials and methods

2.1. Fuel composition and sample preparation

This particular study tested three types of fuel samples: raw wood, torrefied wood, and steam-exploded wood. The sample materials were commercially available pellet products and thus the wood species were different. The raw wood was Finnish spruce, the torrefied sample Swedish spruce, and the steam-exploded sample Southern Yellow Pine. The torrefied and steam-exploded wood samples were received to the laboratory tests in the form of pellets. The raw wood was originally pelletized, but for the DTR tests it was received preground. From the torrefied wood raw material 90% was softwood, and the rest hardwood. The stem wood raw material had been first chipped and then torrefied. The torrefaction had been completed at 250 °C in a continuously operated reactor. The residence time of the chips in the reactor had been approximately 0.5 h. The mass yield of the torrefaction process had been 89.6% from the original weight. The torrefied wood had then been pelletized with a ring matrix pelletizer. The

steam-exploded biomass sample in turn was biomass made from conifer chips. The reactor pressure level had been 15-25 bar and the residence time under 20 minutes. The temperature level had been approximately 210 °C. The raw biomass was pinewood. The ultimate and proximate analyses of the samples are presented in Table 1. The ash fusion temperatures and the mercury porosimeter results of the samples are also presented.

Table 1: The results of the ultimate, proximate, ash fusion, and porosimeter analyses for the samples tested in this study.

Analysis	Raw	Torrefied	Steam-exploded	Unit
Ash content (815°C)	0.3	0.2	-	dry wt%
Ash content (550°C)	0.3	0.2	0.5	dry wt%
Volatile matter	84.9	81.9	76.2	dry wt%
Sulfur	<0.02	<0.02	<0.02	dry wt%
Carbon	50.8	53.2	54	dry wt%
Hydrogen	6.1	6	5.9	dry wt%
Nitrogen	<0.2	<0.2	<0.2	dry wt%
Oxygen (calculated)	42.7	40.38	39.4	dry wt%
Chlorine	0.003	0.002	0.008	dry wt%
Fluorine	<0.001	0.001	<0.001	dry wt%
Bromine	<0.001	<0.001	<0.001	dry wt%
Gross Calorific Value	20.3	21.07	21.79	MJ/kg
Lower heating value	18.97	19.77	20.51	MJ/kg

Fusibility of ash	Raw	Torrefied	Steam-exploded	Unit
Deformation temperature	1440	1310	1250	°C
Sphere temperature	>1450	-	1260	°C
Hemisphere temperature	>1450	1330	1290	°C
Flow temperature	>1450	1360	1300	°C

Porosimeter results	Raw	Torrefied	Steam-exploded	Unit
Apparent density	1055	931.0	1166	kg m^{-3}
Intrinsic density	1500	1208	1341	kg m^{-3}
Average pore diameter	3.078	0.1845	0.07129	µm
Total pore area	0.285	5.317	5.729	m^2 g^{-1}

The density of the samples that were chosen for the experiments was measured with a Micrometrics Poresizer 9320 mercury porosimeter in the Department of Civil Engineering at Tampere University of Technology. The density

measurements were conducted with the same sample particle size that was used in the DTR tests. The intrinsic density of the samples was calculated according to the mercury intrusion volume when all the pores greater than 6 nm were filled. The apparent density was evaluated with a mercury intrusion threshold of 26 μm. The threshold value was chosen according to the evaluated resolution of the already defined particle projection surface area. In the mercury intrusion volume curve as a function of average pore diameter, the 26 μm value appeared to be the point where mercury had filled most of the gaps between the particles and started intruding inside them. Furthermore, based on image analysis, the evaluated particle apparent density and the particle volume could be used to calculate the mass of the particles. The calculated apparent density values, the mercury porosimeter-based intrinsic density along with the average pore diameter and total pore area are presented in Table 1.

From the three samples, the raw wood had the smallest pore area. It also had the highest intrinsic density. The low apparent density value could be explained with the shape of the ground particles and the imaging technique. Admittedly, the use of mercury porosimeter -based surface area and pore size most likely influence the determined kinetic parameters, since many of the pores in the particle are surely smaller than 6 nm. Furthermore, the pore size evolution should be studied further, since a rapid pyrolysis process generates larger pores. Due to lack of better techniques available, the presented pore diameters and surface areas were used as initial parameters in the model calculations of this study. The pore diameter was assumed to stay constant, and the surface area as function of conversion was calculated according to the Bhatia-Perlmutter random pore model, which is explained in a later section of this article.

Before the DTR tests, the samples were ground and sieved to a size fraction of 112-125 μm. However, it must be noted that this fraction size only represents

the ring sieve openings, not the overall size fraction of the sample particles. The spherical equivalent particle diameter distribution of each sample along with projections of the preprocessed particles is shown in Figure 1.

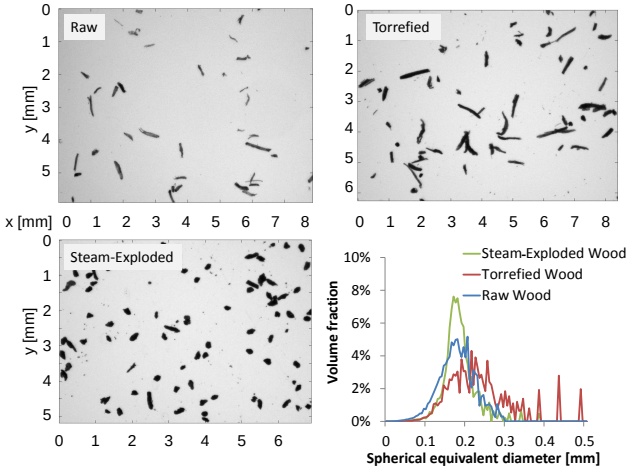

Figure 1: The preprocessed particle projections and the spherical equivalent particle diameter distribution of the samples before the DTR treatment.

The projections in Figure 1 show that the particles were elongated and thus the spherical equivalent mass mean diameter was greater than the sieve sizes. In order to avoid absorption of moisture or impurities, the samples were stored in air sealed containers.

2.2. Drop-tube reactor

The DTR system employed in this study was designed by the first author. The design was based on previous versions constructed at the Tampere University of Technology, Finland. The reactor design and the auxiliary devices are described and depicted in more detail in [10]. The ideal solution for char oxidation tests in a DTR is usually to insert prepyrolyzed particles into the reactor. With coal samples this is relatively easy since the shape and size of

the pyrolyzed particles is very much similar to the original coal particles, and they also have sufficient structural strength. However, since biomass has such a small amount of char in it, the pyrolyzed particles are small and brittle. Therefore, the char combustion process with wood could not be studied separately from pyrolysis. The pyrolysis tests were conducted in pure N_2 and for the char combustion tests O_2 was added to the atmosphere. The O_2 concentrations used in the measurements were 3–21 vol-% in either N_2 or CO_2 atmospheres. The pyrolysis process was examined separately at a temperature range of 973-1173 K. The combined pyrolysis and combustion tests were carried out at a reactor temperature of 1123 K. The same type of particles were used in both cases. Because unpyrolyzed particles were used in the combustion tests, the effect of the volatiles combustion had to be considered. A small amount of char was produced for these tests. The aim was to see how the volatiles combustion affected the particle surface temperature. The production process was very laborous and thus only three test runs could be conducted. The results of these tests are further discussed in the results chapter.

2.3. Particle velocity measurements

A high-speed camera was used for taking photographs through the measuring windows of the particle stream inside the reactor. The recorded pictures were then analyzed with a computer program in order to determine the velocity of the particles. The camera was an AVT Marlin 145-B2 with a 1380×1090 resolution and with a black and white CCD-cell. The camera was placed in front of the measurement windows, and the background led-light was placed to the opposite side of the reactor. The falling particles generated a double shadow to the image because of the pulsating LED-light located on the opposite side of the reactor. Based on the distance of the shadows and the time delay between the two pulses, the analysis program could determine the velocity of the particles. The velocity

measurement setup is discussed further in [11].

2.4. Determining particle diameter

The diameter of the particles was determined in a separate stage after the reactor treatment. First, the particles were scattered on a light diffuser that was luminated from below with an LED light. The CCD camera was used to take pictures of the particle projections. The diameter of the particles was determined from these images with a computer program. For easier comparability, the presented diameters are all those of a sphere with an equal volume. The measurement setup and the analysis program are discussed further in [11].

2.5. Two-color pyrometer

The pyrometer used in this study was mainly based on the work of [12] and it is discussed further in [10].

2.6. Fine grinding energy measurement

The instruments used in determining the fine grinding energy requirement for the sample pellets were a Retsch ZM200 ultra-centrifugal mill for grinding and a Christ Elektronik CLM1000PP energy consumption meter for monitoring the power draw of the mill. The procedure of determining the fine grinding energy requirement is the same that has already been explained in [13]. The amount of sample mass per measurement was 20 g, and the sample was fed to the mill in the form of pellets. The raw wood pellet sample was from a different batch than the ones fed into the DTR. For the torrefied and steam-exploded samples the batches were the same. In addition to the fine grinding energy, the resulted particle size distribution was also studied. These studies followed the same procedure that was used in determining the DTR sample particle diameters.

3. Modeling

3.1. Mass loss chemical kinetics

The kinetic model describing the fuel particle mass loss was selected so that the resulting parameters could be directly utilized in commercial computational fluid dynamics programs, such as Fluent. The pyrolysis chemical kinetics were modeled according to the rate expressions proposed by Kobayashi [14]. The volatile yield $m_v\,(t)$ (kg) up to time t (s) can be written as:

$$m_v\,(t) = m_{0,DAF} \int_0^t (\alpha_1 R_1 + \alpha_2 R_2) \exp\left(- \int_0^t (R_1 + R_2)\, dt \right) dt \qquad (1)$$

,where α_1 and α_2 are yield parameters (-), R_1 and R_2 are the competing reaction rates (s^{-1}), and $m_{0,DAF}$ is the dry, ash-free initial mass of the particle before entering the reactor (kg). Both reaction rates can be expressed in the form of the Arrhenius equation:

$$R_n = A_n \exp\left(-\frac{E_{a,n}}{R_u T} \right) \qquad (2)$$

,where A_n is the pre-exponential factor of the reaction rate coefficient (s^{-1}), $E_{a,n}$ is the exponential factor of the reaction rate coefficient (J mol^{-1}), R_u is the universal gas constant (J $mol^{-1}K^{-1}$), and T is the reaction temperature (K).

At the moment of entering the reactor, the dry, ash-free part of the particle was assumed to consist entirely of material available for the oxidation reaction. In some models the pyrolysis reactions form volatiles in the beginning, followed by the separate char oxidation to CO. In this work the unreacted wood in the particle was set to be available for both pyrolysis and oxidation reactions. Therefore, both reactions occurred simultaneously. This approach meant that some of the unvolatilized compounds could oxidize as well. However, it was noted that when using the Kobayashi pyrolysis model at high O_2 concentrations,

which in turn meant higher temperatures, the formation of volatiles increased and the pyrolysis reactions were faster. The simultaneous oxidation of char and unvolatilized compounds was thus very minor. Therefore, it can be stated that the oxidation kinetic parameters actually describe virtually entirely char oxidation. A commonly used approach, e.g. [15], to calculate the char oxidation rate is to use the intrinsic model. The intrinsic model takes into account the extra- and intraparticle diffusion of the oxidizing agent. The mass loss related to the char and oxygen reaction can be expressed in terms of the kinetic rate and the diffusion rate coefficient as:

$$\frac{dm_p}{dt} = -A_p p_{O_2\infty} \frac{D_0 R}{D_0 + R} \tag{3}$$

,where A_p is the spherical equivalent diameter based area of the particle (m^2), $p_{O_2\infty}$ is the partial pressure of oxygen in the surrounding gas (Pa), R is the kinetic rate of the reaction (s m^{-1}), D_0 is the diffusion rate coefficient related to oxygen diffusion through the boundary layer (s m^{-1}). The intrinsic kinetic model used in this study is based on Smith's work [16]. Thus, the reaction order is assumed to be equal to unity. The kinetic rate of the reaction can be expressed in terms of the intrinsic chemical and pore diffusion rates as:

$$R = \eta \frac{d_p}{6} \rho_p A_g k_{c,i} \tag{4}$$

,where d_p is the equispherical diameter of the particle (m), ρ_p is the apparent density of the particle (kg m^{-3}), A_g is the internal surface area of the particle (m^2 kg^{-1}), and $k_{c,i}$ is the intrinsic reactivity (s m^{-1}). The reactivity is again of the Arrhenius form:

$$k_{c,i} = A_c e^{\left(-\frac{E_{a,c}}{R_u T}\right)} \tag{5}$$

,where A_c is the pre-exponential factor of the reaction rate coefficient (s m^{-1}),

E_a is the exponential factor of the reaction rate coefficient (J mol^{-1}), R_u is the universal gas constant (J mol^{-1}K^{-1}), and T is the reaction temperature (K). The term η in the kinetic rate equation is the effectiveness factor (-). This term is described in Section 3.3, Equation 14.

3.2. Particle energy balance

In the pyrolysis and combustion modeling, the particles were divided into 20 concentric cores, each of which had the same initial volume. The energy balance equation was solved numerically, and each core had its own devolatilization and carbon consumption reaction rate and properties based on its temperature. The core thickness was calculated again at each time step based on the mass loss and the volume change equation. The general energy balance equation for a combusting char particle can be written in a differential form as:

$$\frac{\partial \left(\rho_p T_p\right)}{\partial t} = \frac{1}{c_p}\frac{1}{r^2}\left(\frac{\partial}{\partial r} r^2 k_p \frac{\partial T_p}{\partial r}\right) + \frac{1}{c_p}\dot{r}\left(-\Delta h\right) \tag{6}$$

,where ρ_p is the density of the particle (kg m^{-3}), c_p is the heat capacity of the particle (J kg^{-1} K^{-1}), t is the time (s), r is the radius of the particle (m), k_p is the heat conductivity (W m^{-1} K^{-1}), T_p is the temperature of the particle (K), $\dot{r}$ is depending on the case either the pyrolysis reaction rate or the reaction rate at which carbon is consumed (kg s^{-1}) during char char oxidation, and Δh is the reaction enthalpy (J kg^{-1}) related to the considered reaction. The reaction enthalpies of the oxidation reaction were found from literature, e.g [17]. The pyrolysis reaction enthalpy was set to 120 kJ kg^{-1}; endothermic for all the samples. The term on the left hand side describes the energy stored in the particle. The first term on the right hand side describes the heat conduction and the second term the internal heat generation or consumption resulting from the chemical reactions taking place during the process. Because of symmetry, the heat flux is zero at the particle center point.

The boundary condition for the particle surface can be written as:

$$-k_p \frac{\partial T_p}{\partial r} = \theta h_c \left(T_{gas} - T_p\right) + \varepsilon\sigma \left(T_{wall}^4 - T_p^4\right) \tag{7}$$

,where θ is a coefficient related to the Stefan flow (-), h_c is the convective heat transfer coefficient (W m^{-2} K^{-1}), T_{gas} is the gas temperature (K), T_{wall} is the reactor wall temperature (K), ε is the emissivity of the particle (-), and σ is the Stefan–Boltzmann constant (W m^{-2} K^{-4}). The term on the left hand side describes heat conduction. The first term on the right hand side describes heat convection to the particle from the surrounding gas, the second term describes radiative heat transfer between the wall and the particle. As a result of the measurements, both the gas and wall temperature profiles were known. The heat conductivity inside the particle was assumed to be a constant value of 0.1 W m^{-1} K^{-1}. This term took into account both the conduction of the char itself as well as the effect of the gas conductivity in the particle pores. The heat transfer coefficient was calculated with the Ranz Marshall [18] correlations widely used in combustion literature. The emissivity of the particle in the radiation part was set to be 0.9 as proposed by [19]. There are various correlations presented in literature for biomass and wood specific heat capacity. However, due to the uncertainties related to measuring the specific heat capacity at the temperature levels examined in this work, a constant value was used. Based on the heat capacity correlations presented in [20], a value of 1500 J kg^{-1} K^{-1} was chosen. This value was used both in the pyrolysis and combustion models. The value was chosen to represent the combined heat capacity of the unreacted part of the particle, the formed char, and the voids filled by gases.

The Stefan flow term θ in the convection part of the energy balance equation was used as presented in [21]. The equations related to that are also shown in [11].

3.3. Gas diffusion

The mass transfer processes inside a combusting spherical particle can be described with the following differential equation:

$$\frac{\partial C}{\partial t} = \frac{1}{r^2}\left(\frac{\partial}{\partial r} r^2 D \frac{\partial C}{\partial r}\right) + \dot{C} \tag{8}$$

,where C is the gas concentration (mol m^{-3}), r is the radius (m), and the last term $\dot{C}$ describes the consumption of the diffusing gas species due to chemical reactions (mol $m^{-3}s^{-1}$). The boundary condition on the particle surface can be calculated with the help of gas film diffusion theory. The common approach to model gas film diffusion is to use a simple integrated form of Fick's Law [22], presented as:

$$\dot{N}^{"}_{gas} = k_d \left(C_{gas,\infty} - C_{gas,s}\right) \tag{9}$$

,where $\dot{N}^{"}_{gas}$ is the molar flow of gas through a surface (mol s^{-1} m^{-2}), $C_{gas,\infty}$ is the concentration of the gas outside the boundary layer, and $C_{gas,s}$ is the gas concentration on the particle surface. In this study the concentration of the boundary layer was calculated at the average temperature of the bulk gas and the particle surface. The mass transfer coefficient k_d (m s^{-1}) was calculated from the Ranz Marshall correlation while expressing the Sherwood number as a function of the Reynolds and Schmidt numbers:

$$k_d = \frac{ShD_{AB}}{d_p} \tag{10}$$

,where Sh is the Sherwood number (-). The binary diffusion coefficient was calculated as presented in [23]:

$$D_{AB} = \frac{266T^{\frac{3}{2}}}{p(M_{AB})^{\frac{1}{2}}\sigma_{AB}^2\Omega_D} \tag{11}$$

,where D_{AB} is the diffusion coefficient (cm^2 s^{-1}), σ_{AB} is the characteristic length (Å), p is the pressure (Pa), T is the temperature (K), and Ω_D is a diffusion

collision integral (-). The term M_{AB} can be calculated as:

$$M_{AB} = 2\left[\frac{1}{M_A} + \frac{1}{M_B}\right]^{-1} \tag{12}$$

,where M_A and M_B are the molecular weights (g mol^{-1}) of gases A and B. The diffusion rate coefficient D_0 can be calculated from Equations 3 and 9:

$$D_0 = \frac{k_d M_c}{\nu R_u T} \tag{13}$$

,where M_C is the molar mass of carbon (kg mol^{-1}) an ν is the stoichiometric coefficient of the oxidation reaction (-), in this case, 0.5.

The internal concentration gradient could also be solved numerically, similarly as with the heat transfer. However, to make the calculation procedure faster, the Thiele modulus approach was used. Thiele modulus is used in determining the effectiveness factor η (-) in the kinetic rate equation. The effectiveness factor stands for the ratio of the actual reaction rate to the rate where pore diffusion was infinitely fast. It can be written as:

$$\eta = \frac{3}{\phi^2}\left(\phi \coth\left(\phi\right) - 1\right) \tag{14}$$

,where ϕ is the Thiele modulus

$$\phi = \frac{d_p}{2}\left[\frac{S_b \rho_p A_g k_{c,i} p_{O_2\infty}}{D_e \rho_{O_2}}\right]^{\frac{1}{2}} \tag{15}$$

,where S_b is the mass stoichiometric coefficient related to the char oxidation reaction to carbon monoxide (-), ρ_{O_2} is the density of the oxidant in the bulk gas (kg m^{-3}), and D_e is the effective diffusion coefficient inside the particle. Molecular and Knudsen diffusion are included in the effective diffusion coefficient as follows:

$$D_e = \frac{\theta}{\tau^2}\left[\frac{1}{D_{kn}} + \frac{1}{D_{AB}}\right]^{-1} \tag{16}$$

,where θ is the porosity calculated with the true and apparent density of the

particle (-), τ is the turtuosity of the pores (-), and D_{kn} is the Knudsen diffusion coefficient (m^2 s^{-1}):

$$D_{kn} = 97\bar{r_p}\sqrt{\frac{T_p}{M_{O_2}}} \tag{17}$$

,where $\bar{r_p}$ is the mean pore radius of the particle (m), M_{O_2} is the molecular weight of the oxidizing species (kg mol^{-1}), in this case, oxygen. The molecular binary diffusion coefficient D_{AB} (m^2 s^{-1}) is discussed in the following section. As alredy mentioned in Section 2.1, the specific surface area evolution during conversion was calculated according to the Bhatia-Perlmutter random pore model:

$$A_b = A_{b,0}\sqrt{1 - \Psi \ln\left(1 - X_{dry}\right)} \tag{18}$$

,where $A_{b,0}$ is the initial specific surface area (m^2 kg^{-1}), X_{dry} is the dry form of conversion, and Ψ is the structural parameter (-). There are correlations to calculate the structural parameter, or it can be a fitted coefficient. However, in this work the parameter was set to be 10 for all the fuels. Using the Bhatia-Perlmutter approach in this case is somewhat questionable because the model was originally developed for coal char oxidation. Since in this work the focus was on combined pyrolysis and char oxidation of biomass, the pore structure evolution might actually differ from what the equation predicts.

When calculating the overall reaction rate, the particle was first divided into co-centric cores with equal initial volumes. During each time step the particle temperature profile was first solved numerically. For the Thiele modulus the intrinsic reactivity $k_{c,i}$ was calculated with the particle average temperature. The effectiveness factor η could be then calculated. The reaction rate of each core was then calculated with their own temperature, and the average effectiveness factor was solved according to Equation 3. This procedure enabled taking into account the temperature gradient, especially in the larger particles. Moreover, using the Thiele modulus eliminated the need to solve the internal concentration

gradient numerically, thus simplifying the calculations.

3.4. Particle diameter evolution

The shape of the particles posed a problem in terms of modeling the diameter evolution of the particles as a function of the conversion. The initial shape of the particles was in some cases very elongated. However, the previous tests by Tolvanen et al. [11], indicated that during pyrolysis the shape of the biomass particles deformed and became almost spherical. At the end of the pyrolysis process no elongated particles could be detected in the images. An equispherical particle approach was therefore used. This approach also made the results easier to use in CFD calculations as all the standard models apply only to spherical particles.

The volume change equation could be written based on the diameter evolution as[16]:

$$V_e = V_{e,0}\,(1 - X)^{3\beta} \tag{19}$$

,where V_e is the volume of the element, $V_{e,0}$ is the initial volume of the element, and X is the element mass loss in dry form. If the term β is 0, the particle diameter remains constant and its density decreases during pyrolysis, i.e. the shrinking core model. The maximum value of 1/3 for β describes a situation where the density remains constant and the diameter decreases, i.e. the shrinking particle model. Calculating the kinetic parameters and the other modeling cases were all performed with particles consisting of 20 cores, all of which had the same volume in the beginning. All the cores had different temperature histories and thus also different reaction rates. Each core shrunk separately according to Equation 19. The overall particle diameter could be calculated based on sum volume of each core.

3.5. Discretizing the particle size distribution

The particle size distribution was calculated for the initial samples according to the analyzed diameter data. The distribution was discretized into ten equal-sized volume fractions. After this, the volume mean diameter of each fraction was calculated. The volume mean diameters obtained were then used as initial diameters in the model calculations. Thus, the model results, excluding the particle surface temperature, were volume-averaged.

The modeled temperature profile of the combusting particles was significantly influenced when the discretized size distribution was applied. This can be seen from Figure 2, where the torrefied wood sample combustion temperature profile is shown as an example.

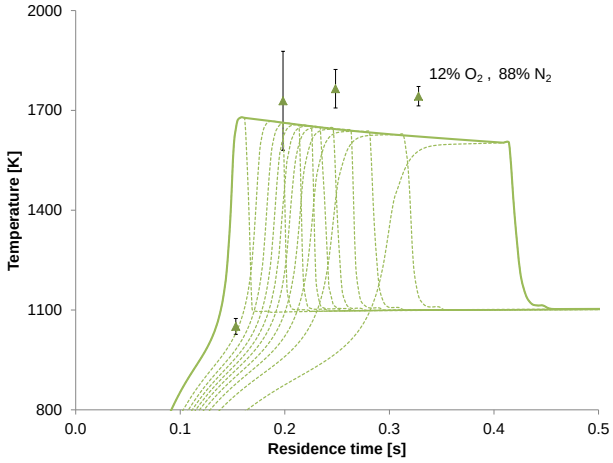

Figure 2: The use of discretized particle size distribution resulted in an overall apparent temperature profile, where the modeled temperature remained high for longer than with a mono-sized single particle model.

The importance of using discrete distribution instead of a mono-size particle model was emphasized e.g. by [24] and [25]. In the early stages of combustion the smallest particles would show in the pyrometers field of view rather

frequently because there were a lot of them. As the combustion process advanced, only the largest particles remained. The number of the larger particles was much smaller and the frequency of detecting particles decreased. This can be seen as a decreasing standard deviation in Figure 2. The temperature profile that was used in the kinetic parameter search was generated based on the ten different particle profiles. The thick line in Figure 2 represents the highest temperature attainable at a given time according to the model. Therefore, in the optimization routine, this temperature profile was allowed to overshoot the measured average values.

Regardless of the size distribution, small particle sizes meant that their terminal velocity was small compared to the gas velocity. Thus, the velocity of the particles in the reactor was assumed to be the same regardless of the particle size. Therefore, there was no difference in the residence times between different volume fractions.

3.6. Objective function and the optimization routine

A MATLAB-based objective function was written in order to determine the kinetic parameters of the selected reactions. The objective function minimized the square error between the measured values and the mass loss, particle surface temperature and diameter model predictions. The optimization routine used MATLAB's fminsearch function. The errors from the mass loss, particle surface temperature, and diameter comparisons were summed in such a manner that the mass loss and temperature error were emphasized more than the diameter error. This was done because of the greater variance in the diameter measurements and because the mass loss and temperature were of greater importance when determining the chemical kinetic parameters. The kinetic parameters were optimized for all the four N_2/O_2 concentration cases for both fuels.

4. Results and discussion

4.1. Fine grinding energy and resulting particle size distribution

The sample pellet fine grinding tests indicated that fine grinding the steam-exploded wood pellet consumed the most energy, and it also had the greatest variance in the grinding results. The torrefied wood sample, in turn, had the smallest grinding energy requirement. The pellet structure was also the most brittle of the three samples. Results presented in literature suggest that torrefaction decreases the fine grinding energy requirement [3] and [13]. However, because the pelletizing process and the possible additives can distort the results, the grinding energy tests presented in this article might be a poor indicator of how the thermal treatment technology affects the structural strength of the biomass itself. More interesting factors are the particle size and geometry resulting from the grinding process. The spherical equivalent diameter comparison of the ground samples showed that the heat or physical treatment resulted in smaller particles. This can be seen from Figure 3.

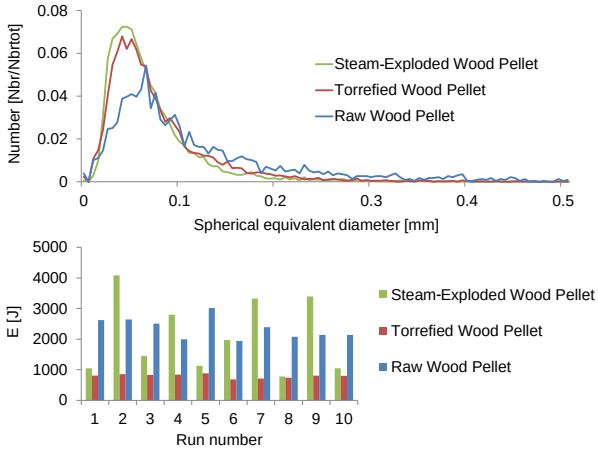

Figure 3: The spherical equivalent diameter number fractions of the particles resulting from the grinding process, and the required pellet fine grinding energies for each sample.

As already mentioned in previous sections of this article, grinding the raw wood sample resulted in significantly more elongated particles compared to the two heat treated samples. From the two types of heat treated samples the steam-exploded sample particles were by far the most spherical. This can be an important factor when determining the trajectories of the particles in industrial furnaces.

4.2. Pyrolysis

The pyrolysis process of the three samples was studied at three different temperatures in pure N_2 atmosphere. The measured values and the model fits are presented in Figure 4.

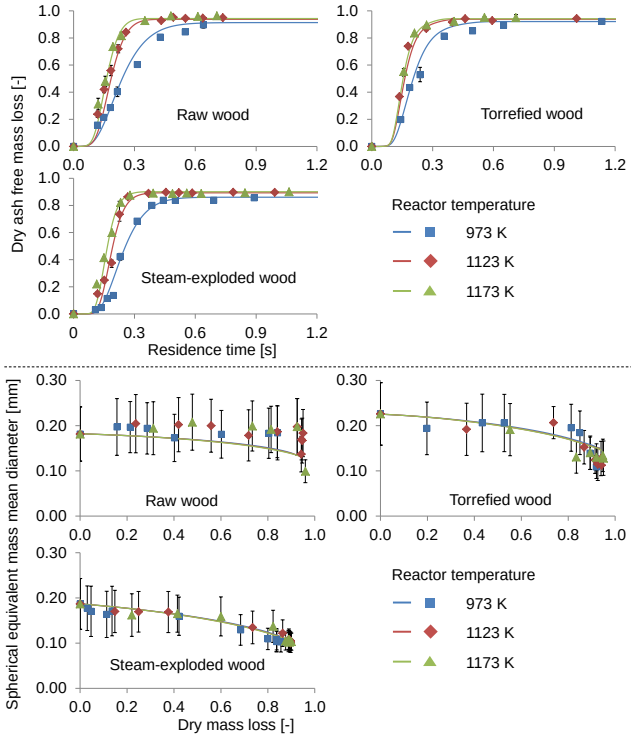

Figure 4: The dry ash-free mass loss of the samples as a function of residence time and the spherical equivalent diameter evolution of the samples as a function of dry mass loss during pyrolysis. The dots represent the measured values and the lines indicate the model fits.

The Kobayashi model fit matched the results fairly accurately. A direct comparison of the samples in terms of mass loss versus time is not entirely straightforward nor sensible. The samples have different apparent densities and therefore different falling velocities inside the reactor. Since the reactor temperature was dependent on the place in the reactor, mostly in the beginning of the heating zone, and different samples had different velocities, it is clear that they also developed different external temperature histories. Therefore, in

order to compare the reactivities of the sample fuels, kinetic modeling has to be applied.

Studying the spherical equivalent diameter evolution of the pyrolyzing particles revealed that with all samples the particle size shrunk. Diameter comparison was given the least emphasis during the multiobjective optimization routine to fit the selected parameters. However, regardless of this, in the case of torrefied and steam-exploded samples the model prediction seemed to be fairly good. With raw wood the measured values were greater than those of the model prediction. The major shortcoming of the diameter measurement setup is that all particles injected into the reactor might not have been visible or present during the diameter measurement. The smallest particles may have been pyrolyzed and gasified by the volatile gases almost entirely. As a result, a group of the smallest particles might not be present in the measurement results. This seems to be the case especially with the raw wood sample.

4.3. The effect of volatiles combustion on char oxidation

The effect of volatiles combustion on the particle surface temperatures was studied by inserting prepyrolyzed steam-exploded wood char particles into the DTR. The results were then compared to the raw sample tests. It was observed that the pyrolysis delayed the combustion process, but the volatiles combustion did not drastically change the measured particle maximum temperature during char combustion. The highest measured temperature with the unpyrolyzed sample was 1765 K, whereas the corresponding temperature measured with the steam-exploded wood char was 1692 K. In other words, the radiative heat transfer from the combusting gas film around the particle towards the particle was minor.

4.4. Combined pyrolysis and char oxidation

The char oxidation of the samples was tested with four O_2 concentrations: 3, 6, 12, and 21 vol-% combined with either N_2 or CO_2. The kinetic parameters were fitted to the N_2 measurements. The CO_2 model results were calculated with the same kinetic parameters as the N_2 ones. The changes in gas properties were taken into account. This was done in order to find out whether the gas property differences between N_2 and CO_2 were the only reason for the differences in the measured results. A small indication was found in [10] that high levels of CO_2 would interfere with the solid char and O_2 reaction by occupying some of the active sites on the surface of a combusting char particle. Another, more likely possibility for the difference could be the CO_2 gasification. The mass loss, particle surface temperature, and diameter evolution results in O_2 and N_2 atmospheres are presented in Figures 5, 6, and 7.

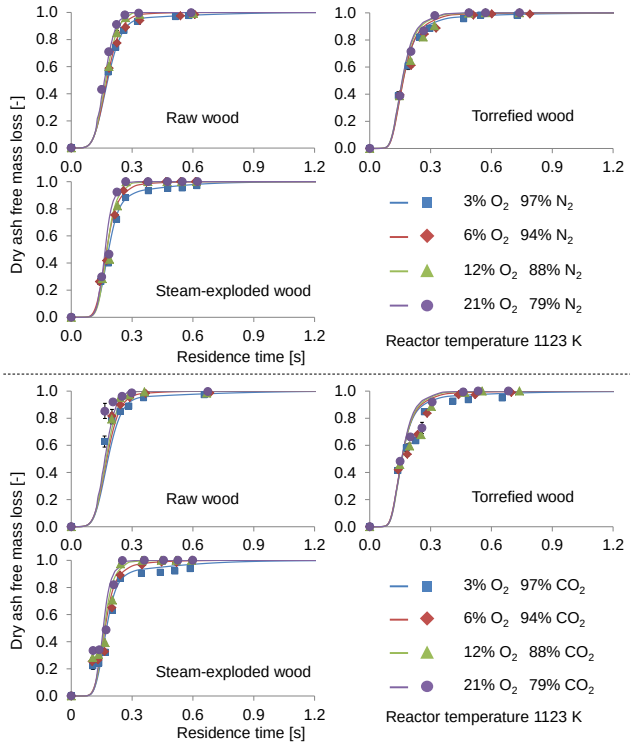

Figure 5: The dry ash-free mass loss of the samples during combined pyrolysis and char oxidation in both N_2/O_2 and CO_2/O_2 atmospheres. The dots represent the measured values and the lines indicate the model fits.

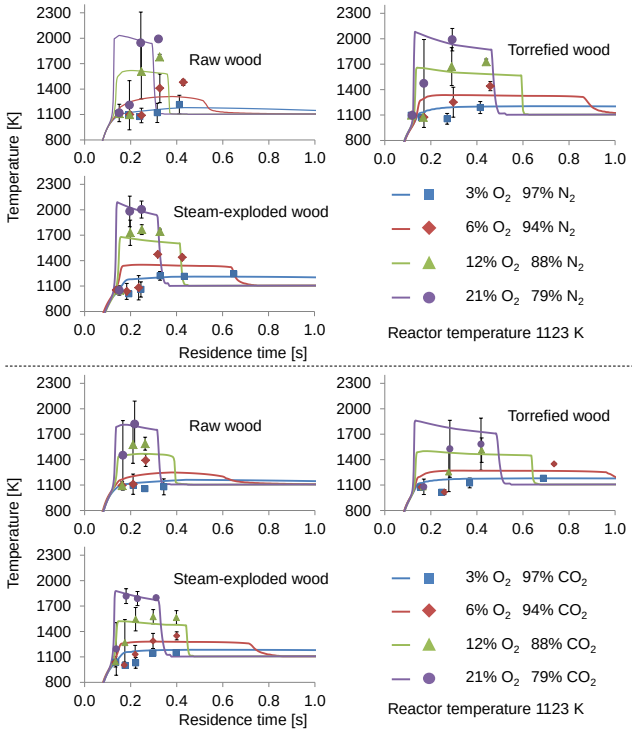

Figure 6: The particle surface temperature of the samples during combined pyrolysis and char oxidation in both N_2/O_2 and CO_2/O_2 atmospheres. The dots represent the measured values and the lines indicate the maximum values of the distributed diameter model fits.

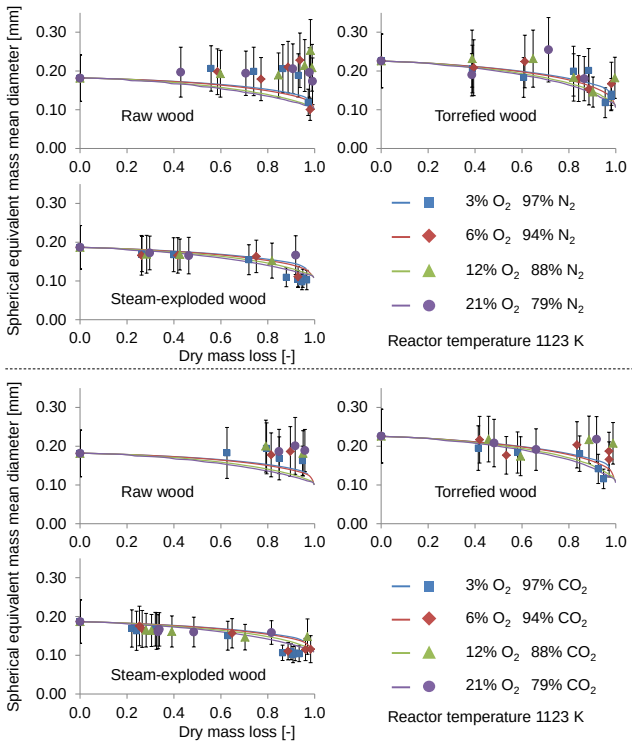

Figure 7: The spherical equivalent diameter evolution of the samples as a function of dry mass loss during combined pyrolysis and char oxidation in both N_2/O_2 and CO_2/O_2 atmospheres. The dots represent the measured values and the lines indicate the model fits.

As can be seen from the figures presented above, replacing N_2 with CO_2 reduced the measured particle surface temperatures and slightly changed the conversion rate. The decrease in the char oxidation reaction rate, particularly with the torrefied sample, can be explained similarly as in [24]. Only the largest particles remained at the end of the overall combustion process and they had slower reaction and heating rates than the smaller particles. The diameter fit of the raw wood sample was not accurate. The reason for this was that multiob-

jective optimization routine emphasized the diameter results less than the mass loss and the temperature. Moreover, the diameter measurement results of the raw wood sample seem to behave differently than the other two. This implies that there might be a systematic measurement error. The same difference could be seen in the pyrolysis and CO_2/O_2 cases. The mass loss, particle surface temperature, and diameter evolution results in O_2 and CO_2 atmospheres indicate that there is a minor difference in the results which cannot be explained entirely with the gas property differences between N_2 and CO_2. However, the difference is so minor that it can hardly be considered as conclusive evidence of CO_2 gasification competiting with the oxidation reaction. On the other hand, if the CO_2 gasification reaction would be significant the measured particle surface temperature would have been lower and the measured values and the model prediction would not have matched so well. This can be seen from Figures 5 and 6.

4.5. Fitted parameters

The kinetic parameters related to the pyrolysis and oxidation models determined in this work are presented in Table 2.

Table 2: The fitted Kobayashi pyrolysis model and the char oxidation model kinetic parameters.

Pyrolysis				
Parameter	Raw	Torrefied	Steam-exploded	Unit
A_1	64.60	92.96	72.65	s^{-1}
$E_{a,1}$	20,440	23,600	27,320	J mol^{-1}
A_2	666,710	615,700	651,700	s^{-1}
$E_{a,2}$	89410	74,190	83,300	J mol^{-1}
α_1	0.8407	0.6804	0.4279	-
α_2	0.9997	0.9997	0.9787	-
β	0.1173	0.1580	0.2561	-

Char oxidation				
Parameter	Raw	Torrefied	Steam-exploded	Unit
A	19.10	4.284	12.28	s m^{-1}
E_a	160,900	166,500	169,400	J mol^{-1}
β	0.1002	0.1202	0.1019	-

In this work, models that are commonly admitted by CFD codes were selected. The kinetic parameters can only be used in conjunction with both the combustion and pyrolysis models and employed to derive them and the reaction scheme to link the reactions. Moreover, while the reaction scheme enabled overlapping pyrolysis and char oxidation, the oxidation parameters may not be accurate if used separately from the pyrolysis model.

4.6. Sample comparison

As mentioned before, a direct comparison of the DTR results is not sensible, since the samples had different external temperature histories due to different falling velocities. Furthermore, the samples were not of the same origin. When it comes to wood species, the raw and torrefied wood samples were the closest match. Because the samples had different temperature histories in the DTR, the determined kinetic parameters were used to model the pyrolysis and char oxidation processes of the samples in the same environment. The results in

Figure 8 were calculated with 200 µm -sized particles at 1123 K reactor wall and gas temperature.

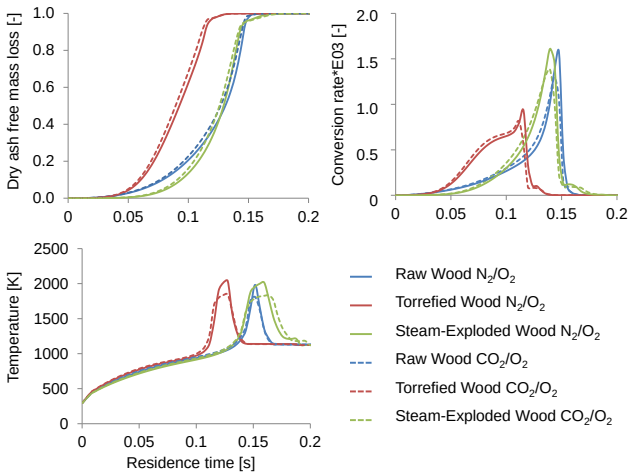

Figure 8: The mass loss, mass loss rate, and the particle surface temperature of 200 µm -sized raw, torrefied, and steam-exploded wood samples. The results were calculated with identical external temperature histories. Both the gas and the radiating surface temperatures were set to 1123 K. The O_2 concentration was set to 21% in both N_2 and CO_2.

Based on Figure 5, it would appear that the torrefied wood had the slowest overall reaction rate. However, the results shown in Figure 8 indicate that the torrefied sample actually was the fastest to reach total conversion. The steam exploded sample in turn seemed to have the highest overall reaction rate. The N_2 and CO_2 atmosphere results were calculated with the same kinetic parameters. Therefore, their difference during pyrolysis represents the higher specific heat capacity of CO_2 compared to N_2, and during char oxidation also the lower diffusivity of O_2 in CO_2 than in N_2.

There have been studies reporting improved reactivity of biomass char combustion following torrefaction [26]. On the other hand, some studies have also

stated the opposite [27]. However, it is noteworthy that these studies were conducted with thermal a gravimetric analyzer and thus had heating rates of different magnitude compared to the one used in this work. The seemingly faster overall reaction rate of the torrefied sample in the beginning derives not only from the kinetic parameters but from the density and pore structure as well. The density of the torrefied sample was the lowest of the three, resulting in faster internal heating rate. In addition, the mercury porosimeter-based mean pore diameter was significantly greater for torrefied wood than with the two other types of samples. Based on this examination no unambiguous conclusions can be drawn on how torrefaction or steam explosion affects to the pyrolysis and char oxidation rates, since the samples were not of the same origin or wood species. Instead, the value of this type of study lies in its ability to describe a methodology of how it is possible to conduct high heating rate pyrolysis and char oxidation reaction rate comparisons.

5. Conclusios

This study focused on fine grinding energy requirement, ground particle geometry, and size distribution of three different types of wood pellet products: raw, torrefied, and steam-exploded wood. The results show that grinding the steam-exploded wood pellet samples required the most energy, but it also produced more sphere-like particles compared to the other two sample types. The combustion behavior of the three samples was tested in a laminar DTR. The tests were conducted with particles that had been sieved with vibration sieves the opening of which was 112-125 μm. The pyrolysis process was examined separately at a temperature range of 973-1173 K. The combined pyrolysis and combustion tests were carried out at 1123 K reactor temperature. The oxygen concentrations chosen for the measurements were 3-21 vol-% in either N_2 or CO_2.

The kinetic parameters that described the pyrolysis and char oxidation rates were determined for each sample based on the measured mass loss, particle surface temperature, and diameter measurement results in the N_2/O_2 atmospheres. The same kinetic parameters were used in order to calculate the reaction rates of the samples in CO_2/O_2 atmospheres. The property differences between CO_2 and N_2 explained the differences in the measured results rather well. Therefore, the kinetic parameters determined in N_2/O_2 atmospheres and high heating rates could be used with a reasonable accuracy in model calculations when CO_2 is present. The gasification reaction between CO_2 and solid char may reduce this accuracy. However, based on the measured and modeled particle surface temperature results it appeared that the overall effect of the gasification reaction was not very significant in the experiments of this work.

For the sample reaction rate comparison, the determined kinetic parameters were used to calculate the reaction rates of 200 µm -sized sample particles in identical external conditions. This examination revealed that the torrefied wood sample had the fastest pyrolysis rate, whereas the fastest oxidation rate was noted with the steam-exploded sample. From the three types of tested samples, the raw wood sample had the slowest overall reaction rate. Overall, this study shows how important it is to combine optical and physical measurement techniques when conducting high heating rate reactivity tests. It is also vital to use kinetic modeling for sample reactivity comparisons and not only compare the measurement data itself due to the different temperature histories particles experience in measurement devices such as the DTR. In the future, more emphasis should be put on studying the overlapping pyrolysis and oxidation reactions with larger biomass particles, since they are also present in pulverized fuel furnaces and are the cause of much of the unburnt material.

6. Acknowledgments

The authors gratefully acknowledge the financial support of Valmet Co., Fortum Co., UPM-Kymmene Co., Pohjolan Voima Co., and Helen Co. for this study. The authors also acknowledge the help of M.Sc. Matti Paananen and Ph.D. Markus Honkanen for arranging the pyrometer and particle imaging setups for the measurements.

7. References

[1] A. K. Biswas, W. Yang, W. Blasiak, Steam pretreatment of Salix to upgrade biomass fuel for wood pellet production, Fuel Processing Technology 92 (9) (2011) 1711 – 1717, ISSN 0378-3820, doi:http://dx.doi.org/10.1016/j.fuproc.2011.04.017, URL http://www.sciencedirect.com/science/article/pii/S037838201100138X.

[2] J. Bourgois, R. Guyonnet, Characterization and analysis of torrefied wood, Wood Science and Technology 22 (1988) 143–155.

[3] V. Repellin, A. Govin, M. Rolland, R. Guyonnet, Energy requirement for fine grinding of torrefied wood, Biomass and Bioenergy 34 (7) (2010) 923 – 930, ISSN 0961-9534, doi:http://dx.doi.org/10.1016/j.biombioe.2010.01.039, URL http://www.sciencedirect.com/science/article/pii/S096195341000053X.

[4] J. H. Peng, H. T. Bi, S. Sokhansanj, J. C. Lim, A Study of Particle Size Effect on Biomass Torrefaction and Densification, Energy & Fuels 26 (6) (2012) 3826–3839, doi:10.1021/ef3004027, URL http://dx.doi.org/10.1021/ef3004027.

[5] R. L. Pereira, The chemistry involved in the steam treatment of lignocellulosic materials, Quím. Nova 26 (2003) 863 – 871, ISSN 0100-4042.

[6] L.-P. Wiktorsson, W. Wanzl, Kinetic parameters for coal pyrolysis at low and high heating rates: a comparison of data from different laboratory equipment, Fuel 79 (6) (2000) 701 – 716, ISSN 0016-2361.

[7] E. Biagini, M. Simone, L. Tognotti, Characterization of high heating rate chars of biomass fuels, Proceedings of the Combustion Institute 32 (2) (2009) 2043 – 2050, ISSN 1540-7489, doi:http://dx.doi.org/10.1016/j.proci.2008.06.076, URL http://www.sciencedirect.com/science/article/pii/S1540748908001508.

[8] E. S. Hecht, C. R. Shaddix, M. Geier, A. Molina, B. S. Haynes, Effect of CO2 and steam gasification reactions on the oxy-combustion of pulverized coal char, Combustion and Flame 159 (11) (2012) 3437 – 3447, ISSN 0010-2180, doi:http://dx.doi.org/10.1016/j.combustflame.2012.06.009, URL http://www.sciencedirect.com/science/article/pii/S0010218012001897.

[9] O. Karlström, A. Brink, M. Hupa, Desorption kinetics of CO in char oxidation and gasification in O2, CO2 and H2O, Combustion and Flame 162 (3) (2015) 788 – 796, ISSN 0010-2180, doi:http://dx.doi.org/10.1016/j.combustflame.2014.08.010, URL http://www.sciencedirect.com/science/article/pii/S0010218014002466.

[10] H. Tolvanen, R. Raiko, An experimental study and numerical modeling of combusting two coal chars in a drop-tube reactor: A comparison between N2/O2, CO2/O2, and N2/CO2/O2 atmospheres, Fuel 124 (0) (2014) 190 – 201, ISSN 0016-2361, doi:http://dx.doi.org/10.1016/j.fuel.2014.01.103, URL http://www.sciencedirect.com/science/article/pii/S0016236114001227.

[11] H. Tolvanen, L. Kokko, R. Raiko, Fast pyrolysis of coal, peat, and torrefied wood: Mass loss study with a drop-tube reactor, particle geometry analysis, and kinetics modeling, Fuel 111 (0) (2013) 148 – 156, ISSN 0016-2361, doi:http://dx.doi.org/10.1016/j.fuel.2013.04.030, URL http://www.sciencedirect.com/science/article/pii/S0016236113003165.

[12] T. Joutsenoja, Pyrometric Thermometry and Sizing of Fuel Particles in Combustion, Ph.D. thesis, TTKK, 1998.

[13] L. Kokko, H. Tolvanen, K. Hämäläinen, R. Raiko, Comparing the energy required for fine grinding torrefied and fast heat treated pine, Biomass and Bioenergy 42 (0) (2012) 219 – 223, ISSN 0961-9534, doi:http://dx.doi.org/10.1016/j.biombioe.2012.03.008, URL http://www.sciencedirect.com/science/article/pii/S0961953412001262.

[14] H. Kobayashi, J. Howard, , A. Sarofim, 16th Symposium (International) on Combustion, in: Coal Devolatilizationat High Temperatures, The Combustion Institute, 411–425, 1976.

[15] O. Karlström, A. Brink, J. Hercog, M. Hupa, L. Tognotti, 16th IFRF Members' Conference: Combustion and sustainability: new technologies, new fuels, new challenges, Boston, in: Kinetic combustion parameters for chars using the IFRF solid fuel data base, 2009.

[16] I. W. Smith, The Combustion Rates of Coal Chars: A Review, The Combustion Institute In 19th Symposium on Combustion (1982) 1045–1065.

[17] P. W. Atkins, Physical Chemistry, Oxford University Press, 6th edn., iSBN: 019850102, 1998.

[18] W. E. Ranz, J. W. R. Marshall, Evaporation from Drops, Part II, Chem. Eng. Prog. 48 (1952) 173–180.

[19] P. R. Solomon, D. G. Hamblen, M. A. Serio, Z.-Z. Yu, S. Charpenay, A characterization method and model for predicting coal conversion behaviour, Fuel 72 (4) (1993) 469 – 488, ISSN 0016-2361.

[20] M. Grønli, A Theoretical and Experimental Study of the Thermal Degradation of Biomass, Ph.D. thesis, The Norwegian University of Science and Technology, 1996.

[21] P. R. Solomon, M. A. Serio, E. M. Suuberg, Coal pyrolysis: experiments, kinetic rates, and mechanisms, Progress in energy and combustion science 18 (1992) 133–220.

[22] N. M. Laurendeau, Heterogeneous kinetics of coal char gasification and combustion, Progress in energy and combustion science 4 (1978) 221–270.

[23] R. C. Reid, J. M. Prausnitz, B. E. Poling, The Properties of Gases & Liquids, McGraw-Hill, Inc. New York., 4th edn., 1987.

[24] J. Ballester, S. Jiménez, Kinetic parameters for the oxidation of pulverised coal as measured from drop tube tests, Combustion and Flame 142 (3) (2005) 210 – 222, ISSN 0010-2180, doi:http://dx.doi.org/10.1016/j.combustflame.2005.03.007, URL http://www.sciencedirect.com/science/article/pii/S0010218005000817.

[25] M. Simone, E. Biagini, C. Galletti, L. Tognotti, Evaluation of global biomass devolatilization kinetics in a drop tube reactor with {CFD} aided experiments, Fuel 88 (10) (2009) 1818 – 1827, ISSN 0016-2361, doi:http://dx.doi.org/10.1016/j.fuel.2009.04.032, URL http://www.sciencedirect.com/science/article/pii/S0016236109002087.

[26] A. Toptas, Y. Yildirim, G. Duman, J. Yanik, Combustion behavior of different kinds of torrefied biomass and their blends with

lignite, Bioresource Technology 177 (0) (2015) 328 – 336, ISSN 0960-8524, doi:http://dx.doi.org/10.1016/j.biortech.2014.11.072, URL http://www.sciencedirect.com/science/article/pii/S0960852414016745.

[27] J. Jones, T. Bridgeman, L. Darvell, B. Gudka, A. Saddawi, A. Williams, Combustion properties of torrefied willow compared with bituminous coals, Fuel Processing Technology 101 (0) (2012) 1 – 9, ISSN 0378-3820, doi:http://dx.doi.org/10.1016/j.fuproc.2012.03.010, URL http://www.sciencedirect.com/science/article/pii/S0378382012001038.

Tampereen teknillinen yliopisto
PL 527
33101 Tampere

Tampere University of Technology
P.O.B. 527
FI-33101 Tampere, Finland

ISBN 978-952-15-3666-3
ISSN 1459-2045